Investigation of Determining Velocity Profiles in Microfluidic Channel Using Micro PIV

by

Fahimeh Behboodi

A thesis submitted in partial fulfillment of the requirements for the degree of

Master of Science

Department of Mechanical Engineering
University of Alberta

ABSTRACT

An investigation of the velocity profile in a microscale (<5mm) channel using micro PIV technique is presented. Measuring the velocity profile in the microchannel becomes increasingly important with the improved attention to microscale devices. Theory dictates that flow in the channel has a parabolic velocity profile according to Navier Stokes assumptions and formulas. The channel which was used in this study had a scale of 0.8 mm width and 2 mm length. Flow, seeded with hollow sphere particles, is pumped through the channel. Micro particle image velocimetry measured the velocity profile by measuring movement of particles in one interrogation window over time and calculate velocity related to each window. Different algorithms for processing data including various interrogation window sizes and shapes were determined using commercial software (DaVis 8.0.7, LaVision GmbH) to compare results of the measured velocity profile with theory. The aim was to determine the impact of the PIV processing approach on the validity of the velocity profile in the near wall region.

Effect of different window shapes and sizes were investigated and realized that the smaller window size has more velocity profile compatible with theory near the wall, and changes in the interrogation windows do not have so much influence on the velocity profile near boundary. At the end the agreement of the

experimental results with theory is acceptable and shows different errors associated to the near boundary velocity profile in those methods.

This thesis is dedicated to my parents Tahereh and Najaf for their endless love and support, and my lovely niece Taha for the love and energy he brought us by his birth.

ACKNOWLEDGEMENTS

This thesis is submitted as partial fulfillment for obtaining the degree of Master of Science (MSc) at University of Alberta.

I would like to acknowledge all the people who spent their times with me helping me finish this project. I would like to give an especial thanks to Dr. David S. Nobes for always having hisku office door open for any discussions according to my project and finding solutions for problems depriving me of the right pass for doing experiments. His act made me realize I am real engineer and I need to find a solution by myself. I would like to thanks Dr. Subir Bhattacharjee for the financial support of the project and first guidance of this project.

I also would like to thank my friends, Sabereh, Leila, Soudeh, Neshat, Roya & Mohtada, Fatemeh & Ali, Zahra & Mohammad Hossein for the time they spent for motivating me and giving any types of support. And I also like to mention my good friend Behnam for the last five months following up my progress and useful discussions we had together in the office for writing this thesis. God preserves those who expand their knowledge and love.

The man of knowledge is the one who recognizes that what is known is very little compared to what is not known, and as a result he considers himself ignorant, and accordingly he increases his efforts to know more by going out in search of knowledge, Imam Ali (A.s.).

Table of Contents

CONTENTS

List of Tables

List of Figures

Nomenclature

Symbol/Acronym	Description	Unit
a	Particle radius	m
n	Number of particles per unit volume	$1/m^3$
p	Fluid pressure	Pa
u	Fluid velocity	m/s
u_{max}	Maximum velocity of particle in channel	m/s
u_{avg}	Average velocity	m/s
V_0	Particle volume	m^3
x	location in *X* direction	m
y	location in *Y* direction	m
z	location in *Z* direction	m
Δx	Distance a particle travels	m
μ	Dynamic viscosity	Pa.s
ρ_f	Fluid density	kg/m^3
ρ_p	Particle density	kg/m^3
λ	Wave length	m
k	Wave number	1/m
f	Fourier transform	-
f^{-1}	Inverse Fourier transform	-
s	Mean square distance passed by a particle	m
D	Diffusion factor	m^2/s
K	Boltzmann constant	J/K
T	Absolute temperature	ºk
d_p	Particle diameter	m
D_{hyd}	hydraulic diameter	m
RMS	Root mean square	-
SNR	Signal to noise ratio	-
γ_1	Skewness	-
β_2	Kurtosis	-
σ	Standard deviation	m
ε_B	Brownian motion error	m
PIV	Particle Image Velocimetry	-
PTV	Particle Tracking Velocimetry	-
µPIV	Micro PIV	-
LDV	Laser Doppler Velocimetry	-

CHAPTER 1: **INTRODUCTION**

1.1 Introduction

Microfluidics, in simple explanation, is the science of the flow inside channels of micron size including designing, manufacturing, and formulating devices and processes for this size scale. Nowadays microfluidic systems are used almost everywhere, as they are becoming a natural part of our lives. The interest in analysis of even more multifaceted biological systems such as living cells using microfabricated structures has attracted increased attention, in the past few years [1]. Thus, microfabrication technique has pierced to the science field and become a platform for understanding neurobiology, cell biology, drug delivery [1] and DNA amplification [2].

There are many advantages associated with microfluidic devices, such as the analysis of the results does not take a lot of time and also less volume of fluid is needed to run the experiment [3]. Another advantage is that less amount of energy is being used for microfluidic device fabrication and operation which is really alluring when there is a deficiency in available energy [2].

The flow in microchannels is laminar and has a small Reynolds, but measurement of the flow velocity and its profile is crucial for analyzing the flow field and comparing with available theory especially for fluids that have non-

Newtonian characteristics. Experiments can predict the flow and velocity profile better than the numerical analysis [4]. Velocity profile is used for measuring shear rate and is an important feature of the flow.

Measuring velocity in microchannels with the driving force of pressure or electroosmotic can be done using different methods and each method has its own benefits, problems and issues [5]. Nuclear magnetic resonance (NMR) is one method which can measure the fluid flow field [6], the problem associated with this method is that it has low spatial resolution [7].

The main advantage of the optical techniques for measuring velocity is that they measure the fluid velocity without interfering with the flow field [8]. Particle tracers and molecular tracers are two different optical techniques. Particle tracer methods are associated with techniques such as laser Doppler velocimetry (LDV) [9], particle tracking velocimetry (PTV) [10], and also particle image velocimetry (PIV) [11]. Overall, PIV have been used for velocity measurement more than other techniques as it is useable in microscale flows [8]. Molecular tracer is other technique which also divided to some different methods [8].

PIV is one of the powerful techniques that has been developed to measure the fluid flow [12]. Particle position is the quantity that PIV records over time and the velocity of the fluid can be derived accordingly. In this technique, small particles are embedded in the fluid to enable capturing their position using a camera. PIV has attracted much attention in the study of fluid flow and currently is one of the most widely used methods to obtain the velocity profile of a fluid flow [13].

Micro particle image velocimetry (μPIV) [14] is a useful tool to investigate fluid mechanics in microfluidic devices and it is first introduced by Santiago et al. in 1998 [14]. Visualizing the flow velocity in microchannels with the length scale of 10^{-4} m to 10^{-7} m [15] using μPIV technique is very demanding in studying fluid flow [16]. In a μPIV system, the laser light is illuminating a volume of the seeded fluid which is injected to the inlet of the microchannel with a syringe pump. The illumination at a specific wavelength is used to excite the fluorescent particles used to track the fluid motion. The fluoresced signal is captured by a CCD camera to record particle locations. The recorded images are analyzed to track particle motion using a correlation approach from which the velocity profile is obtained. Micro particle image velocimetry has some general specification like particle image velocimetry, but its optical and mechanical constrictions are different than PIV so this counted as a different technique [15].

1.2 Approach

According to what is stated about PIV and μPIV systems, in order to develop a system to observe the flow and measure flow velocity in microchannel, understanding the flow behaviour in straight microchannel is important. A micro PIV set up is developed to measure the velocity profile in microchannel, different processing schemes of analyzing experimental results are used to overcome the difficulties due to the restrictions imposed by the small length-scales. Investigations of the velocity measurements near the wall are the main focus of

the current study as that is obstruction which has hindered the progress towards understanding the velocity in such systems experimentally.

1.3 Velocity Measurement

There are a number of techniques for measuring the velocity in microchannels especially close to the channel wall. New velocimetry PIV technique using evanescent waves generated total internal reflection fluorescence microscopy (TIRFM) has finer spatial resolution and is used to measure velocity near wall up to the distance of 450 nm from the surface. This evanescent wave illumination only be used for inspecting the flows near the solid surfaces, [17], [18], so it cannot be used to measure the velocity in other regions of the flow in channel.

There are a number of reasons why PIV has become a practical method for flow velocity. The first reason is that with laser Doppler velocimetry or hot wire anemometry the velocity of the flow obtained in one point but with the PIV the velocity of the flow field in 2D or even 3D is measurable. Second reason is that the particle-based measurement is one way of not disturbing the flow by probe and producing flow blockage, and also has calibration issues. It is much easier to collect thousands of images from different position of the flow in PIV than comparing with the situation of measuring the velocity in pointwise.

When the density of the particles are low, particle tracking velocimetry (PTV) is used, but for the high image density the particle image velocimetry (PIV) is a good option. With PIV and PTV the flow field can be captured in two

dimensions. The main difficulty in PIV and PTV is to finding particles following the flow and overcoming a problem of particles rolling at boundaries.

1.4 Image Processing

In order to measure velocity of the particles, images taken by camera are being processed to enhance their quality, reduce the background noise, and become more visible. Particles which are at boundaries or some unwanted particles removed from the image by filtering the image [19]. Velocity profiles being obtained after processing the images and analyzing them with software.

1.5 Objective

The main objective of this thesis is to improve the current understanding of the velocity profile in the microchannel and to investigating issues arising when the velocity is measured near the microchannel wall. Construct a PIV technique for studying the particles motion in microchannel with pressure driven flow and look at the velocity profile near the boundary. The main focus of this research is to see how close to the wall the experiments profile coincides with the velocity profile of the theory. The technique and the schemes which are used tried to find a way of decreasing the error comes up near the wall.

1.6 Thesis Structure

This thesis deals with the investigation of micro scale flow using PIV and issues regarding to microfluidic flow. An experimental set up developed to study the velocity profile in the microchannel and validate it with theory and in the processing procedure find errors of velocity measurement near wall with PIV.

Thesis structure consists of 7 chapters and the brief outline of thesis is given as follows. Chapter 1 presents the introduction and overview of all chapters of the thesis; chapter 2 includes literature review and measurement technology. Chapter 3 discusses the experimental set up and method. Chapter 4 presents experimental set up specifications. Chapter 5 presents instantaneous results and discussions. Chapter 6 is about results and discussions. Chapter 7 is the conclusion of which is obtained from the current study. In Appendix A, different Matlab codes which are used for plotting data are attached, and in Appendix B, PIV processing schemes in DaVis software are shown.

CHAPTER 2: **LITERATURE REVIEW**

2.1 Background

Meinhart et al. [11] introduce the terms of microfluidics as a flow in systems with length scale of hundreds of micron or less. In this type of flow the forces which are important are different than the ones when the flow is at the macro scales. These forces and their interactions are a key answer to some fluid behaviors, so it is vital to study about these forces. At small length scale the ability to observe a flow compare to the volume of the fluid increases. In the microfluidic the scale is changed and because of this, many conventional diagnostic tools are not practical in micron area. Traditional flow meters which typically cause flow disturbances are inaccurate, That's why Santiago et al. [11] developed a PIV experimental technique which is applicable in microscale flow measurements.

Microfluidic systems have application in DNA separation [20], sample preparation, chemical reactions and micro pumps [21]. Microfluidic systems become of an interest in recent researches, and they become applicable in manufacturing process, biology and nanotechnology. MEMS systems for biological applications, lab-on-a-chip provides devices for the chemical reactions, Micro heat exchangers increase the heat transfer properties [22].

2.2 Measurement Technology

Different measurement techniques to measure the flow velocity have been so far developed. A list of these techniques is as follows:

- Pitot- static tube
- Hotwire anemometer
- Laser Doppler anemometry
- Particle image velocimetry
- Particle tracking velocimetry
- Digital particle image velocimetry
- Laser speckle velocimetry

In the point measurement devices like pitot-static tube and hotwire anemometer the probe causes a disturbance in the flow as it interferes with the flow field. Other difficulties with these intrusive methods are reversing flows and vortices [23]. In addition the other difficulty associated with intrusive probe is the need to calibration every time they are used and their sensitivity to temperature, humidity, etc [23].

Lasers produce a non-intrusive flow measurements technique such as laser Doppler anemometry (LDA), particle image velocimetry (PIV), particle tracking velocimetry (PTV), digital particle image velocimetry (DPIV), and laser speckle velocimetry (LSV). Yeh and Cummins [24] examine the Doppler shift with laser spectrometer in Rayleigh light and developed the laser Doppler anemometry. Advancement to LDA was considerable as the output from the transducer was linear and had the advantage of less noise and no need to calibration [23]. Progress in camera and laser technology improves the quality of flow visualization and measurement of the flow field. Particle image velocimetry (PIV)

is one of the most admitted flow measurements as it is applicable to instantaneously measurement of difficult flow filed [23]. High frame rate cameras using high frequency lasers provided the time resolved measurements [23]. Laser speckle velocimetry (LSV), similar to PIV and PTV, takes the images of the particle in the flow. The difference between these three techniques is that, PTV mainly deals with the low particle density flows, PIV is usually appropriate for medium seeding density where as LSV is mostly recommended for high seeding density [23]. In PTV, time sequence of individual tracer particles in the flow is taken in to account in order to detect individual particles and track them from one frame to another frame, this individual tracking needs small density of seeding particles. Historically, PIV and LSV give the velocity of the flow for each interrogation window by statistically measuring velocity value from many tracer particles. So PIV and LSV are identical techniques with a various seeding particles density [23]. In the next section we will present more explanation about PIV and μPIV as these two methods are the focus of the present study.

2.3 Particle Image Velocimetry (PIV)

Particle image velocimetry (PIV) is the technique that captures particle positions from the scattered light by them when they are illuminated by the laser light in to a photographic film. The procedure for measuring flow field with PIV technique is as follows: the positions of the group of particles are recorded in time t and $(t + \Delta t)$, the probable displacement of the groups of particles accounted to

be equal to Δs. The velocity of the particles by assuming no acceleration will be derived as:

$$u = \frac{\Delta s}{\Delta t} \tag{2.1}$$

Equation (2.1) is applicable for the entire flow field. What is recorded with PIV is divided into small regions called interrogation window. Particles in each interrogation cells are moving in the same direction and evenly identical spaces.

To analyze the particle images it is needed to consider the way these images have been taken by the camera. First set of images which consist of both illuminations in one frame are called single frame / double exposure. These types of images are evaluated by auto-correlation. The second sets are those which are recorded the scattered light from first illumination in one frame and those from second illumination in the other frames. This is called double frame / double exposure and is evaluated by cross correlation. Schematic figure of cross correlation is presented in Fig. 1.

Two frames are taken with camera and they divided into interrogation window spaces, sub window from the first frame in time t_1 and the other sub window from frame 2 in time t_2 are shown in Fig. 1. When these sub windows, are cross correlated the correlation function associated to the particles movement shows a peak as a measure of displacement and the displacement in that window is from the center of the correlation map out to the end position of that peak. The displacement vector for each interrogation window is shown in Fig. 1.

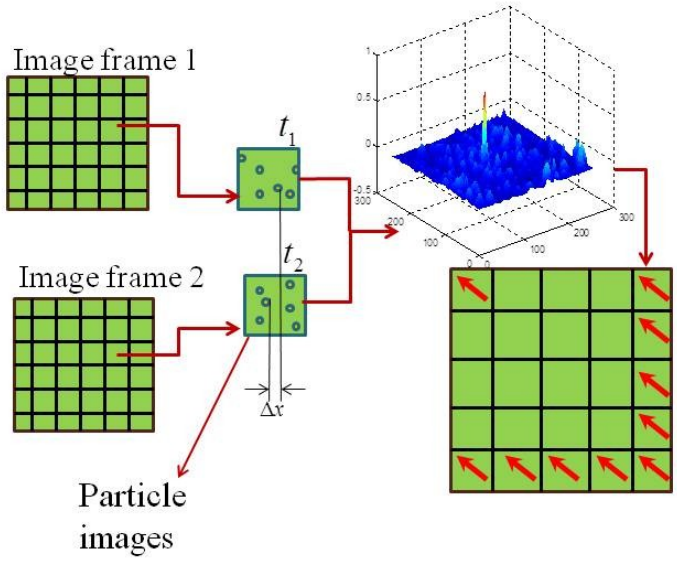

Fig. 1: Schematic image of cross correlation PIV processing.

2.4 Main Features of PIV

The main features of PIV are as follows [25]:

- **Non-intrusive velocity measurement**

In the PIV techniques for measuring velocity no flow disturbance occurs in contrast to hot wire anemometry which uses a measurement probe. This advantage increases the applicability of PIV for high speed flows or boundary layer.

- **Indirect velocity measurement**

In PIV technique the velocity of a fluid element is measured by velocity of tracer particles added to flow.

- **Velocity lag**

Tracer particles added to the flow need to follow the flow faithfully. It is essential that in each experiment the tracer particles be chosen to the extents that have the density in the same order of the flow density.

- **Illumination**

The intensities of the illuminated particles need to be high enough to be observed in the photographic film. Larger particles scatter light better than the small particle.

- **Duration of illumination pulse**

Freezing the motion of the particles in order to avoid blurring of the image is important and for that the short duration of the illumination light pulse is needed.

- **Distribution of tracer particles in the flow**

The distribution of the tracer particles in the flow should be homogeneous in PIV in order to get ideal evaluation of the velocity.

- **Density of tracer particle images**

Image density is distinguished in three different types [26], low image density is applicable to particle tracking velocimetry (PTV), medium image density is required for PIV and high image density is used by laser speckle velocimetry (LSV) technique for velocity evaluation.

2.5 Theory of μPIV Measurement

Application of μPIV is similar to PIV technique and first developed in 1998 [14] where the velocity of around a 30 micron elliptical cylinder was obtained. μPIV is used for measuring the velocity in micro scales. The μPIV system consists of a CCD (Charged Coupled Device) camera, a microscope, objective, tracer particles having fluorescent dye, and illumination light. Basic idea of μPIV is the same as PIV where the velocity of the flow is obtained by measuring the displacement of the tracer particles. When the flow observation is done in conventional PIV the laser sheet with thickness less than the depth of field of image recording system is produced near the depth of focus of the camera lens. But in micro scale flow visualization the alignment of the laser sheet is difficult, therefore the volume illumination [27] is used. The volume illumination concept is explained in the next section. Tracer particle in the fluid which moves with the flow are the main source for μPIV to measure the velocity. The size of the particles is needed to be optimum as they need to emit enough light to be captured by the camera and produce a detectable image, it should not be so large to stick to the microchannel walls, and not too small to be not able to follow the flow [11]. In this study, hollow sphere particles with the size of 6-8 μm are used which are at the applicable size for shadowgraphy.

2.6 Volume Illumination

Tracer particles in both PIV and μPIV will be illuminated and the scattered light from particles is recorded by camera. In the PIV technique the laser light

generates a thin sheet to illuminate a plane in the flow field [28]. The sheet thickness is smaller than the depth of focus of the camera, therefore all the particles illuminated in that laser sheet will be captured by CCD camera. But in μPIV the production of a laser sheet is difficult, because the length scales in microfluidic is in the order of micro meter, and the optical access in microfluidic is in one direction. In the μPIV technique a volume of the flow is illuminated and the measurement plane is determined in the focal plane of the objective [29].

2.7 Micro Channel Flow Field

Preparing a microfluidic flow cell connected to a μPIV system, creates a set-up which leads to producing a place for observing the flow. Seeded water is injected to the inlet of the microchannel with syringe pump. The laser light is illuminating the volume of the flow in the channel and exciting the particles. The excited particles emit light to the CCD camera and by analyzing the pictures from CCD camera the velocity of the particles will be obtained.

When it goes to microfluidic devices the forces or phenomena which are applicable in micron size have effect on the particle following the flow, these are such as Saffman lift, Brownian motion and electrostatic forces between liquid and solid.

2.8 Velocity Profiles in Microchannel with Circle Cross Section

The fluid flowing in the microchannel produces a profile which is obtained by considering the forces which are applying on the flow. Using the governing equations for the flow in the pipe, the velocity profile in the pipe will be obtained [30]. Two dimensional incompressible ($\frac{\partial}{\partial z} = 0$) viscous flow between parallel plates with height of *2b* is shown in Fig. 2. The flow is fully developed so it is essentially axial, i.e. $u \neq 0$ but $v = w = 0$. Continuity equation is presented in equation (2.2).

$$\frac{\partial u}{\partial x} + \frac{\partial v}{\partial y} + \frac{\partial w}{\partial z} = 0 = \frac{\partial u}{\partial x} + 0 + 0 \quad \text{or} \quad u = u(y) \text{ only} \tag{2.2}$$

From this it can be concluded that the fluid velocity just varies across the channel and flow is fully developed. Substituting the simplified velocity profile in the *x* component of the Navier-Stokes momentum equation, equation (2.3) can be obtained.

$$\rho\left(u\frac{\partial u}{\partial x} + v\frac{\partial u}{\partial y}\right) = -\frac{\partial p}{\partial x} + \rho g_x + \mu\left(\frac{\partial^2 u}{\partial x^2} + \frac{\partial^2 u}{\partial y^2}\right)$$
$$\text{or} \quad \rho(0 + 0) = -\frac{\partial p}{\partial x} + 0 + \mu\left(0 + \frac{\partial^2 u}{\partial y^2}\right) \tag{2.3}$$

Most of the terms drop out because the flow is fully developed and $u = u(y)$, thus the momentum equation simply turns to equation (2.4).

$$\frac{\partial p}{\partial x} = \mu \frac{\partial^2 u}{\partial y^2} \tag{2.4}$$

The $v = w = 0$ and gravity is neglected in the y component and z component of the momentum equation, so from those equations this is concluded that the pressure is only function of x direction only, $p = p(x)$. Therefore equation (2.4) leads to $\frac{\partial p}{\partial x} = \mu \frac{\partial^2 u}{\partial y^2} =$ constant. Now, for finding velocity the equation (2.4) needs to be solved.

$$\frac{du}{dy} = \frac{1}{\mu}\frac{\partial p}{\partial x} y + b_1$$

$$u = \frac{1}{2\mu}\frac{\partial p}{\partial x} y^2 + b_1 y + b_2 \tag{2.5}$$

At $y = \pm b \quad u = 0$ or $b_1 = 0$ and $b_2 = -\frac{\partial p}{\partial x}\frac{b^2}{2\mu}$

So, the velocity for laminar flow in the channel is presented in equation (2.6).

$$u = -\frac{\partial p}{\partial x}\frac{b^2}{2\mu}\left(1 - \frac{y^2}{b^2}\right) \tag{2.6}$$

Fig. 2 illustrates the typical parabolic velocity profile of an incompressible viscous flow between two fixed plates. This theoretical profile is used to compare with the experimental velocity profile, validating the experiment and evaluating the accuracy of the experiment.

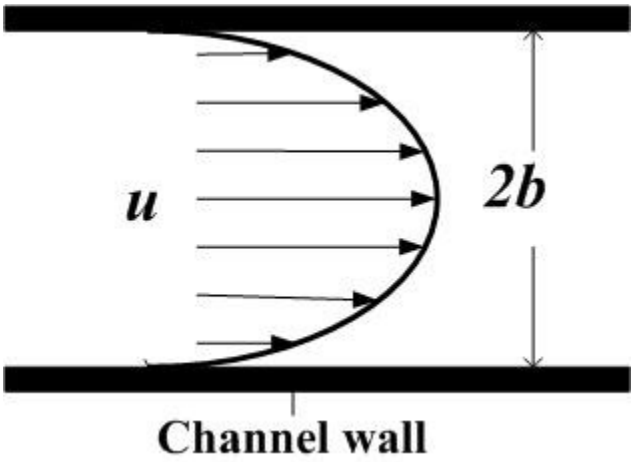

Fig. 2: Incompressible viscous flow between fixed parallel plates.

The velocity profiles at the middle position of the flow field were normalized and plotted. These profiles were fitted using the Newtonian theoretical profile. For the velocity profile of water the compliance with theory was studied. The characteristic equations for velocity profile of Newtonian fluids in a rectangular channel are well documented [30].

2.9 Scaling the Flow

When the cross section of the flow is not circle, the hydraulic diameter is used as the characteristic length scale for scaling and calculating the Reynolds number [30]. The entrance length is the distance over which the flow no longer changes along the channel. In the channel with non circular cross section the hydraulic diameter is used for the entrance length in non circular cross section channels.

$$D_{hyd} = \frac{4A}{C} = \frac{4 \times w \times h}{2 \times (w + h)} \tag{2.7}$$

$$Re = \frac{\rho v_{avg} D_{hyd}}{\mu} \tag{2.8}$$

where A is the area of the cross section and C is its perimeter.

2.9.1 Velocity profiles in microchannel with rectangle cross section

Using the coordinates as shown in Fig. 3, the theoretical velocity profile based on the solution of the Navier-Stokes equation with a no-slip boundary condition is expressed as [31], [32].

$$u_x(y,z) = \frac{4h^2 \Delta p}{\pi^3 \mu L} \sum_{n=1,3,5,\dots}^{\infty} \frac{1}{n^3} \left[1 - \frac{cosh\left(n\pi\, {}^{y}/_{h}\right)}{cosh\left(n\pi\, {}^{w}/_{2h}\right)} \right] sin\left(n\pi \frac{z}{h}\right) \tag{2.9}$$

The flow rate can be obtained by integrating the velocity profile across the channel described as:

$$Q = \int_0^{w/2} \int_0^{h} u_x \, d_y d_z \tag{2.10}$$

This gives:

$$Q = \frac{w h^3 \Delta p}{12 \mu L} \left[1 - \sum_{n=1,3,5,\dots}^{\infty} \frac{1}{n^5} \frac{192}{\pi^5} \frac{h}{w} tanh\left(n\pi \frac{w}{2h}\right) \right] \tag{2.11}$$

$$Q = Q_p \left[1 - \sum_{n=1,3,5,\dots}^{\infty} \frac{1}{n^5} \frac{192}{\pi^5} \frac{h}{w} tanh\left(n\pi \frac{w}{2h}\right) \right] \tag{2.12}$$

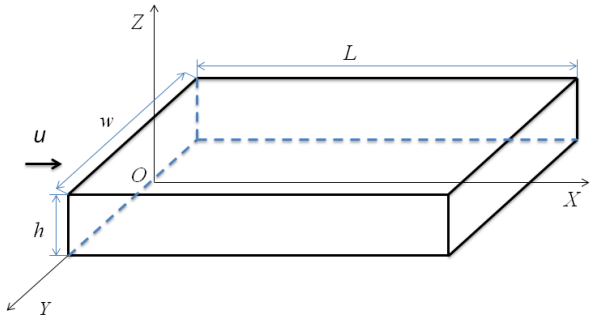

Fig. 3: Schematic diagram of the rectangular microchannel and the coordinate system, the width of the channel is *w* (*Y* direction), the height of the channel is *h* (*Z* direction)

2.10 Conclusion

The main conclusion out of using micro PIV is that it is an appropriate technique because it is used to measure the flow in two dimensions and it captures the flow velocity. Its limitation is that it should track the particles seeded into the flow[33]. With the velocity profile near the wall there is a large potential gradient of the velocity and the interrogation window cannot capture enough particles near the wall. So, near wall measurements are potentially bias based on the approach of the technique.

CHAPTER 3: **METHODOLOGY**

3.1 Introduction

The experimental set up and all the parameters and procedures used in the current experimental study are presented in this chapter. To visualize the velocity profile in microchannels experimental platform is developed and used to explore and understand the physics of the flow where it is needed to know whether the flow is laminar or turbulent. The velocity profile helps to understand the behavior of the fluid while transporting it.

3.2 Cross Correlation

The technique of PIV is the correlation method [34], correlation of two functions of $f(x)$ and $g(x)$ is the convolution product of those two functions,

$$f \star g = C_{fg}(\Delta x) = \int_{-\infty}^{+\infty} f(x)\, g(x + \Delta x)\, dx \tag{3.1}$$

$$f(x) = \delta\left(x - x_f\right)$$

$$g(x) = \delta\left(x - x_g\right)$$

then the correlation is,

$$C_{fg}(\Delta x) = \delta\left(x - x_{fg}\right)$$

with,

$$x_{fg} = x_g - x_f$$

The correlation shows a peak at x_{fg} and is zero elsewhere, this demonstration is shown in Fig. 4.

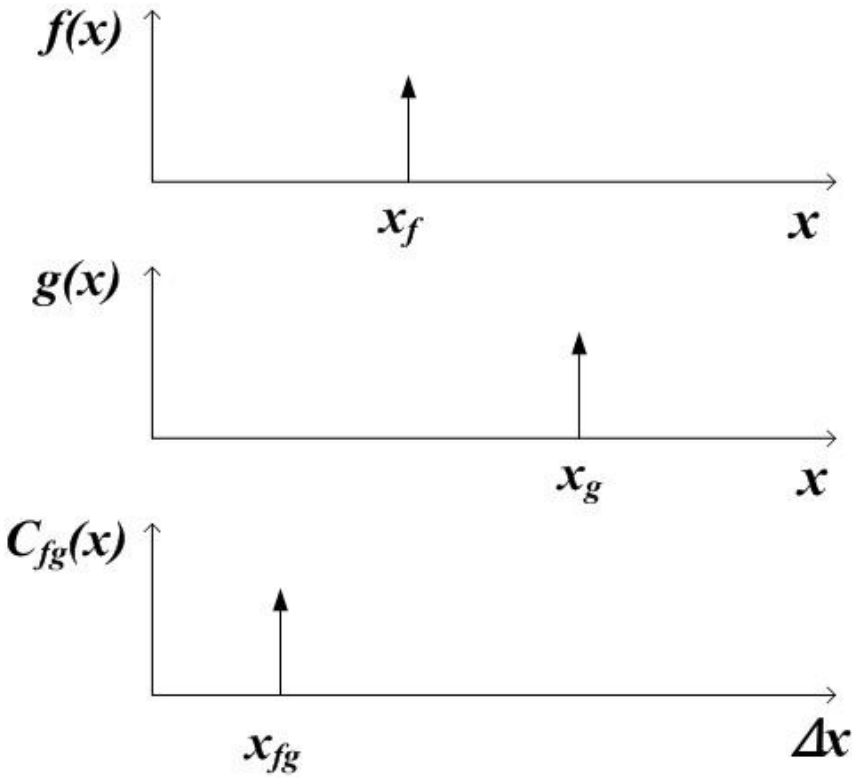

Fig. 4: Example of cross correlation with two Dirac functions.

Correlation in one dimension involves N^2 operations while in the two dimensional plane with $N \times N$ collection of points the number of operations increases to N^4 which is very large and Fourier theory [35] is used to evaluate correlations.

3.3 Correlation Theorem

Correlation theorem is obtained using Fourier theory. The equations below show how the correlation theorem is derived by applying Fourier theory. The wave number k, is a function of wavelength, λ, as

$$k = 1/\lambda \tag{3.2}$$

The Fourier transform, f, and the inverse Fourier transform, f^{-1}, is defined as:

$$H(k) = f[h(x)] = \int_{-\infty}^{+\infty} h(x)\, e^{2\pi i k x} dx \tag{3.3}$$

$$h(x) = f^{-1}[H(k)] = \int_{-\infty}^{+\infty} H(k)\, e^{-2\pi i k x} dk \tag{3.4}$$

The correlation will be,

$$C_{fg}(\Delta x) = \int_{-\infty}^{+\infty} f(x)\, g(x+\Delta x)\, dx$$

$$= \int_{-\infty}^{+\infty} \left(\int_{-\infty}^{+\infty} F(k)\, e^{-2\pi i k x} dk \int_{-\infty}^{+\infty} G(k')\, e^{-2\pi i k' \Delta x} e^{-2\pi i k' x} dk' \right) dx$$

$$= \int_{-\infty}^{+\infty} \left(\int_{-\infty}^{+\infty} F(k)\, e^{-2\pi i k x} dk \int_{-\infty}^{+\infty} G(k')\, e^{-2\pi i k' (\Delta x + x)} dk' \right) dx \tag{3.5}$$

$$= \int_{-\infty}^{+\infty} \int_{-\infty}^{+\infty} F(k)\, G(k')\, e^{-2\pi i k' \Delta x} \left(\int_{-\infty}^{+\infty} e^{-2\pi i (k'-k) x} dx \right) dk dk'$$

$$= \int_{-\infty}^{+\infty} \int_{-\infty}^{+\infty} F(k)\, G(k')\, e^{-2\pi i k' \Delta x} \delta(k'-k)\; dk dk'$$

$$= \int_{-\infty}^{+\infty} F(k)\, G(k)\, e^{-2\pi i k \Delta x}\; dk$$

$$= f^{-1}[F(k)\, G(k)\,]$$

This, $f^{-1}[F(k)\, G(k)\,]$, is known as the correlation theorem. This theorem is also the same for two or more dimensions and the procedure is analogues to equation (3.5) just use vectors equivalent of *x* and *k* instead of *x* and *k*. Correlation is evaluated using equation (3.5) and fast Fourier transform (FFT's).

3.4 Data Acquisition

3.4.1 Triggering

Initially, a function generator (Model: AFG 3022B Dual Channel Function Generator; Tektronix Inc.) was used to send continuous pulses at 40 Hz, with an amplitude of 5 Vpp, an offset of 2.5 V and a 2 % duty. Later a continuous square wave was sent to the camera and the LED light source at frequencies between 1 and 90 Hz, with amplitude of 5 Vpp, an offset of 2.5 V and an adjustable phase difference to synchronize the light pulses to the camera captures.

3.4.2 Parameters

An in-house program built using CVI was used to collect data. Initially, a continuous exposure mode was selected for the white light source. Later, the system was moved on to a timed exposure of 50 μs. The gain settings were played for a well-lit shot. Generally, gain was set between 100 and 200.

3.5 PIV Technique

The software used for applying Particle Image Velocimetry was a commercially available package (DaVis 8.1.4. LaVision). PIV technique consist of different steps, such as calibration, image acquisition, image preprocessing and image post processing which are explained in details in the next sections.

3.5.1 Calibration

Since images taken by the camera are in pixels, a calibration factor was needed to convert the data in the images to the real space. By using a multi function calibration target (Model: DA029, 4X to 20X) the entire image from pixels convert to real dimensions. The layout was a 4.5 mm square grid with line thickness of 20 μm, which were 250 μm apart. Calibration was carried out in commercial software (DaVis 8.0.7. LaVision) and the calibration factor is 1.22 which is used in converting pixels to real space.

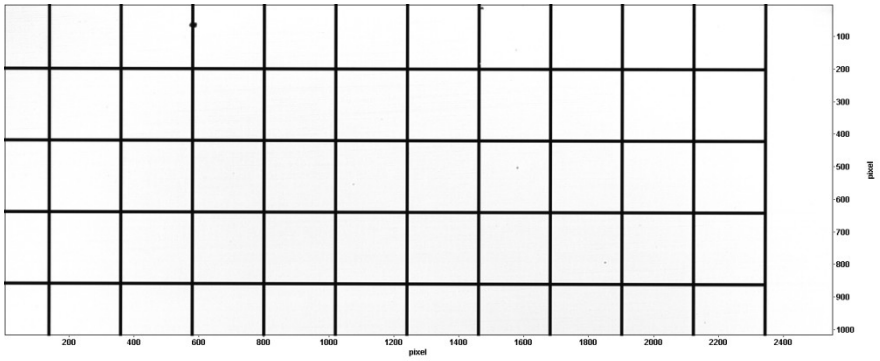

Fig. 5: Calibration target image from Davis

3.5.2 Image Acquisition

A timed series of 1000 images were collected in *.avi format. The video was then imported into DaVis to apply PIV processing. The locations of the channel walls were observed in the images and the exact width of the channel was found out to be 0.831 mm. The image size of the seeding particles was around 3 to 4 pixels. The displacement of the particles between two successive frames was around 3 to 5 diameters[36].

3.5.3 Image Preprocessing

Image preprocessing is applicable for removing noises in the background of the image and letting the particles be obviously distinguished. The preprocessing of the image was done by the Davis. Background noise was reduced by using a sliding minimum subtraction algorithm[37]. A recipe was developed for pre-processing of the images to reduce background noise and increase clarity. First, the images were inverted to counter the blotchy grayish background. Afterwards a non-linear filter with a sliding minimum algorithm was used to subtract the minimum intensity from the middle of each window. The selected window size was 5×5 pixels, which was bigger than the particle, in order to avoid subtracting from the particle images. The intensity of the frames was increased by a multiplication factor of 2, which increased the intensities. Finally, a linear filter was applied. Fig. 6 and Fig. 7 present the particle position in the channel before and after preprocessing.

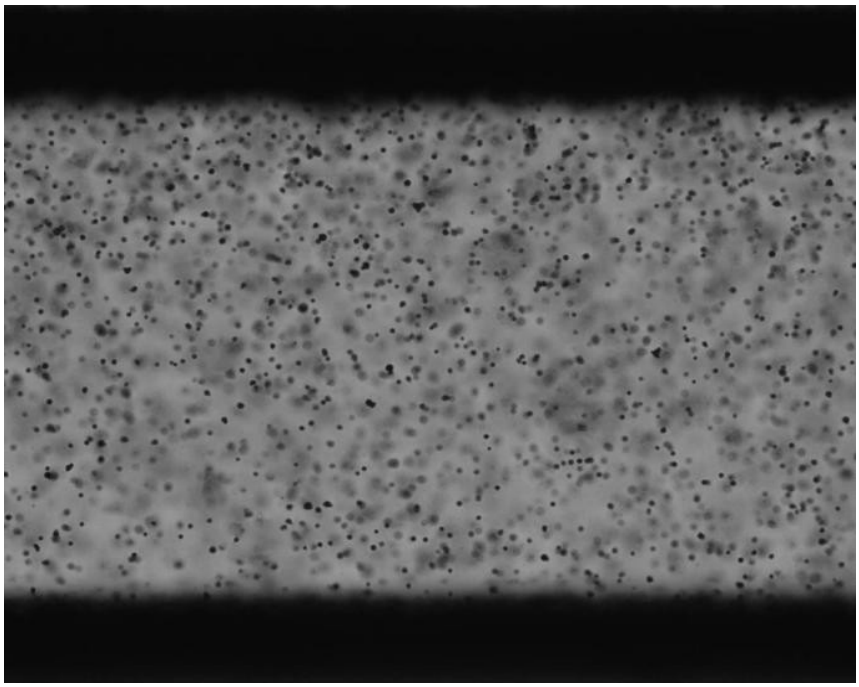

Fig. 6: Particle within the flow in the channel before pre processing

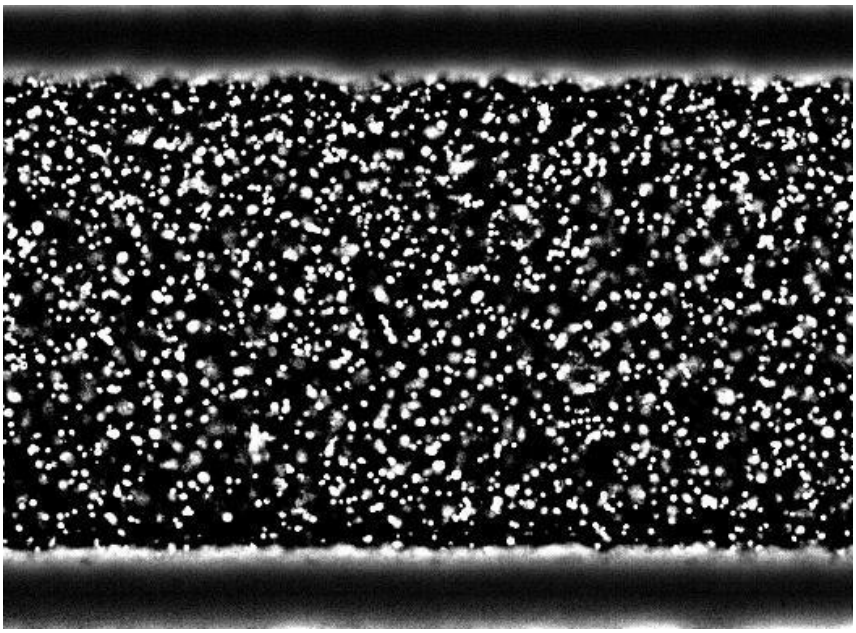

Fig. 7: Particle within the flow in the channel after pre processing

3.5.4 Processing

A cross-correlation PIV technique was applied on the pre-processed images. Elliptical with aspect ratio of 4 and 2, and square interrogation windows were used to break down the entire image. A multi-pass algorithm was used. The scheme of how using multi pass algorithm is explained for each image individually. The cross correlation was performed in two passes, in each set of processing scheme the first pass interrogation window size was bigger than the second pass interrogation window. For example if the first pass interrogation window is 64 × 64 pixels with 50% overlap between the interrogation windows, the second pass was performed with 32×32 interrogation window with 50 % overlap. The window sizes were selected based on analysis of correlation map. The vectors were then averaged in DaVis.

3.5.5 Interrogation Window

Two types of interrogation windows (square and elliptical shape) were used for investigation of particles on the image. The elliptical interrogation window also has two types, one with the aspect ratio of 4 and the other with the aspect ratio of 2. These interrogation window shapes are shown in Fig. 8.

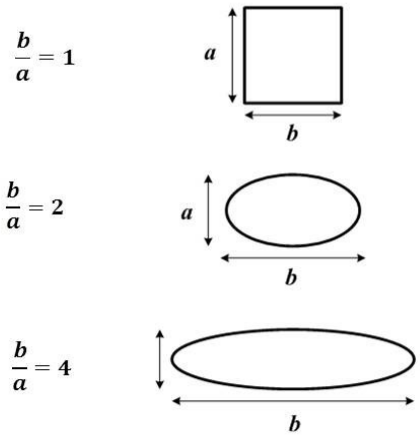

35

Fig. 8: Three types of interrogation windows used in DaVis software, square, elliptic with aspect ratio 2 and elliptic with aspect ratio 4

In PIV processing the errors rises up when the processing goes near the boundaries as the interrogation windows near the wall interfere with the boundary and enough particles for cross correlation are not available in the interrogation windows. These different interrogation windows were introduced to investigate the effects of enlarging the sizes of the window along the boundary and comparing the velocity profiles processed with each of these windows near the boundary. The size of interrogation window was selected to capture the particles and movement of the particles, it should be taken in to account that there is limitation about the extension and compression of interrogation window sizes and

they cannot be so large or so small because enough amount of particles should be captured inside them.

3.5.6 Post Processing

After obtaining the velocity vectors using DaVis, the *.VC7 files were imported to Matlab R2009a (The Mathworks Inc.) to obtain further plots and calculating average velocity using the PIVMat toolbox. In post processing process, groups of vectors less than five were removed, if there be some empty spaces without vectors, those places would be filled up. The other process which was done in post processing was the smoothing of vectors obtained from raw images.

3.5.7 Brownian Motion

Fluid with the suspended particles experience a random motion called Brownian motion, and this type of motion is typically more considerable in micro PIV applications where small particles are moving at low velocities. Brownian motion causes a higher error when the size of the particles decrease and the velocity is low (e.g. in the order of micron per second) [14]. One case that Brownian motion has effect in micro PIV is on correlation function which increases the noise peaks and make it difficult to find the correlation peak among noise peaks [38]. One way of omitting the effect of Brownian motion is to increase the seeding particles size. Decreasing the time interval between two

consecutive laser pulses [38] will help to pass over the noise peak. Sources of errors with using micro PIV technique mainly focus on particle migration [39].

The mean square distance passed by a particle due to diffusion can be calculated as is in equation (3.6) according to Santiago et al [14].

$$s^2 = 2D\Delta t \tag{3.6}$$

D is the diffusion factor and Δt is the time over which particles travel [40] .

$$D = \frac{KT}{3\pi\mu d_p} \tag{3.7}$$

In equation (3.7), K is the Boltzmann constant, T is the absolute temperature, μ is the dynamic viscosity of the fluid, and d_p is the particle diameter. The velocity of particles which travel a distance Δx in the time interval of Δt can be obtained as:

$$u = \frac{\Delta x}{\Delta t} \tag{3.8}$$

So, error due to Brownian motion is

$$\varepsilon_B = \frac{\langle s^2 \rangle^{\frac{1}{2}}}{\Delta x} = \frac{1}{u}\sqrt{\frac{2D}{\Delta t}} \tag{3.9}$$

3.5.8 Saffman Lift

The Saffman lift is the lift that a particle in the shear rate part of the flow experiences when the particle velocity is different than the fluid velocity. Saffman lift is shown in Fig. 9. When the fluid velocity is greater than the particle velocity

then the Saffman lift is in the positive *y*-direction. The Saffman lift can have significant effect on the particles near the walls or other type of boundary. The particle concentration near the wall is much less than the centre line. This lower concentration of particles near the wall cause much higher error for velocity measurement, because less amount of particles are captured in the interrogation windows for PIV processing and getting correlation functions. This error can be decreased by producing some synthetic particles near the wall while doing PIV processing. This method will eliminate the problem of not having enough particles in the interrogation window.

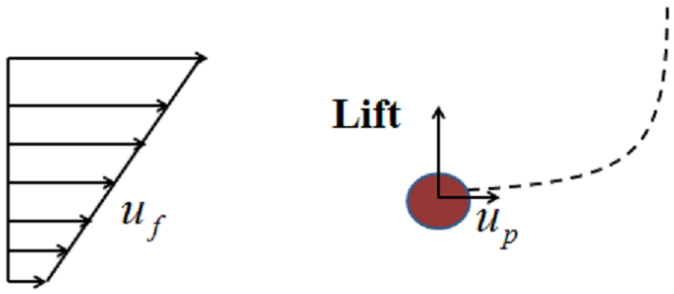

Fig. 9: Schematic of particle in the shear flow near the wall and Saffman lift on the particle

3.6 PIV Uncertainties

Noise in PIV is not eliminated and is inherent to PIV data. Different sources of noise come from optical distortion, transfer function of CCD, light illumination, non-homogeneity, particle characteristics, and speckle etc. As PIV is based on the statistical correlation of imaged sub-regions to determine local flow

velocities, it is subject to inherent errors that arise from finite tracer particle numbers, sample volume size and image resolution. Furthermore, during data processing peak fitting algorithm, image interpolation and peak deformation may cause systematic errors risen up [41].

3.6.1 Errors Due to Calibration

Calibration error is the first major source of bias errors. If the calibration process has some error, that error will be carried in to a measurement as a bias error. Sources which might cause errors in the calibration are listed below:

- Vibration: external vibration during calibration
- Optical distortion: any distortion on the optics used on illuminating light
- Lens distortion: image quality related to the lens which used for taking the image, any distortion on lens may cause a lower image quality
- Target: its manufacturing is important for preventing the probable errors

3.7 Environmental Errors

Environmental error is one of the important precision error sources. Some of environmental errors are background, electrical, thermal and external noise. Experiments and measuring systems normally operates under the electric and magnetic field caused by sources such as building wiring and local radio stations.

3.8 Statistical Processing of Velocity

In this section, the required formulas to quantify measurement errors and also random errors are presented. There are different types of calculations to obtain the errors associated with data which are explained in the following paragraph. Some part of the error analysis done by taking the measurements repeatedly and capturing sets of samples for the error analysis.

3.8.1 Standard Deviation and Standard Error

Although it is desirable to have an identical measurements in an experiment, there are always random variations in measurements by repeating the experiments Having samples for quantities repeatedly and obtaining measurements of $(x_1, x_2, \dots, x_N)$ gives us random variations [42] in measurements. To overcome the variation in measurements, the mean of all the measurement results is taken as it is shown in equation (3.10):

$$\bar{x} = \frac{\sum_{i=1}^{N} x_i}{N} \tag{3.10}$$

Having a sample mean as the value that is used for showing the individuals deviations, helps finding value of another errors. So summed square deviation of individuals from the mean can be good representative of the result's uncertainty.

There will be another parameter which can be derived from equation (3.11) and called root mean square [43] and it shows a deviation that a single measurement has from the mean value. Standard deviation is a slightly larger

estimate of individual measurements deviation from the mean and is shown in equation (3.12)

$$\text{RMS} = \sqrt{\frac{1}{N}\sum_{i=1}^{N}(x_i - \bar{x})^2} \tag{3.11}$$

$$\text{std. deviation} = \sigma = \sqrt{\frac{1}{N-1}\sum_{i=1}^{N}(x_i - \bar{x})^2} \tag{3.12}$$

Standard deviation is normally used to calculate how much far from the mean a single measurement is probable to fall. The final step after standard deviation calculation is to introduce standard error [42] which is used to evaluate the difference of mean from the true value. Having sample variation leads to calculate the mean of repeated trials and in this case standard error is a good quantity to estimate the uncertainty of the mean. Standard error is shown in equation (3.13).

$$\text{std.}\, error = \frac{\sigma}{\sqrt{N}} = \frac{\sqrt{\frac{1}{N-1}\sum_{i=1}^{N}(x_i - \bar{x})^2}}{\sqrt{N}} \tag{3.13}$$

Standard deviation is more familiar term than standard error and most of the software packages use standard deviation, but giving a mean value plus or minus standard error is an accurate way of indicating a measurement results.

3.8.2 Skewness and Kurtosis

In experiments, true errors can only be captured by replication of experiment. Skewness and kurtosis are two types of measuring variance of the experiment data. Skewness is calculated based on equation (3.14) and measures how symmetrical the distribution is. A symmetrical data points have zero skewness. When the skewness is positive the data points are distributed to the right and with the negative skewness the distribution skewed to the left compare to symmetry [44].

$$\gamma_1 = \frac{\frac{1}{n}\sum_{i=1}^{n}(x_i - \bar{x})^3}{(\frac{1}{n}\sum_{i=1}^{n}(x_i - \bar{x})^2)^{\frac{3}{2}}} \tag{3.14}$$

where $x_i$are the data-points, $\bar{x}$ is the mean of the data-points and n is the number of data-points.

Kurtosis of the residual of fitting can be calculated based on equation (3.15). Kurtosis shows the difference of the distribution of data points from Gaussian distribution. When the kurtosis is equal to 3 the data points have a normal Gaussian distribution, with the kurtosis smaller than 3 ($\beta_2 < 3$) the distribution is most likely flatter than the Gaussian distribution and with the kurtosis larger than 3 ($\beta_2 > 3$) the distribution is more peaked than the Gaussian one [45].

$$\beta_2 = \frac{\frac{1}{n}\sum_{i=1}^{n}(x_i - \bar{x})^4}{(\frac{1}{n}\sum_{i=1}^{n}(x_i - \bar{x})^2)^{\frac{4}{2}}} \tag{3.15}$$

Skewness and kurtosis of the data performed on the dataset shown in Fig. 49 to Fig. 51. Skewness is closed to zero and it means that data are not skewed to the left and right direction from symmetry. Kurtosis has a positive value in all

interrogation window shape analysis and it means that the distributions of data are more peaked than the Gaussian distribution.

CHAPTER 4: **EXPERIMENTAL SET UP COMPONENTS AND SPECIFICATIONS**

4.1 Components of Flow Loop

In this section, the components of the experimental set up are introduced and there be an explanation about each component, which is indicated in the experimental set up Fig. 11. Another part includes explanation of the manufacturing process of flow cell. These experimental apparatus were used to investigate the flow behavior in the microchannel. The aim of this chapter is to specify the parameters on the system which effect on experimental set up.

4.2 Experimental Set up

For understanding and visualizing flow velocity in microchannel an experimental set up is produced to capture the flow in the microchannel. This set up allows the visualization of the particle in the flow with the driving force of pressure. A schematic diagram and a picture of the set-up are shown in Fig. 10 and Fig. 11. In our PIV system the shadowgraph Image of the flow with seeded particles is captured using CCD camera, The difference between the PIV and Micro PIV is that in micro PIV the illumination system is volume illumination and thin focal plane of the objective is used to control the measurement, whereas the normal PIV uses the laser sheet and locate that in the *z* direction of the flow field. The syringe pump is used to flow the fluid with seeding particle into the microchannel.

Pulsed illumination was used to freeze the motion of particles seeded in the flow. For flow illumination a high power light emitting diode (LED)[46] (SL112-520nm, Advanced Illumination) is driven by a high current driver (S320, Advanced Illumination) for the time which was required for light pulses[47]. As shown in Fig. 10 bright-field illumination or imaging in shadowgraph was used. A configuration of optics is used to form Köhler illumination [48] which is used for illuminating the sample extremely even and with high contrast over the focal plane of the imaging system.

A high resolution camera captures the images of the illuminated particles, and these images used in the processing schemes. Specifications of these devices which are used in the set up are discussed in the following paragraphs.

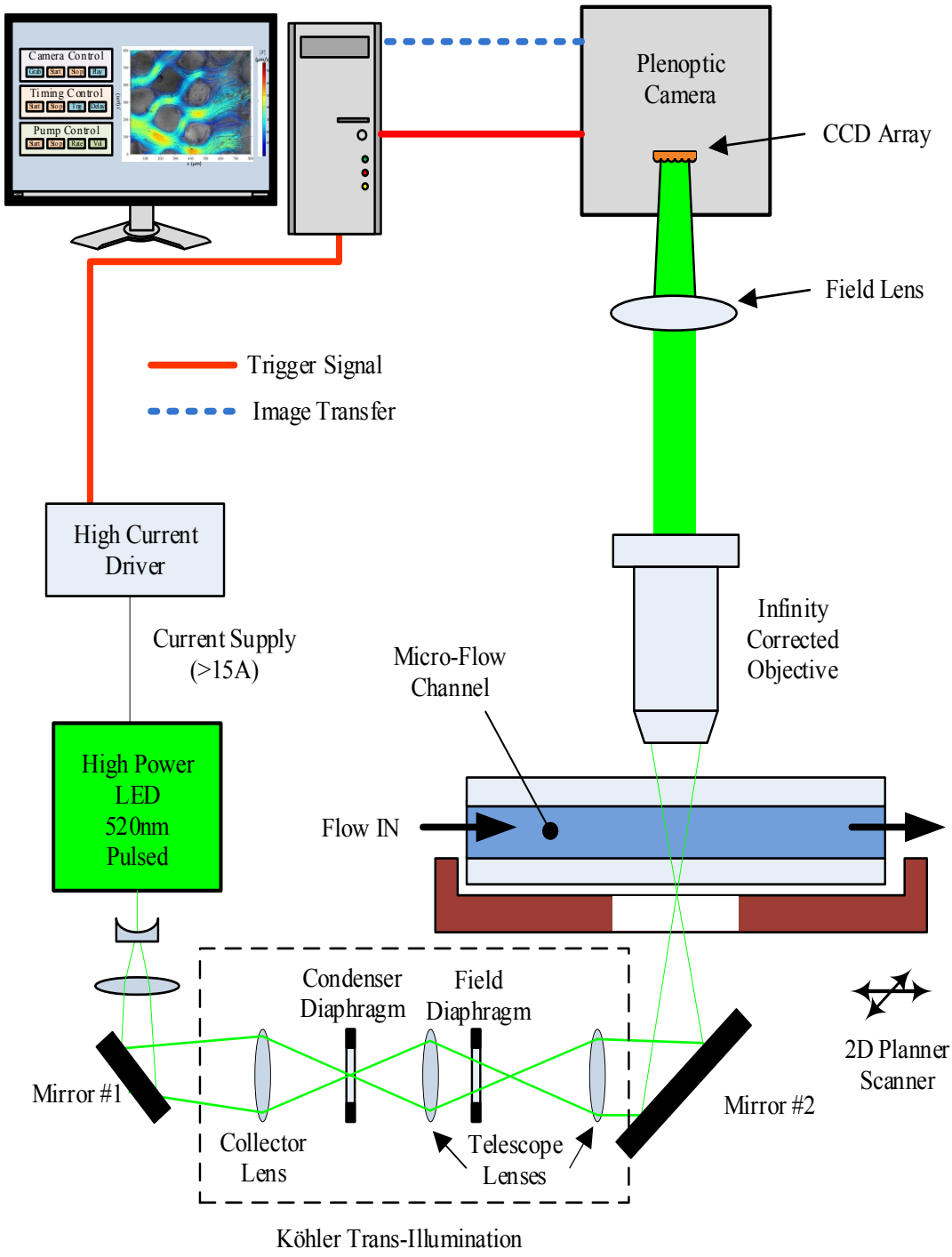

Fig. 10: Schematic of the main experimental component [46]

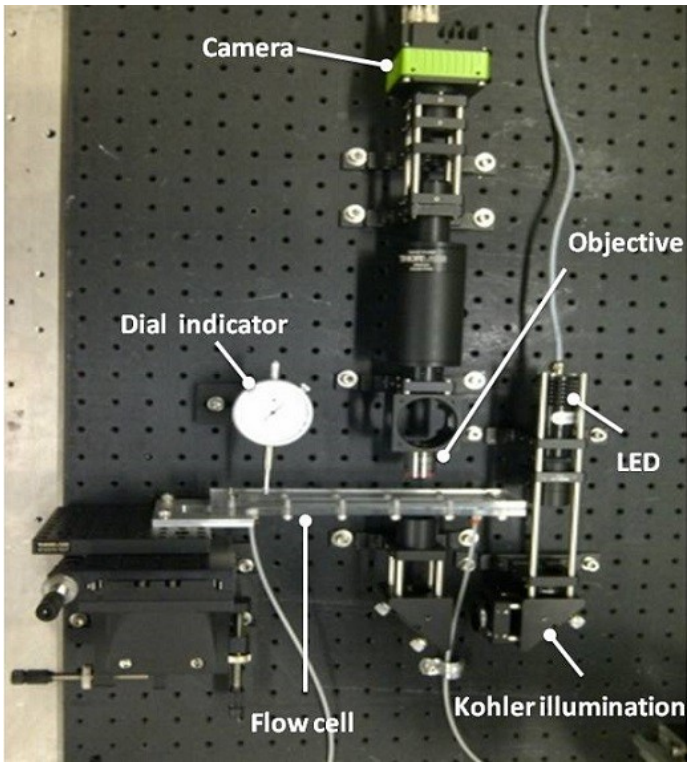

Fig. 11: Digital image of the experimental set up

4.3 Illumination System

Images of the flow with particles can be observed by camera when enough light emitted to the camera objective. LED light is used as an illumination which expanded and directed toward the Kohler illumination system and illuminated the flow cell.

4.4 Flow Cell

The flow cell is designed and built in the MECE department's machine shop has the specification as follows: chip with the length of 170 mm, width of 1 mm, thickness of top and bottom layer of 3.175 mm. There are bolts around the flow

cell holder as it is shown in the Fig. 12:, these bolts are 3/16” and ten bolts with the distance between of 54 mm are designed and fabricated on the flow cell. Inlet / Outlet Diameter (centre is 30 mm away from an edge of the smaller wall; in the channel) is 3mm.

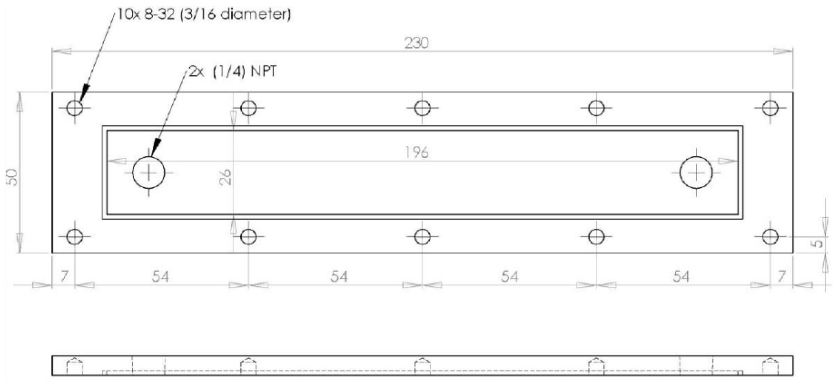

Fig. 12: Solid works plan of the top(inlet) of the flow cell

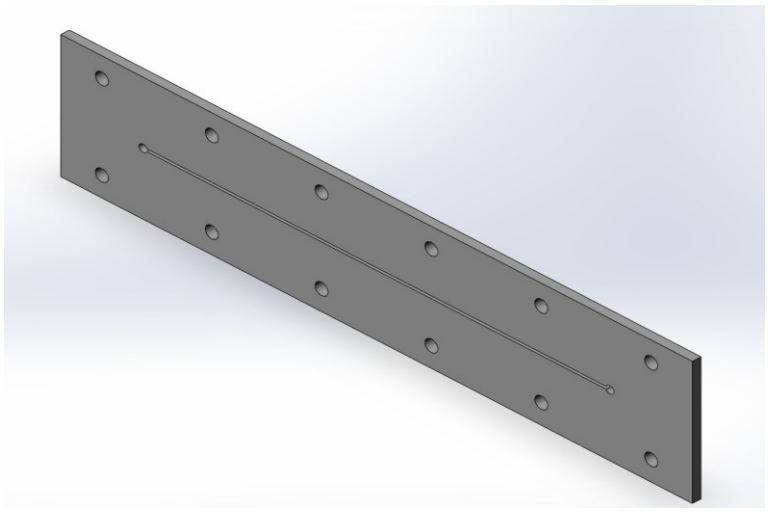

Fig. 13: Solid works plan of the channel, inlet and outlet of the flow cell

4.5 Laser Cutting

Acrylic sheets made of PMMA (Model: Optix; Vendor: Plaskolit Inc.) were used as chip material. A laser cutter (VersaLaser VLS Version 3.50; Universal Laser Systems) was used to cut the solid design with the SolidWorks plan. Laser cutter has a 50 W carbon dioxide laser with a 10.6 μm angle. It has a work area of 24" × 12". The maximum permissible part size and weight are 26.75" × 14.5" ×14" and 9 kg, respectively.

A number of adjustments have to be made to the Solid Works drawing file before it can be imported to the Versa Laser. The drawing sheets have to be scaled 1:1 and notations, dimensions and any marks, which should not be cut, have to be removed. The line thickness has to be 0.05 mm for the Versa Laser to recognize them as vectors and start cutting them. The line colors have to be changed according to the Versa Laser's cutting order shown in Fig. 14 and the order is black > red > green > yellow > blue > magenta > cyan > orange, which means that the first line which is cut is black, and the rests are in the order as it is written. Also, any line which needs to be cut as a raster has to be made black.

After making the necessary changes to the drawing file, it has to be imported to the Universal Laser Systems Control Panel. The laser properties have to be adjusted so that each color is assigned with desired power and speed. According to our observations, for a deeper or through cut, using more number of passes at lower power settings makes a cleaner cut without leaving burrs and smoother channel as compared to a single pass at a higher power.

Fig. 14: Versa laser setting used for cutting channel and chip

4.6 Chip Joining

The different parts of the chip which were cut with Versa laser are needed to join and form a flow cell. Different bonding methods examined to find a good method of joining chips.

4.6.1 Bonding Chip

The three layers were cleaned with warm, soapy water and dried with a lint-free towel to remove marks and oil residues from fingers. After this, the layers were heated at around 50 – 60°C using a hotplate (1103 Jenway Hotplate) and

Stirrer (Jenway Scientific Equipment) for around 15 minutes to straighten them out and remove warps.

For the first design with injection holes, a BD 3 ml needle with a 1 mm inlet hole was used to inject fast-setting, thin, clear glue (LePage Super Glue Ultra Gel Control). The problem of this technique was that the glue could not be injected uniformly to cover the entire surface. Also, the glue would overflow and cover a fair portion of the top surfaces leading to fogginess and stickiness. The thinness of the glue also made it seep into the channel and block them while bonding other parts.

To overcome these difficulties, etches were developed on the top and bottom layers so that the extra glue would pass in to etches instead of seeping into channel and blocking them. A small amount of glue was spread over the surfaces using a paint brush. The surfaces were arranged with the channel sandwiched in between the top and bottom layers. This type of acrylic glue joins by melting the contact surfaces and creating chemical bonds between them. The chip was then clamped and left overnight for the bonds to cure. The gluing technique turned out to be highly reliable with extreme precision required to coat the surfaces without blocking the channel.

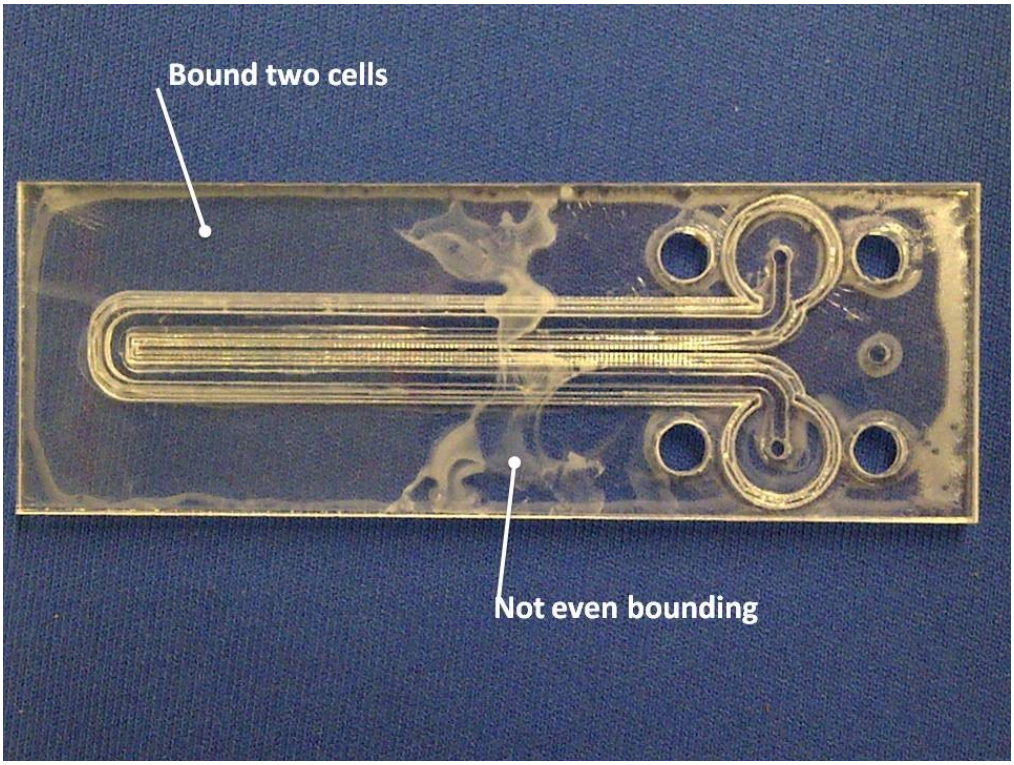

Fig. 15: Bound two parts of the chip with glue

4.6.2 Mechanical with O-ring

The chip has two o-ring grooves on the top and bottom layers. Two 1 mm nitrile o-rings were used to seal the channel. Twelve #10-24 hex socket cap-head cap screws were used to fasten the layers. This technique of assembling the chip turned out to be the most efficient with minimal leakage.

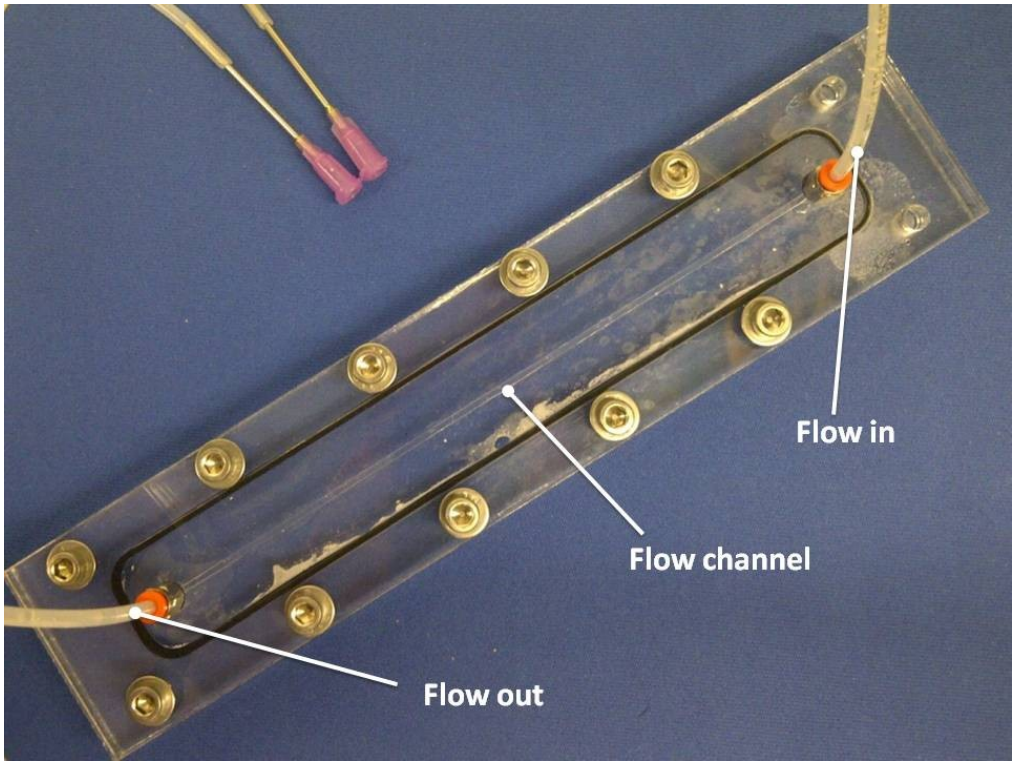

Fig. 16: Flow cell showing the flow channel and flow in and out

4.7 Chip Holder

The chip was bolted to a stainless steel holder. The holder was mounted on a traverse which could move in three different planes. The holder assembly is shown in Fig. 17. The channel inlet and outlet holes were sealed with o-rings (0.06 X 0.06 E70 (-003) EPDM 70A). The inlet and outlet connections were made using stainless steel Swagelok tube fittings (SS Swagelok tube Fittings, Male Connector, 1/16" Tube OD X 1/16" Male NPT) for 1/16" tubes. The inlet and outlet connections were made using brass push-to-connect straight adapter (Push-to-Connect Tube Fitting for Air and Water, Straight Adapter for 1/8" Tube OD X 10-32 UNF Male) for 1/8" tubes. The SolidWorks designs of holder and male

connector are shown in Fig. 17and Fig. 18. Fig. 19 presents the assembly of the holder with the male connector for the experimental set up.

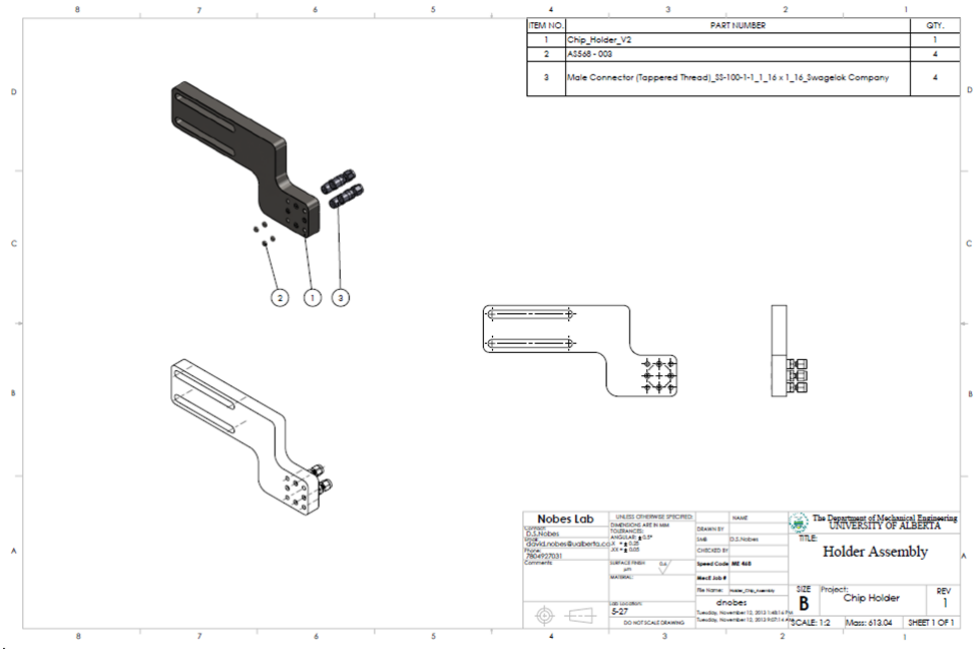

Fig. 17: Holder of chip assembly SolidWorks design

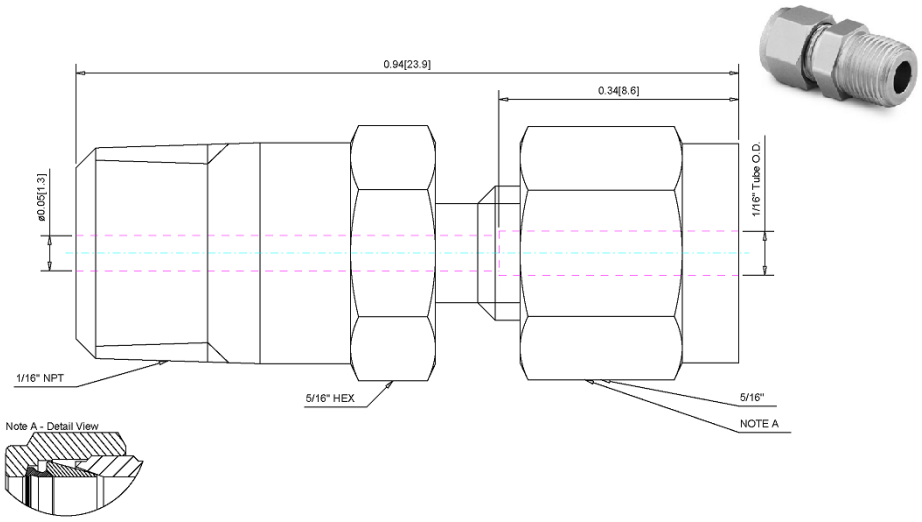

Fig. 18: Small chip male connector SolidWorks design

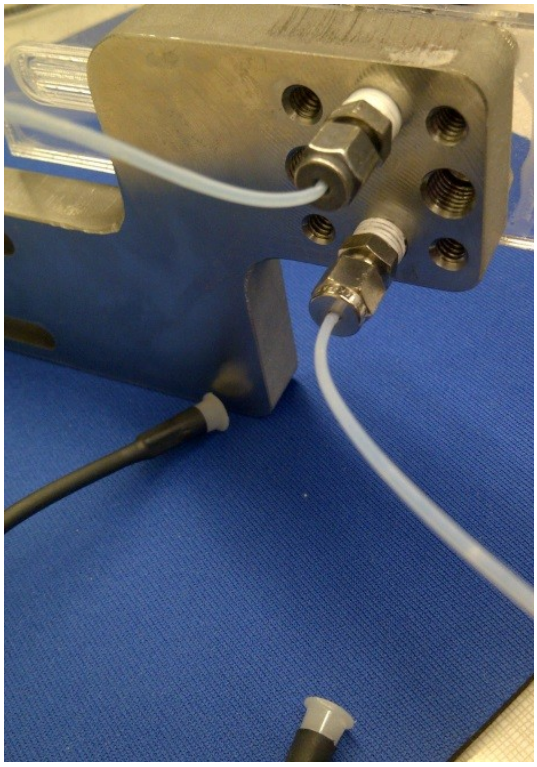

Fig. 19: Small chip male connector in the experiment

4.8 Syringes and Syringe Pump

Initially a plastic syringe (60 ml B-D plastic disposable syringe, Luer-lock tip) was used. The seeding particles were seen to stick to the syringe walls thus breaking the homogeneity of the solution. Also, during transportation of bigger particles, the latter clumped near the syringe outlet and generated uneven pressure leading to flow stoppages and back flows. So, the syringe used was shifted to a glass syringe (Gastight R #1001 Hamilton Co., Reno, Nevada, made in USA, 1000 µl) with diameter of 4.61 mm and the area of 16.64 mm^2which eliminated most of slip sticking problems and leads to a much smoother, and uniform flow.

The fluid is pumped with syringe pump (PHD 2000, Harvard Apparatus) into the channel.

4.9 Camera

The image system of the experimental set up consists of a camera, objective lens and illumination system. Camera is used to capture the images of the particles along the flow field. Camera in this experiment has specifications, which are available in Table 1. The camera is capable of capturing images at 134 frames per seconds at 2560×2048 pixels resolutions, but in this experiment it runs at 90 frames per seconds (with 2500×1000 pixels resolutions). Camera which is used for this set up has specifications and attributes, which are available in Table 1 and Table 2.

Table 1: JAI SP-5000M Camera specification

Manufacture	Model	Total Pixels	Resolution
JAI	SP-5000M-PMCL/SP-5000C-PMCL	5,242,880	2560(h) 2048(v)
Sensor Size	**Pixel Size(μm)**	**Frame Rate(fps)**	**Sensor Type**
16.75mm	5(h) 5(v)	134	CMOS
Shutter Speed(μs)	**Interface**	**A/D Bits**	**Voltage(VDC)**
10(min)/8,000,000(max)	CamLink	12	12-24

Power(watts)	Lens Mount	Weight(grams)	Shutter Type
4.5	C	215	Global

Table 2: Experimental JAI SP-5000M Camera Attribute

Exposure mode	Timed
Frame start trigger mode	On
Exposure time	50 micro sec
Power over camera link	On
Gain	200 units

4.10 Objective Lens

Another part which is used for the image capturing side of the set up is objective lens. Camera has used an objective lens with the magnification of 10× (Model: PLN; Vendor: Olympus) with a numerical aperture of 0.25 and a working distance of 10.6 mm. Depth of field associated with this objective is 8.5μm. This objective lens is used to enlarge the particles' sizes in the image and make them visible to the naked eye.

4.11 Kohler Illumination

The experimental illumination system had been set up using Kohler configuration [49]. The primary advantage of Kohler illumination is that the sample is illuminated extremely evenly and has high contrast. So this provides an evenly distributed intensity over the entire resolution of the image.

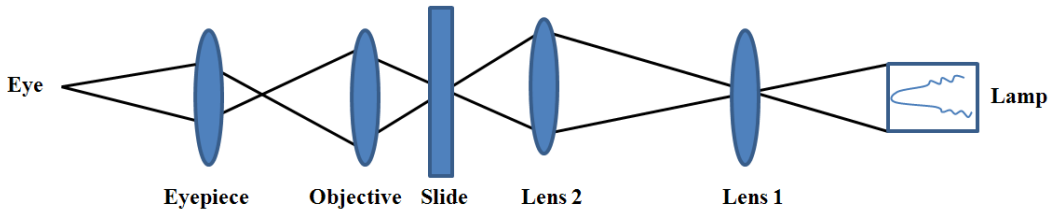

Fig. 20: Kohler illumination configuration of lenses and objective for the light source.

An image of bright-field illumination is shown in Fig. 21. This type of illumination uses components, which are available in the Fig. 20. A collector lens was used to capture light from the illumination source of the LED and focus it onto a condenser diaphragm lens 1. The latter, in turn, was used to affect the amount of light passing through the system. Condenser lens 2 and field diaphragm were used to capture the light and re-image it into the region-of-interest without refocusing it. This was then collected by the microscope objective. The positions of the various components for the Kohler illumination and the distances between them were calculated and available in Table 3:

Table 3: Kohler illumination parameters and formulas

D_{L1}	Diameter of Lens 1		mm	25.40
D_{L2}	Diameter of Lens 2		mm	25.40
FL_1	Focal Length of Lens 1		mm	45.00
FL_2	Focal Length of Lens 2		mm	40.00
D_{source}	Source Diameter		mm	5.00
d_1	Source to Lens 1 Distance	$d_1 = FL_1\left(\frac{D_{source} + D_{L2}}{D_{L2}}\right)$	mm	53.86
d_2	Lens 1 to Lens 2 Distance	$d_2 = \frac{d_1 \times FL_1}{d_1 - FL_1}$	mm	273.60
d_3	Lens 2 to Spot Diameter Distance	$d_3 = \frac{d_2 \times FL_2}{d_2 - FL_2}$	mm	46.85
D_{spot}	Spot Diameter	$D_{spot} = \frac{D_{L1} \times FL_2}{d_2 - FL_2}$	mm	4.35
NA_{input}	Input Numerical Aperture	$NA_{input} = sin\left(tan^{-1}(\frac{D_{L1}}{2*d_1})\right)$		0.23
NA_{output}	Output Numerical Aperture	$NA_{output} = sin\left(tan^{-1}(\frac{D_{L2}}{2*d_3})\right)$		0.26
		System Length = $d_1 + d_2 + d_3$	mm	374
NA		Olympus *x*4	mm	18.5

An image of this illumination technique is shown in Fig. 21 with corresponding intensity distribution profiles across the centre of the image in Fig. 22. When using Kohler illumination the image light is different than the time that just using focused light and light is smoothly distributed all over the image. The image obtained from focused light and Kohler illumination is depicted in Fig. 21 and Fig. 22.

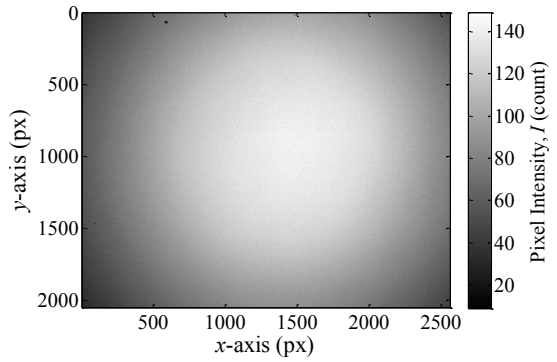

Fig. 21: An image of the light field using focused light

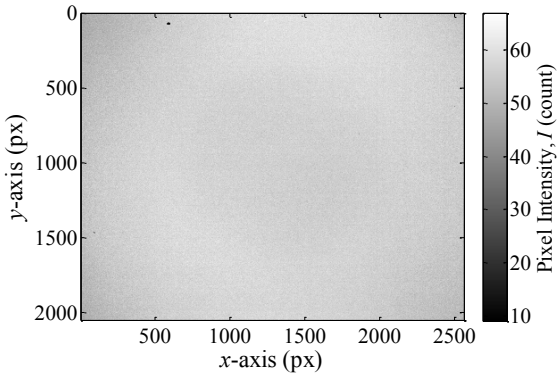

Fig. 22: An image of the field using light from Kohler illumination

4.12 Tracer Particles

An important feature of the seeding particle is that they follow the flow faithfully without exerting any force on the flow. In this case, the particle density ρ_p should be equal to fluid density ρ_f. The seeding particles used have technical diameter of 18 μm, fused borosilicate glass (ASTM C169) shape: hollow non-porous microspheres (Spherical 110P8; Vendor: Potters Industries Inc.) with alkalinity: Max 0.5 meq/g (ASTM D3100) and Max. 0.5 weight % (10 min. @ 250°F). The density of the sphere is 1.1 gcm^3. The size distribution data provided by the manufacturer lists the mean size distribution to be 10 μm. A technique to effectively remove the larger spheres was developed relying upon the assumption that the bigger particles will be heavier (under similar density and hollowness of the lot) and hence settle in water faster than the others. Conducting PIV has a preference to smaller particles in the size range 500 to 1500 nm [16]. These particles were spatially resolved over 3 to 4 pixels [15] and follow the flow perfectly. Properties of the particle sets used in the experiment (at 250 °F) are available in Table 4.

Table 4: Properties of particle sets used in experiment (at 250 °F)

Particle Set	Description	Mean Diameter (μm)	CV	Density (g/cc)	Maximum Working Pressure, (psi)	Bulk Density, (g/cc)
110P8	Hollow Microspheres (Potters 110P8)	5	10%	1.1± 0.05	10,000	0.49
110P8	Hollow Microspheres (Potters 110P8)	10	50%	1.1± 0.05	10,000	0.49
110P8	Hollow Microspheres (Potters 110P8)	21	90%	1.1± 0.05	10,000	0.49
110P8	Hollow Microspheres (Potters 110P8)	25	97%	1.1± 0.05	10,000	0.49

4.13 Size Distribution of Particles

Cumulative distribution function (cdf) describes a variable with a known probability distribution which has a value less or equal to *x*.

$$p(x) = \int_{-\infty}^{x} p(t)dt \tag{4.1}$$

Using HELOS size analyzer device, gives the cumulative distribution function of particles for two different times, one before settlement of particles and the other after the settlement. Results obtained from this device are shown in Fig. 23. The cumulative distribution function for smaller particle size has larger value, and the density distribution shows its peak at a higher value and smaller particle size. This two plots show that smaller sized particles have the most distribution because the larger sized particles were settled and not existed within the sample.

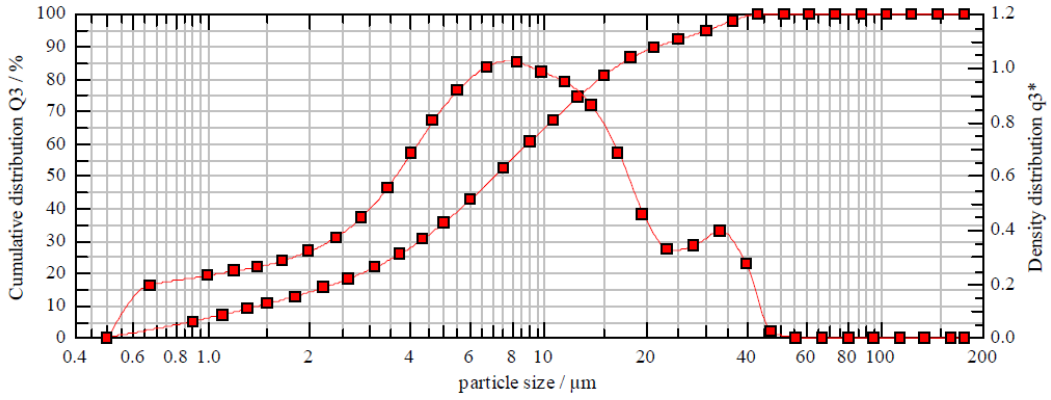

a)

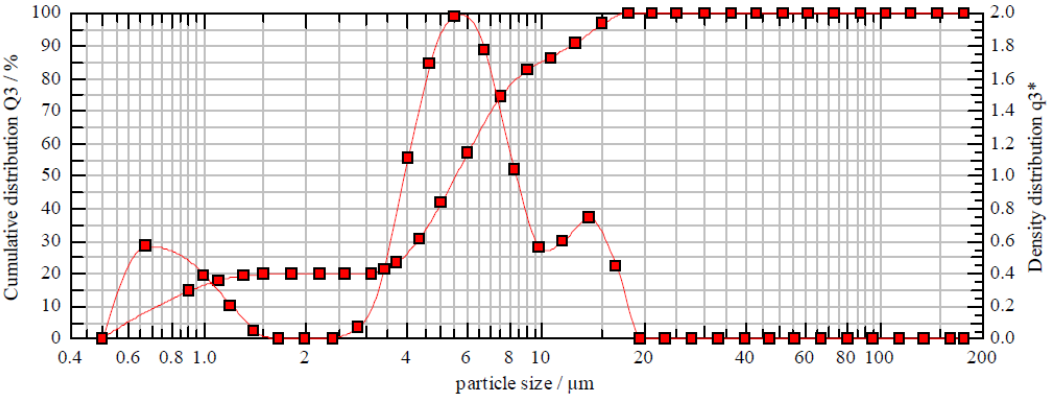

b)

Fig. 23 Cumulative distribution function of particle measured with HELOS (H1019) a) before and b) after settlement of particles in the fluid.

The distribution function is the derivative of the probability density function, so when there is a variation in each part of the plot of cumulative density function the distribution function gets a value because the derivative will not be zero. Density distributions of particles with the data obtained from HELOS (H1019) are plotted in Fig. 24. These plots related to before and after settlements of particles and are the same as the plots which obtained from HELOS (H1019) for density distribution.

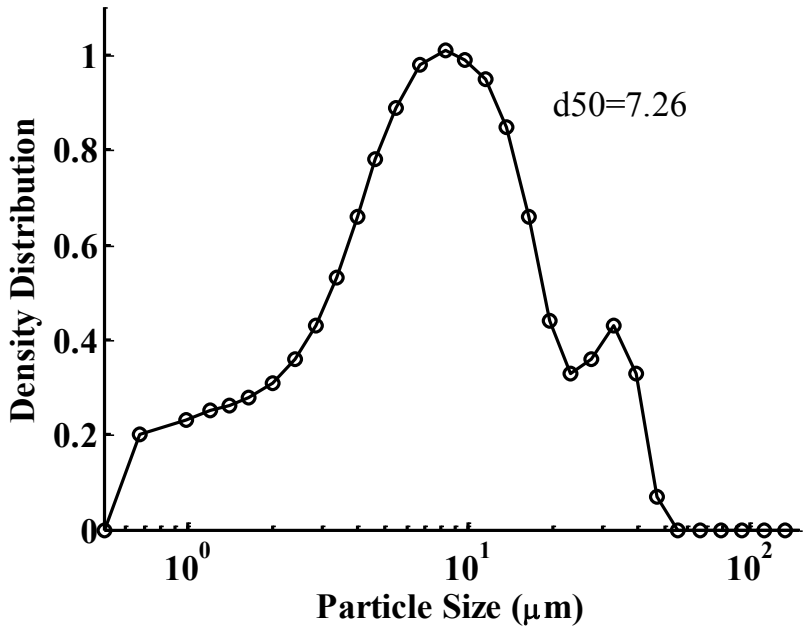

a)

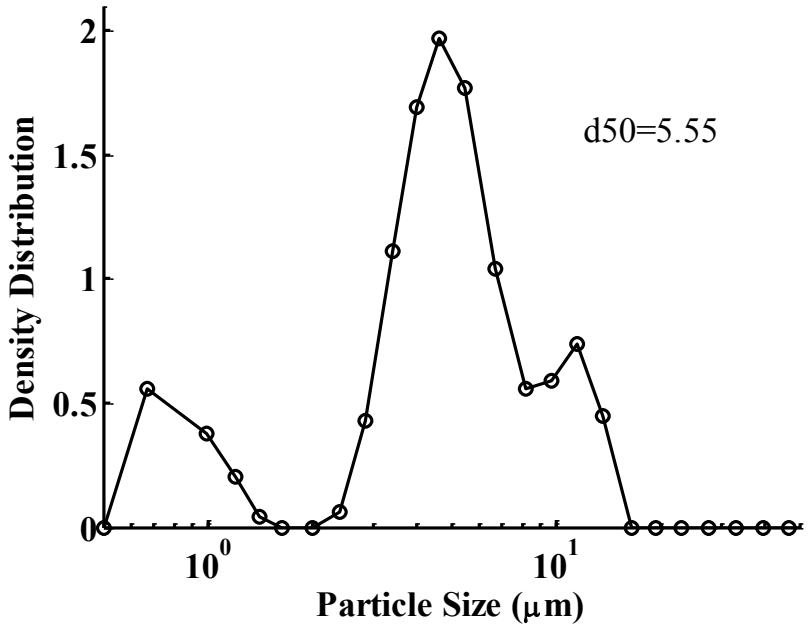

b)

Fig. 24: Density distribution of particle a) before and b) after settlement of particles in the fluid.

CHAPTER 5: **INSTANTANEOUS RESULTS AND DISCUSSION**

Flow which is investigated in the current experiments is fully developed and laminar. Laminar theory is well developed for internal and external flows [30]. Internal flow is the flow with surrounding boundary and increase effect of viscosity on the entire flow. The laminar and fully developed flow is assumed to have parabolic velocity profile as discussed in Chapter 2 and axial velocity no longer changes along the channel and provides a constant velocity profile.

An investigation of the velocity profiles determined from the experimental data is undertaken in this chapter and Chapter 6. The flow rate in a microchannel is much smaller than the flow rate in the turbulent regime so, the flow in microchannel is laminar and parabolic velocity profile is predicted to be observed. The experiments were undertaken and images were captured when the flow was fully developed, so the velocity profile was assumed to be constant throughout the channel and in duration of time.

Individual images of the flow with particles in the channel were considered, and distinct processing schemes were taken in to account to discuss the variation in the results through processing scheme. Velocity fields obtained from three different images are presented in Fig. 25, Fig. 26 and Fig. 27. The sizes of the vectors are different in these three images and these show the changes in velocity

values in the span of time when fluid flows in the channel. The even velocity vectors for one image observed in figures depict the steadiness of the flow in different locations of the channel.

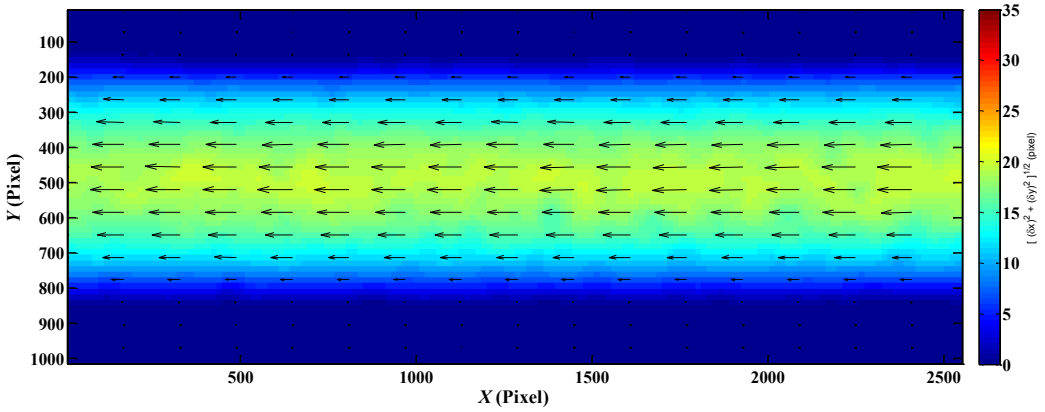

Fig. 25: Velocity along channel for elliptic interrogation window with aspect ratio of 2 for image number 150

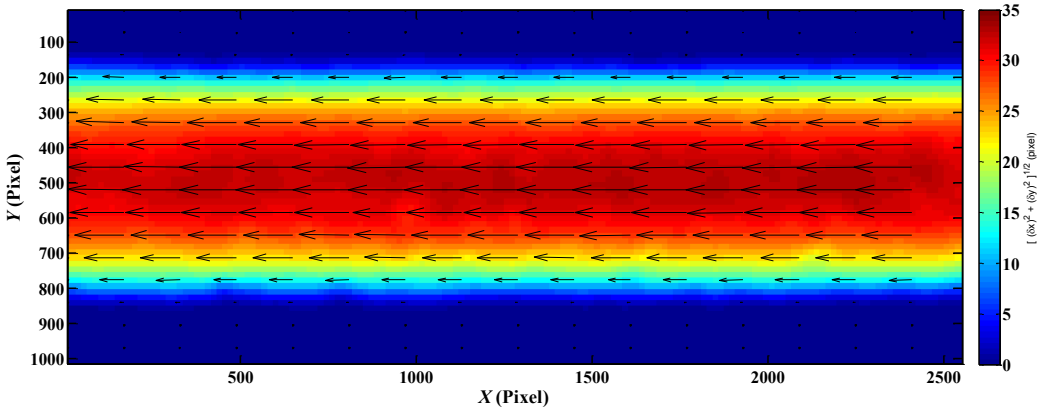

Fig. 26: Velocity along channel for elliptic interrogation window with aspect ratio of 2 for image number 175

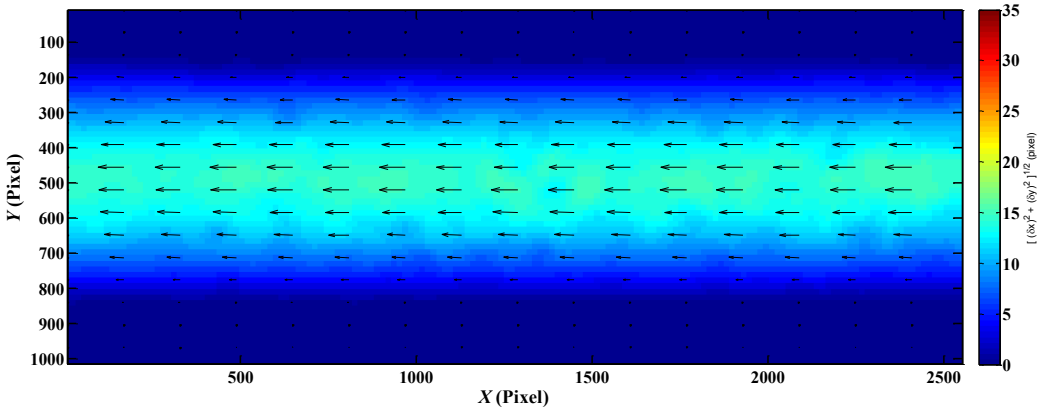

Fig. 27: Velocity along the channel for elliptic interrogation window with aspect ratio of 2 for image number 200

Velocity profiles across the channel for image number 150, 175 and 200 were calculated and shown in Fig. 28. From what is depicted in the figure an increase in the maximum velocity from image number 150 to image number 175 and again a decrease in the velocity from image number 175 to image number 200 is observable. These jumps in the velocity are because of spontaneous jerking motion, which was caused by the sliding of the syringe piston into its cylinder and called slip stick. This slip-stick is mostly observable in plastic syringes as the surface between the syringe piston and cylinder has friction and the load which overcomes the static friction can cause a jump in the flow as the dynamic friction available for motion is less than static friction.

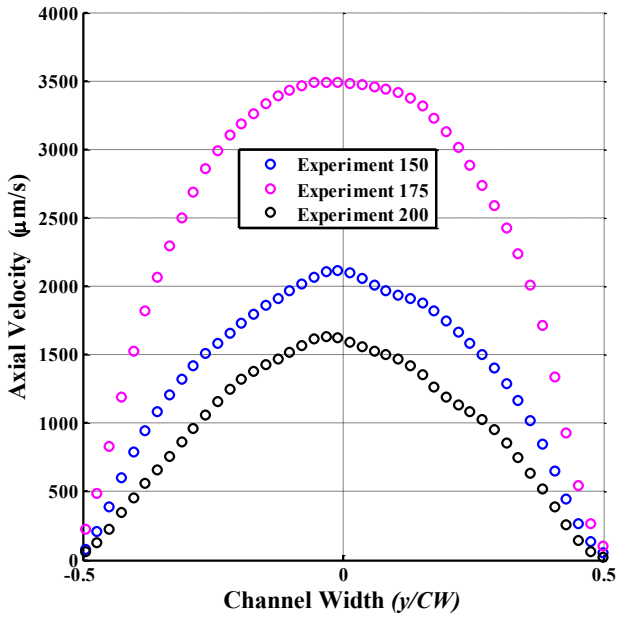

Fig. 28: Average of velocities along the channel for images number 150, 175 and 200 for the flow with 0.01 ml/min flow rate.

5.1 Instantaneous Velocities

In this part, two sets of experimental data, which were processed with DaVis 8.0.7 with different flow rates, are presented. The centre line velocity along the channel was calculated from the instantaneous velocities. Centre line velocities calculated from each instantaneous vector field for each image were plotted and shown in Fig. 29 and Fig. 30. It is observable that the flow along the channel has fluctuations and is not what could be expected of a laminar flow in a microchannel. Laminar flow should have a constant centre line velocity in different locations. These fluctuations are mainly because of using a syringe pump which cannot produce steady flow field.

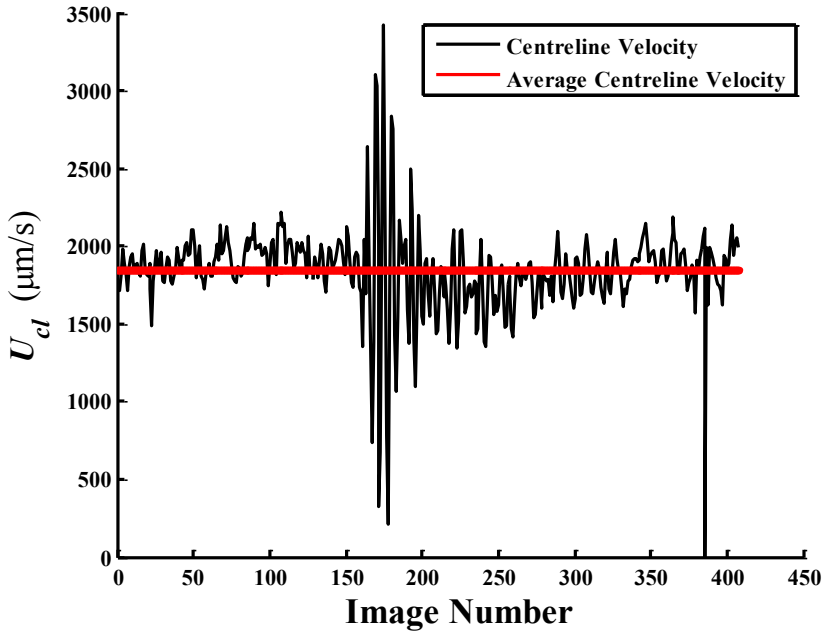

Fig. 29: Centre line velocities of 400 images and average of all centre line velocities for the flow with 0.01 ml/min flow rate.

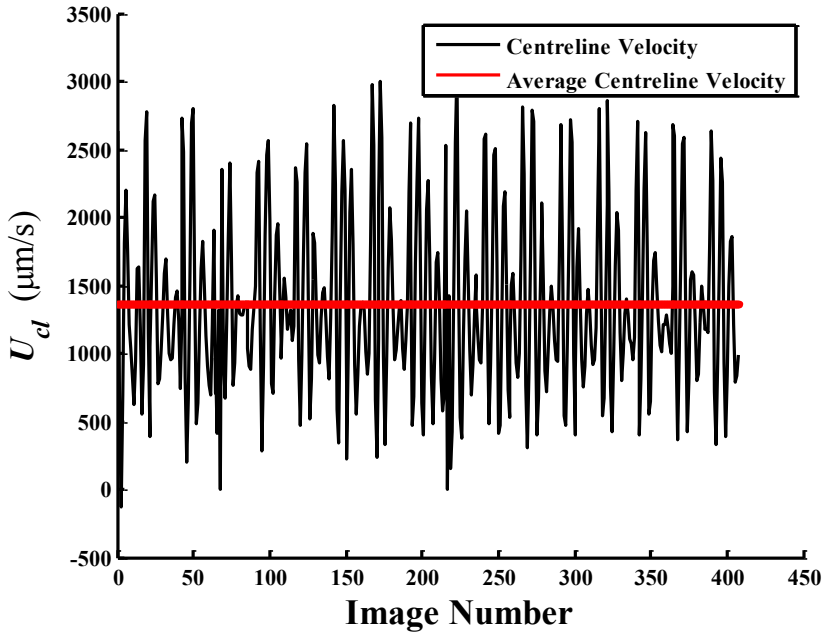

Fig. 30: Centre line velocities of 400 images and average of all centre line velocities for the flow with 0.008 ml/min flow rate.

These differences between the velocities of the centreline from one image to the other image have required the use of different methods in averaging. In these velocities, the averaging in time step is not just like a normal averaging of the actual velocity values. First, velocities in different y locations across the channel are normalized by their centre line velocity, and the normalized parabolic velocity profile is obtained for each x location along the channel and then all normalized velocity profiles of 400 images averaged and give one specific velocity profile as is depicted in Fig. 31. Normalized velocities have the parabolic shape so their average is also in parabolic shape.

In this section the velocities along the channel from experiment which were obtained from captured images by the camera and processed with DaVis 8.0.7 are shown, and the results are described as they were processed with different schemes.

The streamwise velocity profiles of one instantaneous image for various multi pass interrogation windows of 64 × 64 to 32 × 32, 128 × 128 to 64 × 64, and 256 × 256 to 128 × 128 with the elliptic shape and aspect ratio of 2 are presented in Fig. 31 together with the corresponding fully developed laminar analytical velocity profile for a pipe. The deviation from the laminar profile becomes apparent when the experimental results reach near the channel wall locations, and the interrogation windows become larger. Looking at velocity profile in Fig. 31.c) indicate that with bigger interrogation window sizes of 256 × 256 to 128 × 128 there are lack of velocity vectors near the wall which cause an error in calculating velocity profile.

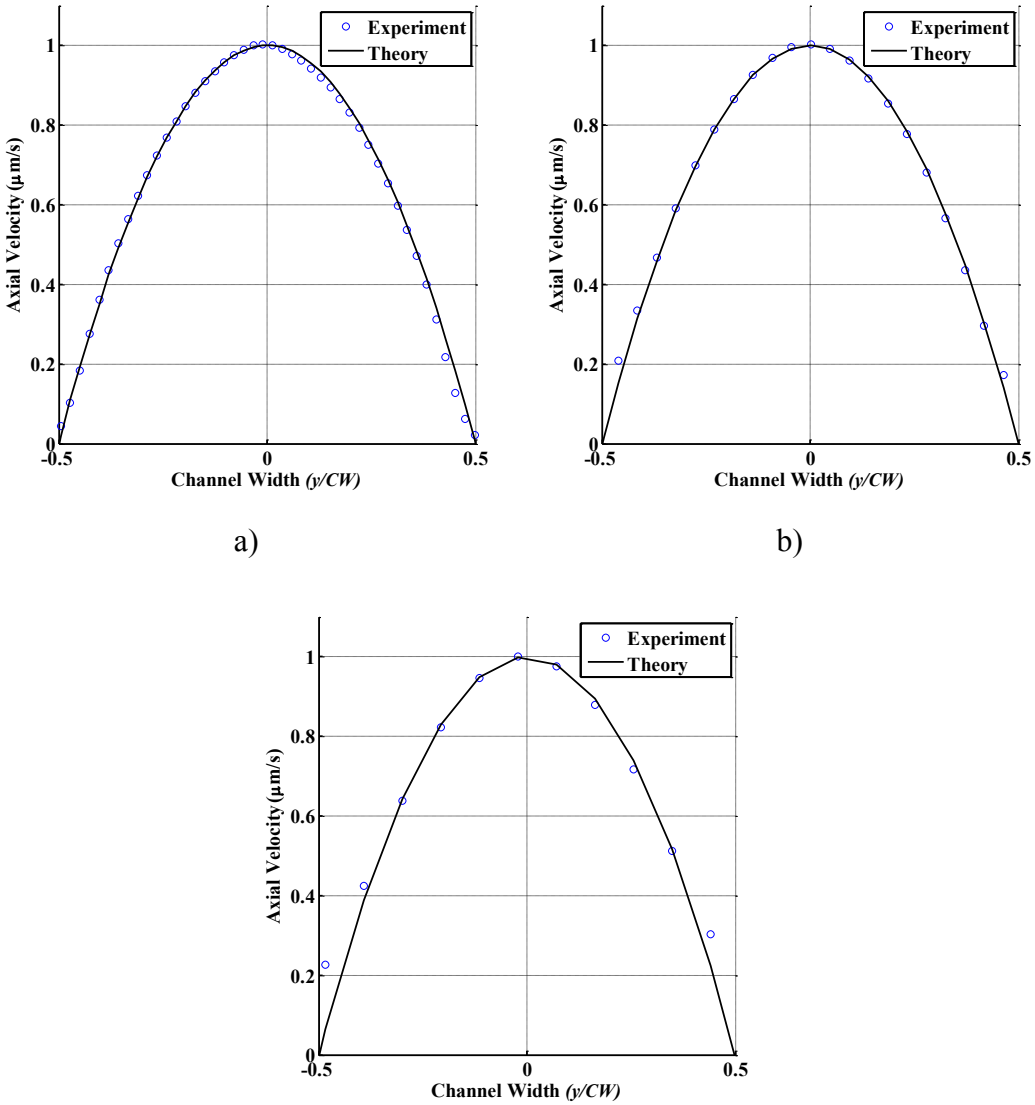

a) b)

c)

Fig. 31: Velocity profile for elliptic shape interrogation window with aspect ratio of 2 and multi pass (decreasing interrogation window sizes) and 50% overlap, a) 64 × 64 to 32 × 32, b) 128 × 128 to 64 × 64, c) 256 × 256 to 128 × 128 .

5.2 Interrogation Windows Shape and Size

The PIV analysis using the commercial software (DaVis 8, LaVision GmbH) has commonly used a cross correlation method over two consecutive images to determine the average displacement of particle in a window. Different interrogation window sizes of 256, 128, and 64 pixels have been used in the analysis. These are shown in relations to the channel width and the shape of the expected velocity profile in Fig. 32. The interrogation windows in the middle of the channel and those which capture the near wall region are observable in this figure. When the interrogation windows reach near wall locations, they interfere with boundary and capture beyond boundary regions. This will generate images with some parts seeded and other parts without seeding particle. These images produce flattened correlation peaks that are not distinct. For larger interrogation windows, more data is collected outside of the microchannel affecting the correlation. With this demonstration, it can be inferred that the sizes of interrogation windows will influence the processing scheme and is a point that will be investigated using experimental results and shown further in this chapter.

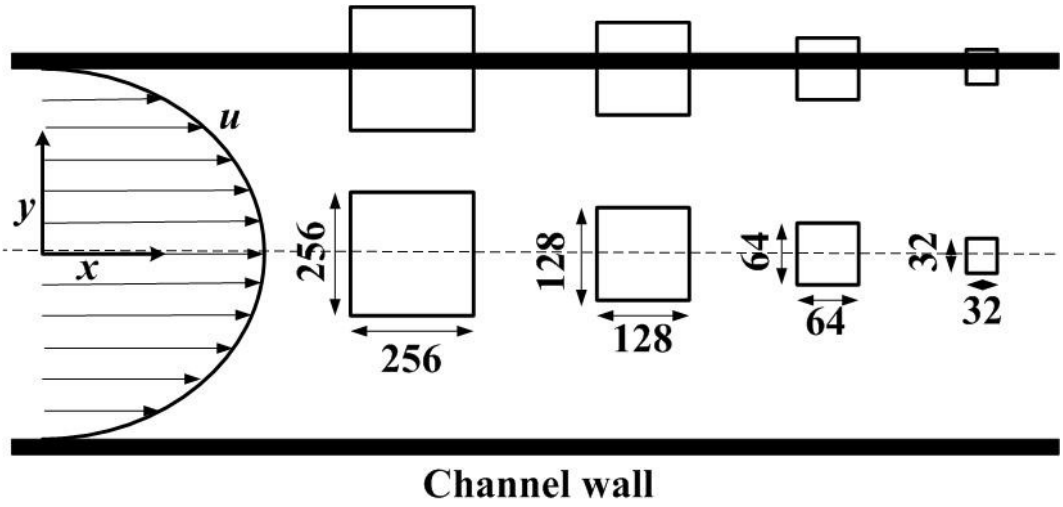

Fig. 32: Square interrogation windows showing different sizes in the microchannel

Two types of single pass and multi pass are available in the software. Single pass is when the velocity vector calculation is undertaken in one pass, Interrogation window sizes and overlaps are constant for the evaluation of particles displacements, and post processing are not applicable during vector calculation

Multi pass is when calculating of displacement vector is investigated by arbitrary number of calculations on the same image with a constant or decreasing interrogation window sizes. For the multi pass with decreasing window sizes the evaluation starts in the first pass with the initial window size and calculate a reference vector. In the next pass the interrogation window size is half the size of the previous pass, and the vector calculated in the previous window used as the best choice window shifting. Window shifting in the multi pass is more accurate and reliable.

In addition to changing of the interrogation window size, it is possible to change the shape of the interrogation window and investigate its influence on the determination of the velocity profile. Two other interrogation windows in the shape of an ellipse with different aspect ratios of 4 and 2 are shown in the Fig. 33. As it is shown in the figure, with the elliptic interrogation window with the aspect ratio of 4 a bigger range in the *x* direction is covered. For the aspect ratio of 2, still a larger domain in the *x* direction compared to the same size square interrogation window is covered. So the hypothesis is that for the elliptic interrogation windows, the error in the calculation of the velocity profile near the wall boundary will be smaller. This will be investigated using the experimental results in chapter 6.

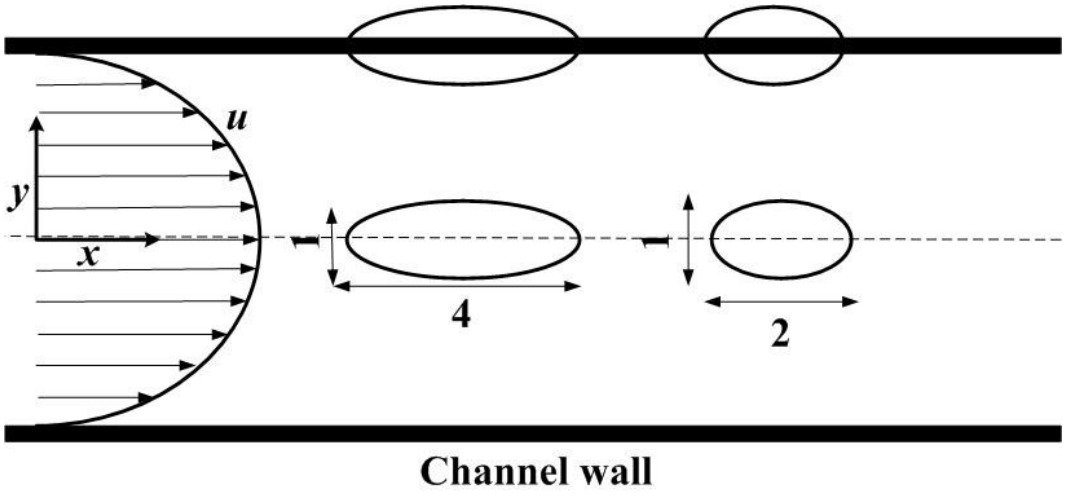

Fig. 33: Elliptical interrogation windows with aspect ratio 4 and 2 in microchannel

5.3 Effect of the Interrogation Window Size on the Cross Correlation Function

Interrogation windows and the cross correlation peaks associated with each interrogation window are shown in Fig. 34, Fig. 35, and Fig. 36. Sizes of interrogation windows are changed in these three figures. Interrogation window with size of 64 pixels is shown in Fig. 34.Because the cross correlation function is based on intensity, while the interrogation window is placed in the middle of the channel the particles inside the window have enough intensity and cross correlation peak image show distinct peaks when the interrogation windows are within the channel, and when the interrogation windows pass through the boundary, a sharp and detectable cross correlation peak is not distinguishable because of less intensity of the particles at boundary region and the wall intensity dominate the correlation function and biased the peak towards wall region. As shown in Fig. 34 d) the cross correlation peaks were changed when the interrogation windows reach wall boundaries, and they are not as sharp as the correlation peaks associated with the interrogation windows in the middle of the channel. Cross correlation functions related to the interrogation windows assigned to the boundary have not a unique correlation peak and depict the difficulty of the velocity calculations near the channel walls. Interrogation windows near the boundary will lack of the particles in some parts as those parts related to outside boundary regions. Images of the interrogation windows interfering with boundary consist of flow field with seeding particle, boundary wall and part with no seeding particles, so the cross correlation peaks cannot be obtained for the whole

interrogation window domain. Fig. 35: and Fig. 36 are related to 128 and 256 pixels interrogation windows, and again the correlation peaks are distinct in the middle of the channel for 128 and 256 interrogation windows sizes and vague correlation peaks are observed for those interfering with boundary.

Different sizes of interrogation windows in calculating cross correlation function has influenced on the cross correlation peaks. Looking at Fig. 34, Fig. 35, and Fig. 36 shows that with smaller sizes of the interrogation windows. More data available in the interrogation windows and probability of finding better correlation peak is high.

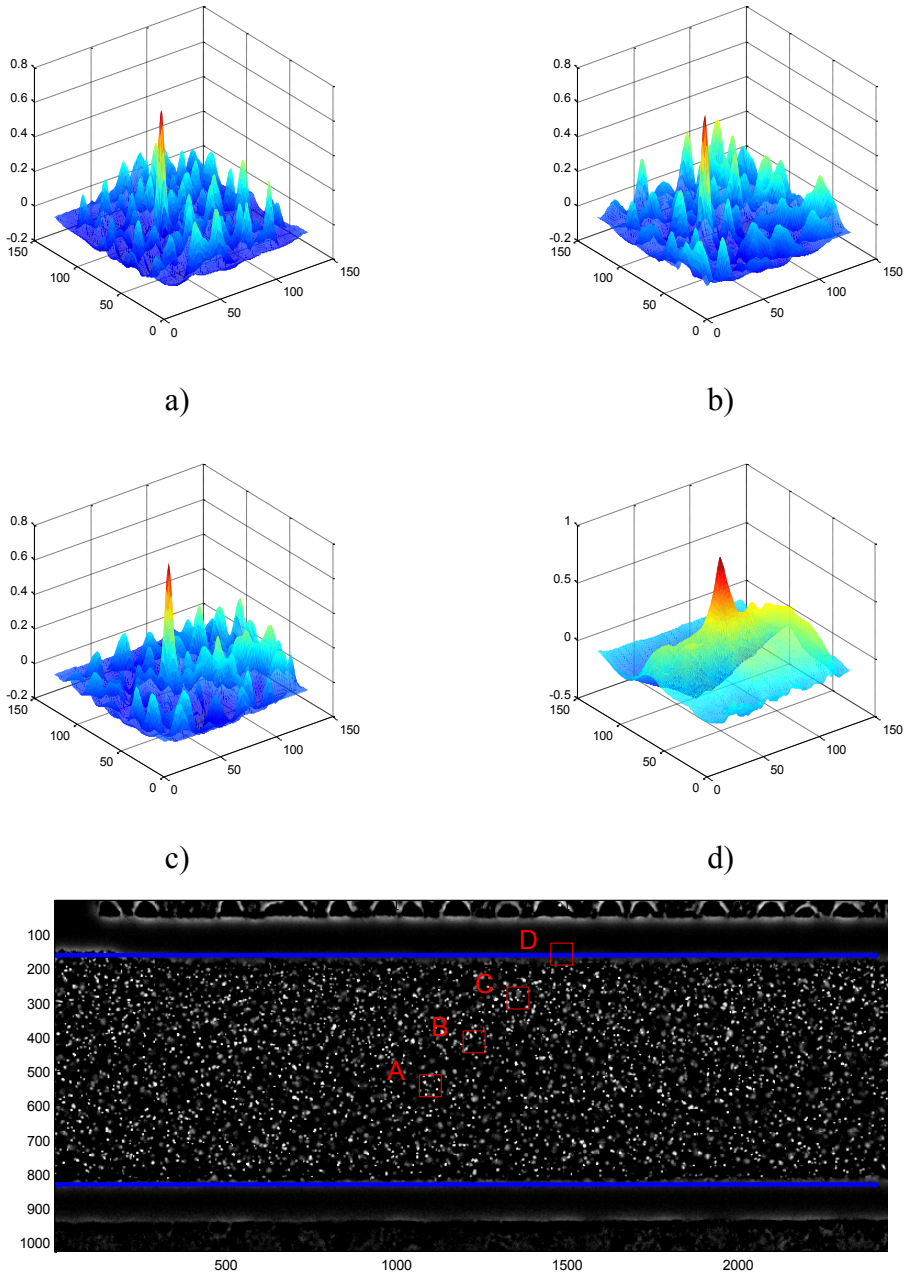

Fig. 34: Microchannel with particles and 64 × 64 pixels interrogation windows, a), b), c), d) show cross correlation function associated with the interrogation windows, and e) shows the location of interrogation windows.

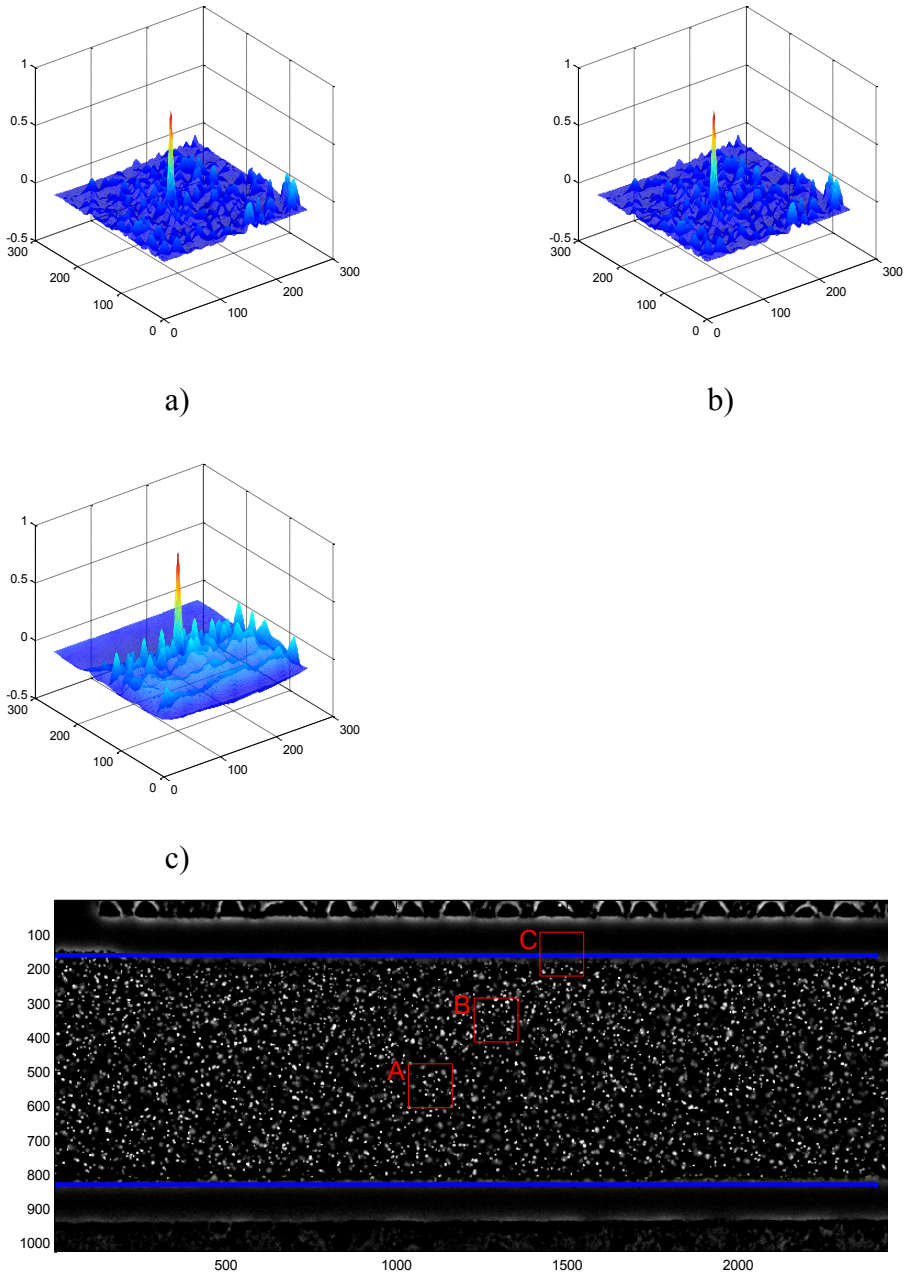

Fig. 35: Microchannel with particles and 128 × 128 pixels interrogation windows, a), b), c) show cross correlation function associated with the interrogation windows, and d) shows the location of interrogation windows.

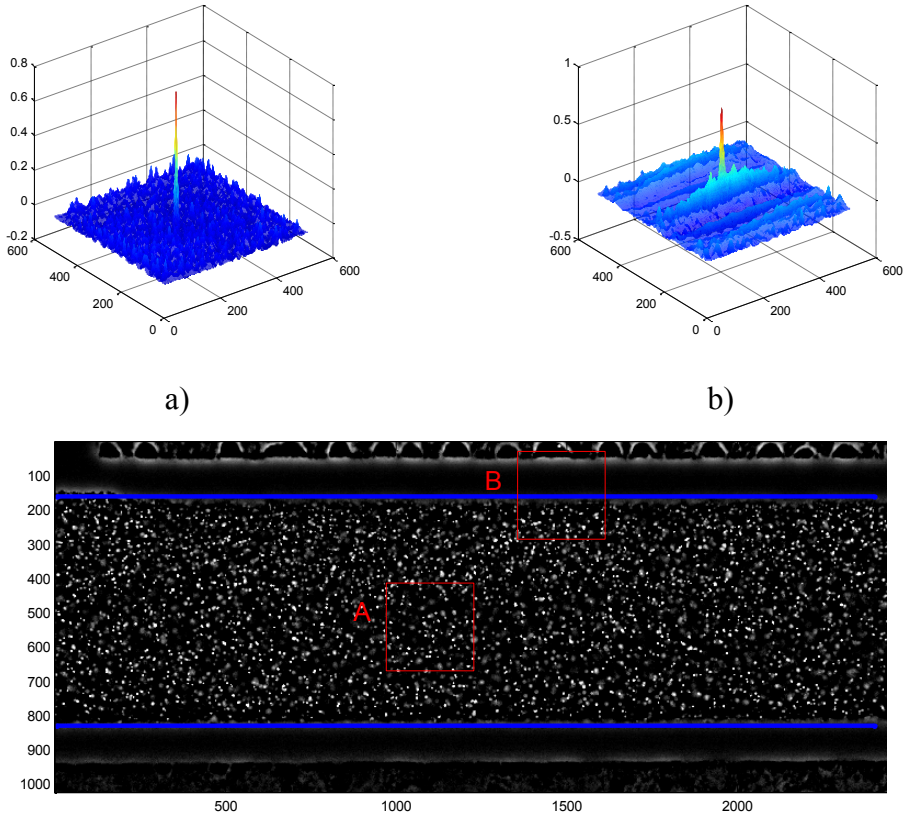

Fig. 36: Microchannel with particles and 256 × 256 pixels interrogation windows, a), b) show cross correlation function associated with the interrogation windows, and c) shows the location of interrogation windows.

5.4 Conclusion

In this chapter, the instantaneous velocity vectors along the channel associated to one image is investigated and then velocity profiles for three images are obtained from velocity vectors, which depict a parabolic velocity profile as it was assumed. Another result deals with the velocity of the centre line, and cross

correlation peaks related to different interrogation window sizes are plotted and shown at the end of the chapter. The clear sudden jump in the velocity profile from image number 150 to 200 shows a slip stick phenomena associated with the syringe. The changes in the interrogation window sizes depict the changes in the cross correlation peaks, as with the smaller size of the interrogation windows the cross correlation peaks are more distinct and observable which lead to calculate velocity profile in better correspondence with theory.

CHAPTER 6: **RESULTS AND DISCUSSION**

6.1 Theories and Computational Approach

In this chapter the results and discussions associated with the mean velocity profiles which are averaged between the velocities obtained from all the vector fields in the images along the channel are presented. Results are shown in Fig. 37 to Fig. 42. Another part of the chapter related to the results from the differences between experimental velocity profiles and the laminar profiles, and these results are shown in Fig. 43 to Fig. 48.

6.2 Velocity Profile Obtained from Experiment and Theory

Experiments were undertaken for two different flow rates and processed for different interrogation shapes and sizes. Fig. 37 shows the velocity profile obtained from experiment and analyzed with three interrogation window shapes of square, elliptic with aspect ratio of 2 and 4 for two different flow rates of 0.008 ml/min and 0.01 ml/min.

Experimental results for the higher flow rate of 0.01 ml/min show a better comparison with the theory profile obtained from the analytical solution of the flow in a pipe. Looking at the velocity on the centre line for the flow rate of 0.01 ml/min for 400 images which is shown in Fig. 29 of chapter 5 indicates that the velocity profile for a flow rate of 0.01 ml/min is more uniform over the span

of time of the experiment. Another observable result from Fig. 37 is that the velocity profiles of different interrogation window shapes, analyzed with the same window size of 256×256 decreasing to 128×128, have not much difference with theoretical velocity profile in the centre line region of the channel. Differences are apparent in near the wall regions. As is discussed in Chapter 5 for the interrogation windows, with elliptical interrogation window of aspect ratio of 4, more seeding particles are confined in the window which leads to a better cross correlation peaks, so the velocity profile related to this interrogation window approaches the theoretical velocity profile with less difference comparing to using two other interrogation windows. After the interrogation window with shape of elliptic and aspect ratio of 4, velocity profile obtained from processing scheme using elliptic with aspect ratio of 2 interrogation window has better corresponding with the theoretical profile. Velocity profile plotted for the square interrogation window in the processing scheme shows the largest difference from the theoretical velocity profile near the wall.

Data processed with the different interrogation shapes and same window size of 128 × 128 decreasing to 64 × 64 and window size of 64 × 64 decreasing to 32 × 32 are shown in Fig. 38 and Fig. 39. The same conclusion drawn for Fig. 37 is applicable for the results shown in these two figures. Also with the conclusions that have been made, these three figures show that size of the interrogation windows have an influence on the velocity profile near the wall regions. When the interrogation widow size is smaller, the experimental velocity profile is closer to the theoretical velocity profile. This is true also when approaching the boundary

of the domain where this can be seen as a good correspondence of the experimental and theoretical velocity profile in Fig. 39.

The next sets of plots from Fig. 40 to Fig. 42 are related to plotting the data which are analyzed with the processing scheme of one interrogation window shape and different interrogation window sizes. These plots verified the same conclusions that the velocity profile obtained from a processing scheme of using small interrogation window sizes as 64 × 64 decreasing to 32 × 32 with the elliptic interrogation window of aspect ratio 4 has the least difference with theory and match theoretical profile near the wall region. With small interrogation window sizes of 64 × 64 decreasing to 32 × 32, other interrogation window shapes of elliptic with aspect ratio of 2 and square processed data also show experimental velocity profile with less difference from theory.

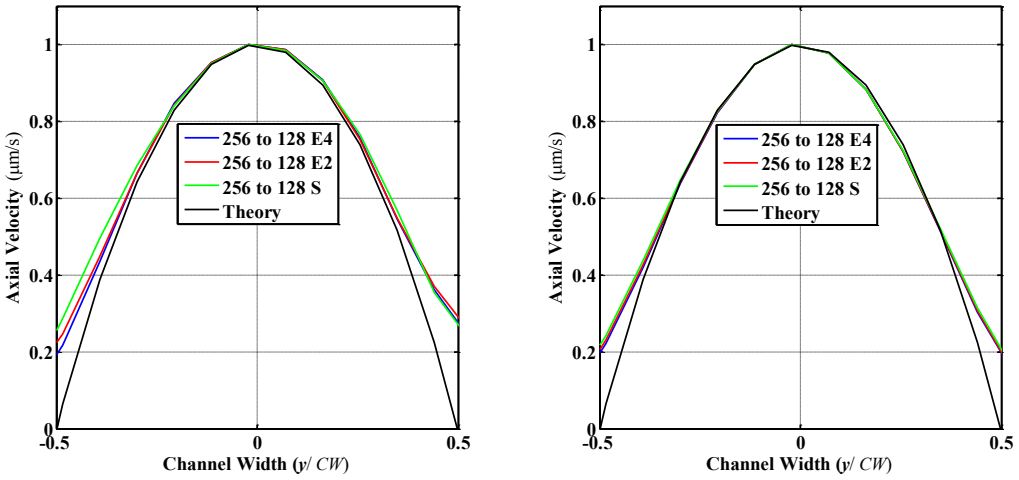

a) b)

Fig. 37: a) Velocity profile for three different interrogation windows of square, elliptic aspect ratio of 4 and 2 with decreasing of interrogation window size from 256 to 128 for flow rate of 0.008 ml/min, b) 0.01 ml/min.

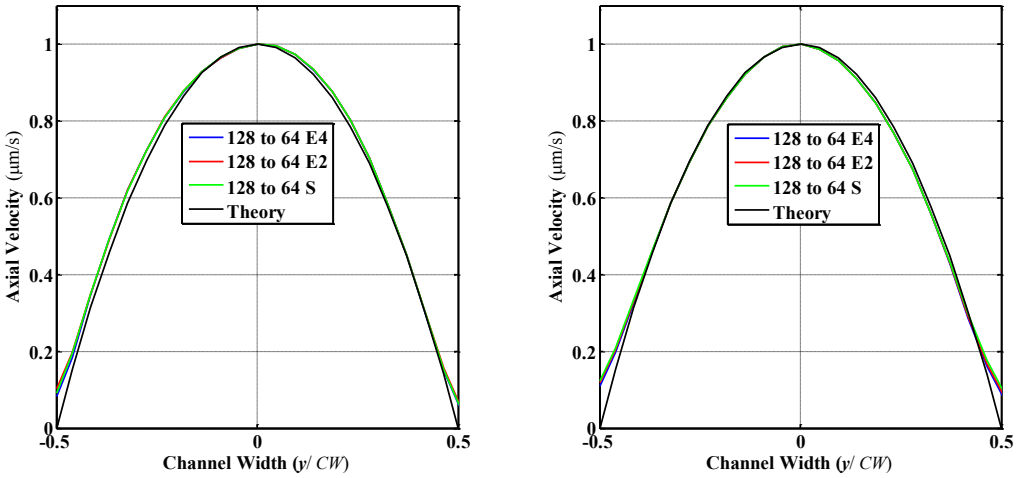

a) b)

Fig. 38: a) Velocity profile for three different interrogation windows of square, elliptic aspect ratio of 4 and 2 with decreasing of interrogation window size from 128 to 64 for flow rate of 0.008 ml/min, b) 0.01 ml/min.

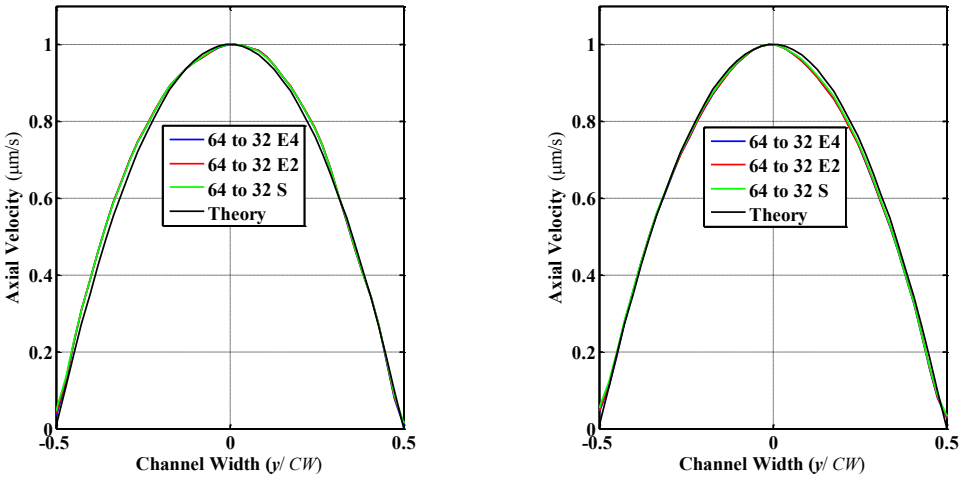

a) b)

Fig. 39: a) Velocity profile for three different interrogation windows of square, elliptic aspect ratio of 4 and 2 with decreasing of interrogation window size from 64 to 32 for flow rate of 0.008 ml/min, b) 0.01 ml/min.

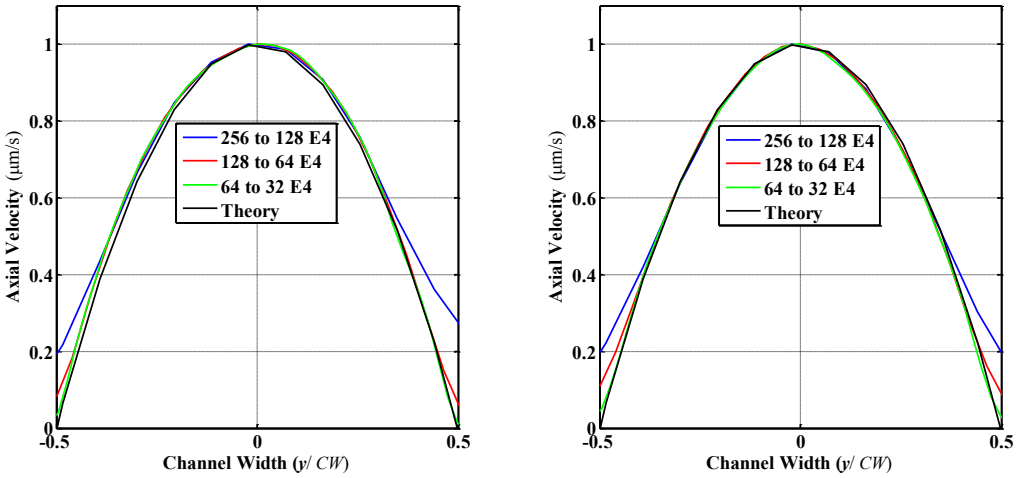

a) b)

Fig. 40: a) Velocity profile for three different pass of decreasing of interrogation window size from 256 to 128, 128 to 64 and 64 to 32 for elliptic interrogation window shape with aspect ratio of 4 and flow rate of 0.008 ml/min, b) 0.01 ml/min.

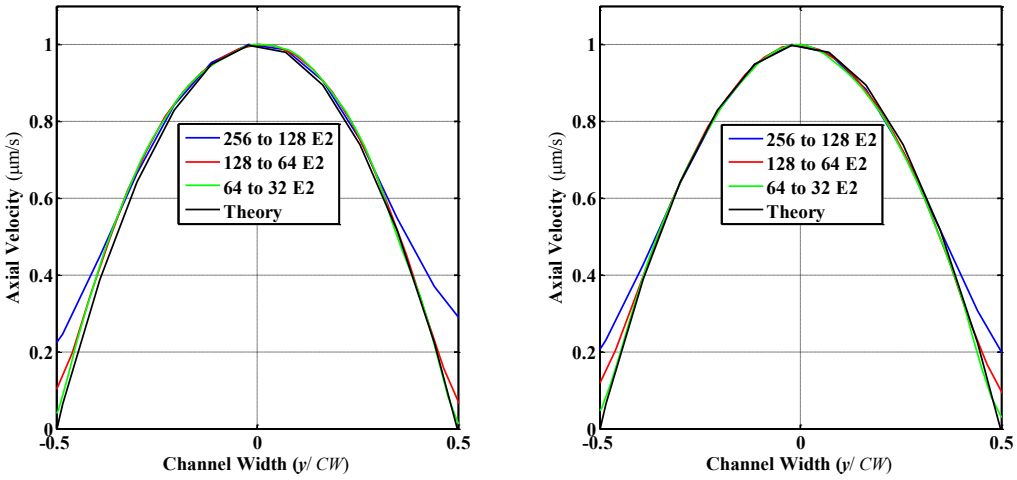

a) b)

Fig. 41: a) Velocity profile for three different pass of decreasing of interrogation window size from 256 to 128, 128 to 64 and 64 to 32 for elliptic interrogation window shape with aspect ratio of 2 and flow rate of 0.008 ml/min, b) 0.01 ml/min.

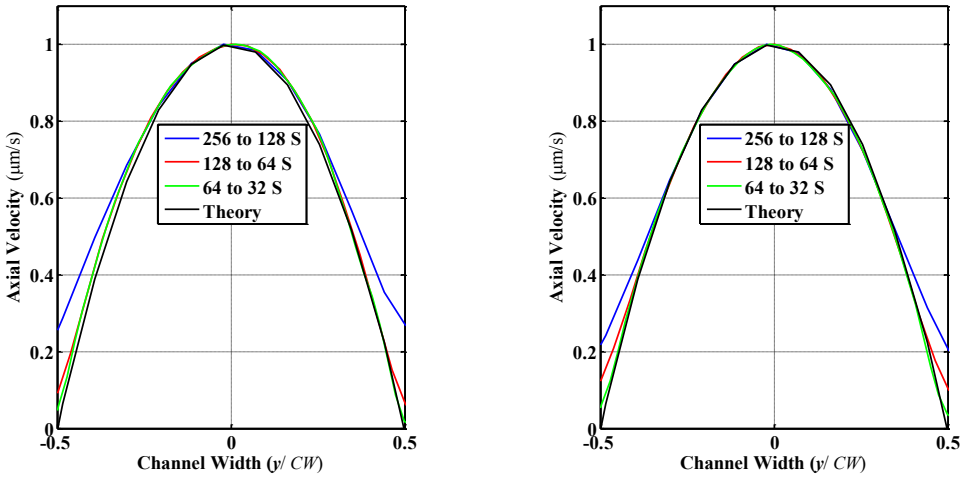

a) b)

Fig. 42: a) Velocity profile for three different pass of decreasing of interrogation window size from 256 to 128, 128 to 64 and 64 to 32 for square interrogation window shape and flow rate of 0.008 ml/min, b) 0.01 ml/min.

6.3 The Difference between Theory and Experiment

In this section the difference between the theoretical and experimentally determined velocity profiles are calculated. As it is observed in all figures from Fig. 43 to Fig. 48 the difference between theoretical and experimental velocity profiles are larger near the walls of the microchannel. These differences approach close to zero at centre of the microchannel. This is where there is only a small velocity gradient across the interrogation window. The problem with near wall region is that the interrogation windows near the wall cannot capture enough seeding particles and there are larger gradients in the local velocity. These produce errors in calculating cross correlation function and do not generate distinct peaks used to determine the velocity vectors. As it is observed in Fig. 45 when interrogation window sizes are decreased, there are more data collected / particle images that have similar velocities leading to a calculated velocity vector close to the theoretical velocity profiles.

The plots in these figures indicate the influence of size and shape of the interrogation windows on calculated velocity profiles. The results obtained from data processed with elliptical interrogation window of aspect ratio 4 and size of 64 × 64 decreasing to 32 × 32 matches the theory results for velocity profile with fewer errors compare to the other processing scheme. Errors in calculating of velocity profile near the wall regions become larger when the sizes of interrogation windows increased, and shapes of interrogation windows change from ellipse to square.

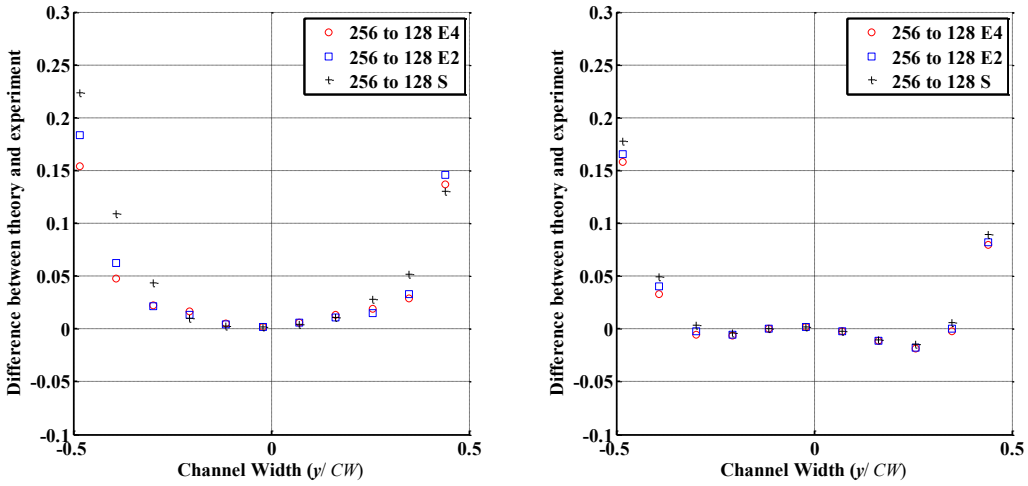

a) b)

Fig. 43: a) Difference between theoretical velocity profile and average experimental velocity profile calculated from instantaneous velocities for square, elliptic aspect ratio of 4 and 2 interrogation window with decreasing size from 256 to 128 for flow rate of 0.008 ml/min, b) 0.01 ml/min.

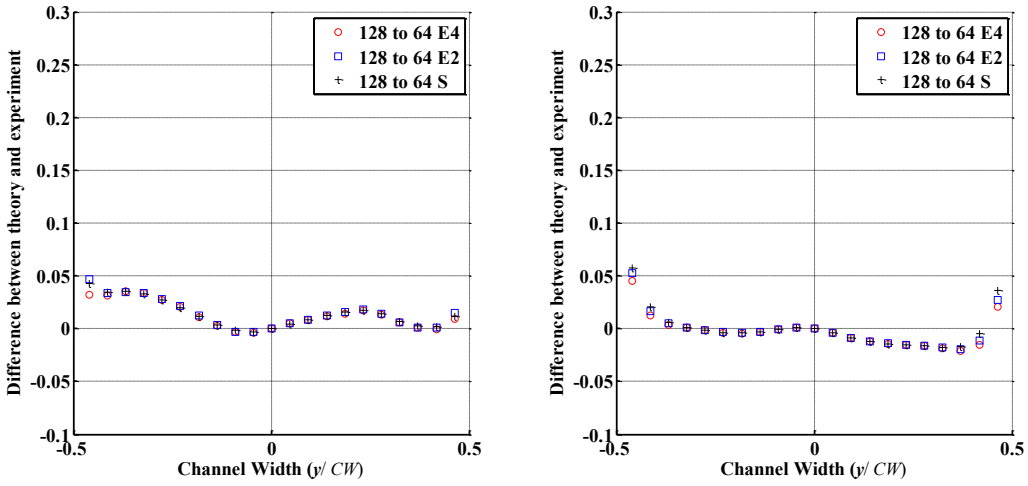

a) b)

Fig. 44: a) Difference between theoretical velocity profile and average experimental velocity profile calculated from instantaneous velocities for square, elliptic aspect ratio of 4 and 2 interrogation window with decreasing size from 128 to 64 for flow rate of 0.008 ml/min, b) 0.01 ml/min.

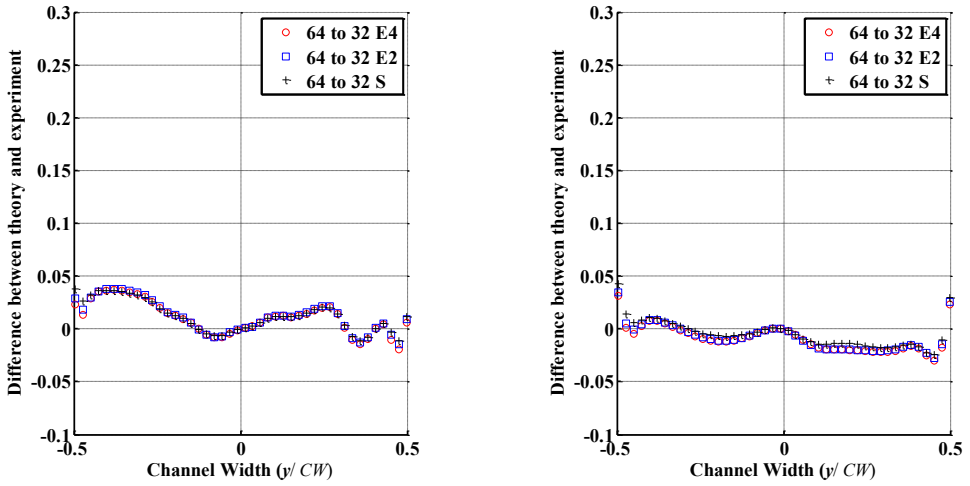

a) b)

Fig. 45: a) Difference between theoretical velocity profile and average experimental velocity profile calculated from instantaneous velocities for square, elliptic aspect ratio of 4 and 2 interrogation window with decreasing size from 64 to 32 for flow rate of 0.008 ml/min, b) 0.01 ml/min.

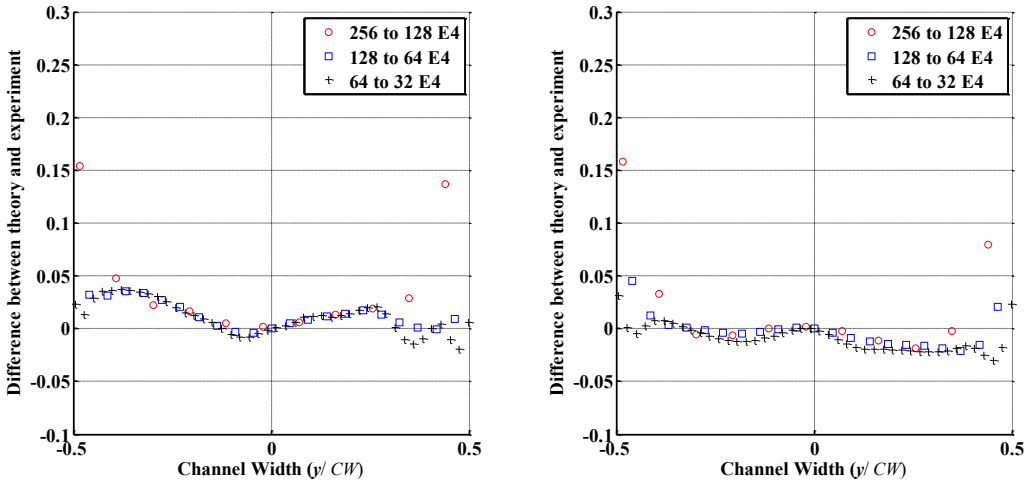

a) b)

Fig. 46: a) Difference between theoretical velocity profile and average experimental velocity profile calculated from instantaneous velocities for three different pass of decreasing elliptic aspect ratio of 4 interrogation window size from 256 to 128, 128 to 64 and 64 and flow rate of 0.008 ml/min, b) 0.01 ml/min.

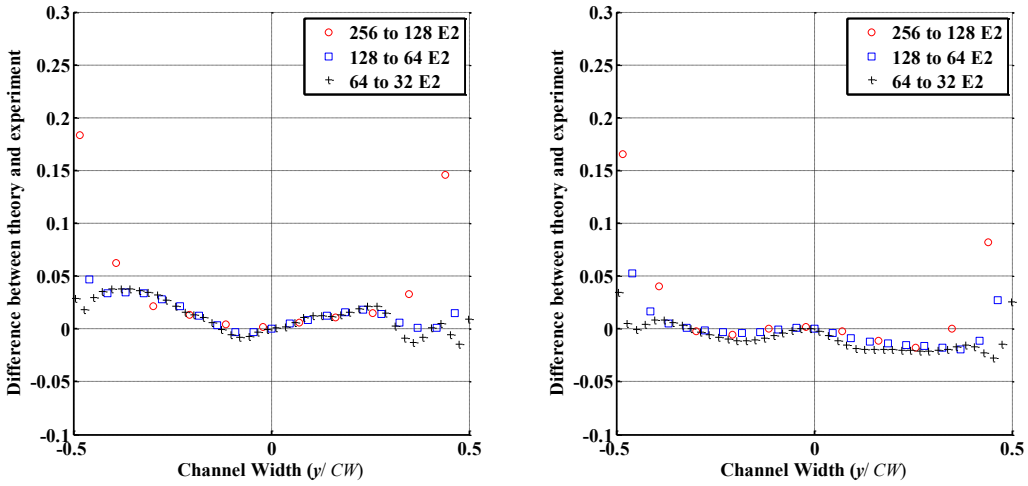

a) b)

Fig. 47: a) Difference between theoretical velocity profile and average experimental velocity profile calculated from instantaneous velocities for three different pass of decreasing elliptic aspect ratio of 2 interrogation window size from 256 to 128, 128 to 64 and 64 and flow rate of 0.008 ml/min, b) 0.01 ml/min.

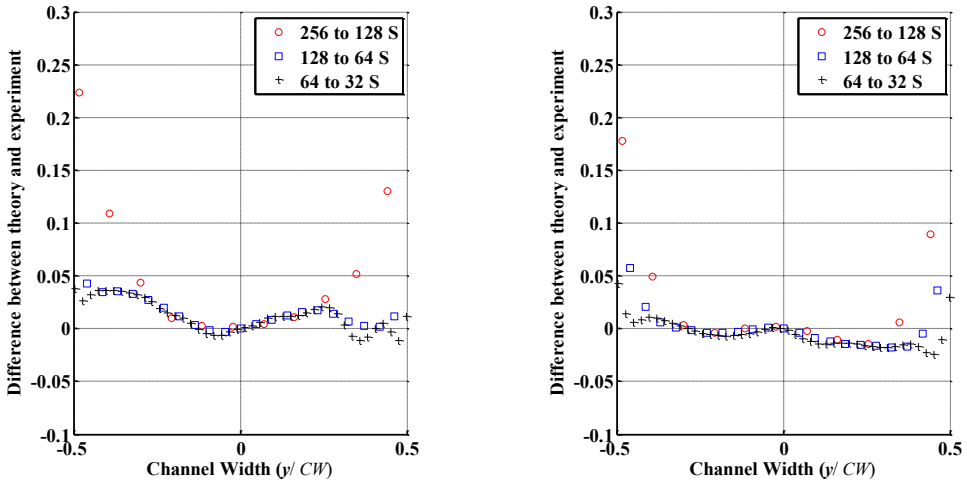

a) b)

Fig. 48: a) Difference between theoretical velocity profile and average experimental velocity profile calculated from instantaneous velocities for three different pass of decreasing square interrogation window size from 256 to 128, 128 to 64 and 64 and flow rate of 0.008 ml/min, b) 0.01 ml/min.

6.4 Error Analysis

There are different processes that effect on the PIV accuracy, such as PIV correlation standard procedures, peak evaluations, and software calculation, these are all parts of the whole process that may effect on the PIV accuracy and precision [25]. In this chapter three kind of error analysis are and measured. These three types consist of kurtosis, skewness and standard deviation, which are explained in details in the following paragraphs.

6.4.1 Skewness and Kurtosis of Experimental Results

The skewness and kurtosis analysis of the experiments data is calculated using Matlab software and results of kurtosis and skewness of analyzed data with different interrogation shapes are shown in Fig. 49, Fig. 50, and Fig. 51. All the plots of skewness and kurtosis have nearly the identical trends so their interpretations are equivalent. Skewness value shows lop-sidedness of the probability distribution of the valid experimental velocity values from the theoretical velocity values calculated from the analytical laminar velocity formula. Skewness value can be positive, negative and zero. The skewness value for the experiments results are around zero as depicted on the figures. The zero value of skewness can be representative of symmetric or asymmetric distributions of data. As it is observed in Fig. 37 as an example of figures for velocity profiles, the zero value of the skewness indicates that the distribution is approximately symmetric in the current study experiment's results.

Furthermore, it is observed from Fig. 49 the kurtosis has a positive number less than 3. So this conclusion can be drawn that the positive values of kurtosis for results talk about [50] the non-uniformity distribution of data and with generally platykurtic distribution, which have flatted top compared to normal distribution[45]. When the shape of the interrogation windows were changed the kurtosis value slightly changed but still have the value smaller than three as they are shown in Fig. 50 and Fig. 51, which the same conclusion of elliptic with aspect ratio of 4 is presented for these ones.

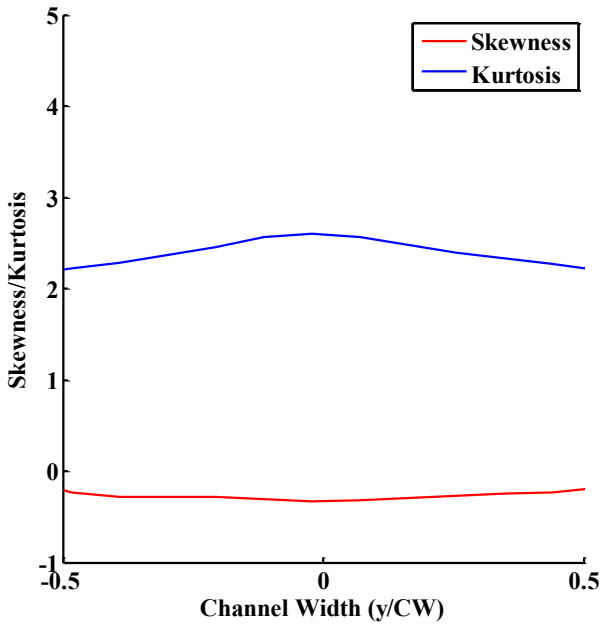

Fig. 49: Skewness and kurtosis of the experimental velocity for elliptic interrogation window with aspect ratio of 4.

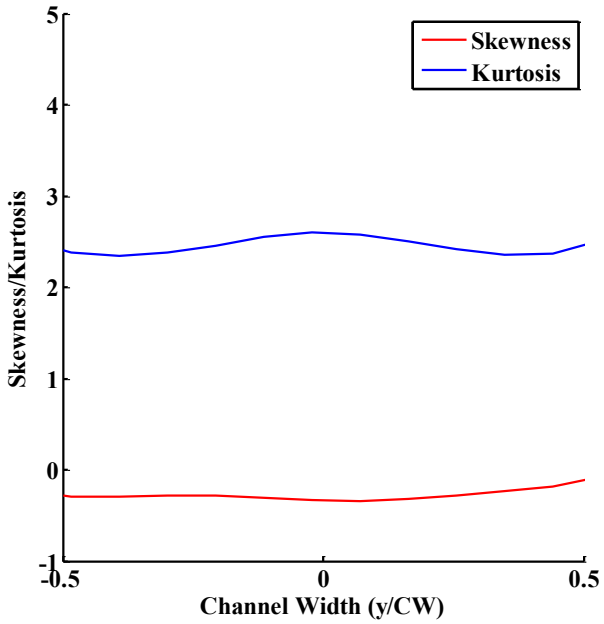

Fig. 50: Skewness and kurtosis of the experimental velocity for elliptic interrogation window with aspect ratio of 2.

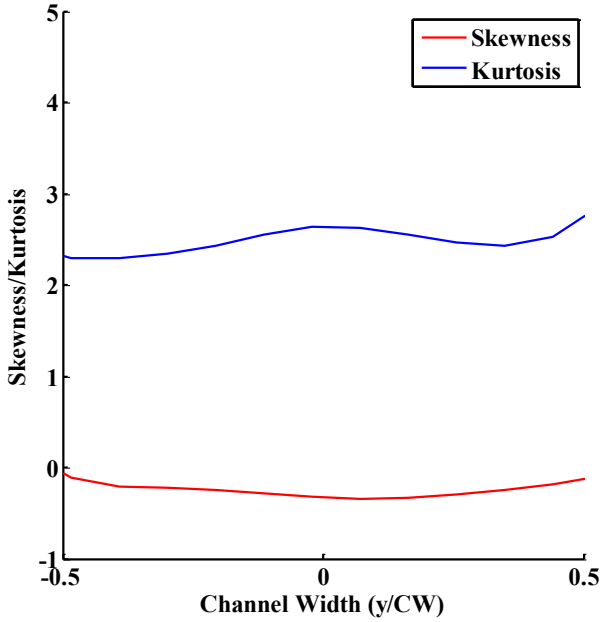

Fig. 51: Skewness and kurtosis of the experimental velocity for square interrogation window.

6.4.2 Standard Deviation

Brownian motion is much more significant in micro PIV application when the size of the seeding particles is small and velocity of the fluid is low. This Brownian motion in the micro PIV influence on the signal strength of the correlation function as it disturbs the correct measuring of the displacement for the particles and finding the accurate correlation peak from noise peaks [51]. One way of getting the good strength of correlation signal is omitting or reducing the magnitude of Brownian motion [52] which is possible by increasing the size of the seeding particle or making two successive laser pulses happen in short time interval [38]. The signal strength can be improved by reducing the magnitude of the Brownian motion by either increasing the particle diameter or decreasing the time intervals between two sequential laser pulses.

The standard deviation of the results obtained from three different interrogation windows are shown in Fig. 52 to Fig. 54. Standard deviation has a zero value in the middle of the channel location and its amount increases when it is calculated for the near wall regions. What observed from figures shows that values of velocity are very close to the expected value at the centre of the channel and deviate from real value within the boundary domain of the channel.

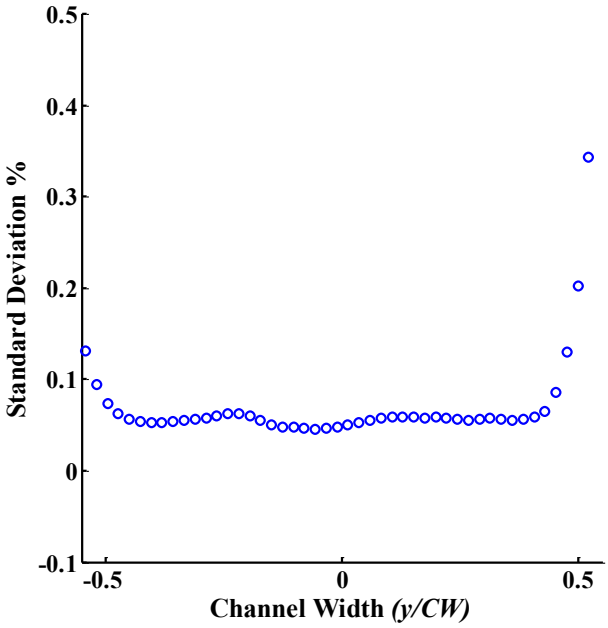

Fig. 52: Standard deviation of the experimental velocity for elliptic interrogation window with aspect ratio of 4 and interrogation windows of 64 decreasing to 32.

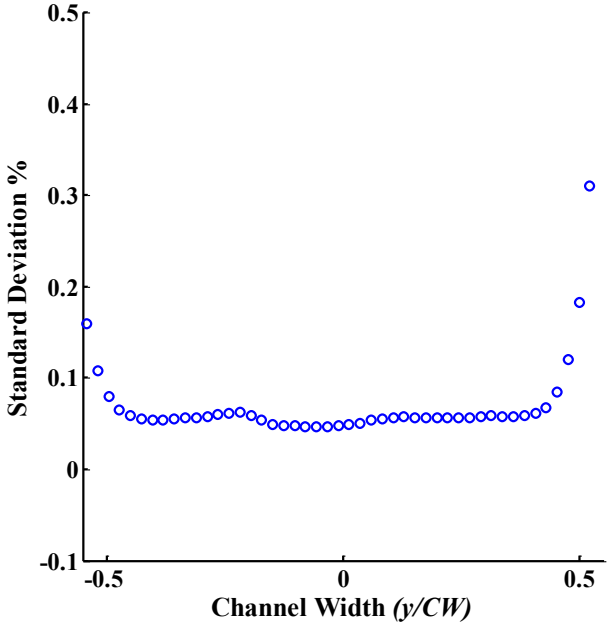

Fig. 53: Standard deviation of the experimental velocity for elliptic interrogation window with aspect ratio of 2 and interrogation windows of 64 decreasing to 32.

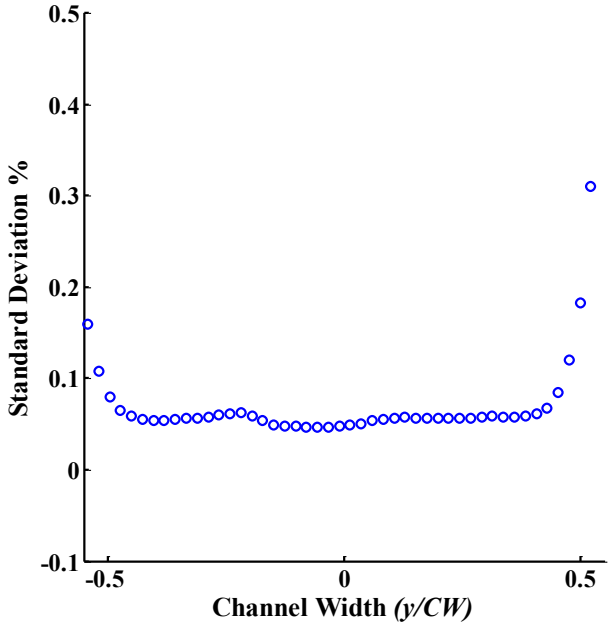

Fig. 54: Standard deviation of the experimental velocity for square interrogation and interrogation windows of 64 decreasing to 32.

6.5 Summary and Conclusions

Instantaneous velocity fields in microchannels measured using micro particle image velocimetry. Mean velocity profiles, differences between theory and experiment, and also skewness and kurtosis were determined from the micro PIV data. Flow studied in the straight microchannel was laminar.

Three interrogation window shapes and sizes studied, overall this conclusion can be drawn out that different shapes of the interrogation windows have not an effect on the velocity profile differences with theoretical profile, but different sizes of the interrogation windows have affected the near wall velocity measurements. The lowest interrogation window size of 64 × 64 to 32 × 32

showed a best correspondence of experimental velocity profile with theoretical velocity profile.

CHAPTER 7: **CONCLUSIONS AND FUTURE WORK**

This thesis used microscale particle image velocimetry (μPIV) to obtain the velocity measurements in straight microchannels. The fluid pumping into the microchannel is water filled with hollow sphere particles. The technique was validated by comparing the time-averaged velocity profiles with the theory. The velocity profile in the straight microchannel is assumed to be in parabolic shape as the theory proved this shape for the velocity profile in the confined channel.

7.1 Conclusion

Samples of 400 images of the laminar flow of fluid with particles in microchannel were taken with 90 frames per second frequency were analyzed in DaVis 8.0.7 to give the results demonstrated in previous chapters. Different methods which investigated for analyzing data are as first changing the interrogation window shapes and second changing the interrogation window sizes.

The result of this experimental investigation is that the velocity profile obeys being in the parabolic shape, but near wall velocity measurements show deterioration from the theory profile. Changes in the sizes of the interrogation windows have influence in the results. The smaller the sizes of interrogation windows are; the more compatible velocity profiles are with the theory. Experimental velocity profile obtained using elliptic interrogation window with

aspect ratio of 4 shows more compatibility with theoretical interrogation window near wall region.

There are a number of factors that influence on the errors come up near the wall. One source of error is the interference of the interrogation windows with the boundary layer, so lacking of enough particles in the interrogation windows will cause on not having a sharp correlation signal peak to measure velocity near the walls. Another source of error is Brownian motion and Saffman lift while Brownian motion is raised when the particles are very small. Authors like Wereley et al. [52] stated that the main source of error in micro PIV was migration of particles and the Saffman lift effect observed near the boundary and caused the less concentration of particles near the wall. It is observed in the experiment that the number of particles reduced in the interrogation windows associated to near wall regions. In addition, the out of focus particles in the images lower the quality of the image and produce background noise and influence on the correlation. The effect of background noise was decreased by pre processing of the raw image. Particles rolling on the wall boundary are also the source of producing error.

Overall, the experimental set up and the micro PIV technique was successfully developed to show the good corresponding to the velocity profile of theory in all parts of the profile except than near the wall. Along with experimental set up and micro PIV technique seed particles are also important to

be considered and what is used in these set of experiments showed a good faith in following the flow.

7.2 Future Work

Develop different methods like particle tracking velocimetry (PTV) to measure the velocity near the wall and try to decrease errors in near wall measurements. Another aspect of the future works can be on studying different shape of microchannel rather than straight microchannel which is used in this study. With different shapes of the channel different fluid types such as Newtonian and non-Newtonian can be studied and with the non-Newtonian fluid the rheology of the flow can be taken in to account.

References

[1] H. Andersson and A. van den Berg, "Microfluidic devices for cellomics: a review," *Sensors Actuators B Chem.*, vol. 92, no. 3, pp. 315–325, Jul. 2003.

[2] Y. Zhang and P. Ozdemir, "Microfluidic DNA amplification-A review.," *Anal. Chim. Acta*, vol. 638, no. 2, pp. 115–25, Apr. 2009.

[3] D. L. Chen and R. F. Ismagilov, "Microfluidic cartridges preloaded with nanoliter plugs of reagents: an alternative to 96-well plates for screening," *Curr. Opin. Chem. Biol.*, vol. 10, no. 3, pp. 226–231, 2006.

[4] K. P. Angele, Y. Suzuki, J. Miwa, N. Kasagi, and Y. Yamaguchi, "Development of a High-speed Scanning Micro-PIV system," *6th Int. Symp. Part. Image Velocim.*, pp. 1–6, 2005.

[5] C. Kuang, W. Zhao, F. Yang, and G. Wang, "Measuring flow velocity distribution in microchannels using molecular tracers," *Microfluid. Nanofluidics*, vol. 7, no. 4, pp. 509–517, 2009.

[6] U. Tallarek, E. Rapp, T. Scheenen, E. Bayer, and H. Van As, "Electroosmotic and Pressure-Driven Flow in Open and Packed Capillaries: Velocity Distributions and Fluid Dispersion," *Anal. Chem.*, vol. 72, no. 10, pp. 2292–2301, 2000.

[7] L. F. Gladden, “Magnetic Resonance: Ongoing and Future Role in Chemical Engineering Research,” *AIChE J.*, vol. 49, no. 1, pp. 2–9, 2000.

[8] C. Kuang, W. Zhao, F. Yang, and G. Wang, “Measuring flow velocity distribution in microchannels using molecular tracers,” *Microfluid. Nanofluidics*, vol. 7, no. 4, pp. 509–517, Jan. 2009.

[9] N. Aksel and M. Schmidtchen, “Analysis of the overall accuracy in LDV measurement of film flow in an inclined channel,” *Meas. Sci. Technol.*, vol. 1140, 1996.

[10] A. A. Adamczyk and L. Ritual, “2-Dimensional particle tracking,velocimetry (PTV): Technique and image processing algorithms,” *Exp. Fluids*, vol. 380, pp. 373–380, 1988.

[11] C. D. Meinhart, S. T. Wereley, and J. G. Santiago, “PIV measurements of a microchannel flow,” *Exp. Fluids*, vol. 27, no. 5, pp. 414–419, 1999.

[12] Y. Le Sant, F. Champagnat, and G. Le Besnerais, “Principles and Applications of Particle Image Velocimetry,” *Opt. Diagnostics Flows*, no. 1, 2009.

[13] N. Eom, V. Stevens, B. Wedding, R. Sedev, and J. Connor, “Probing fluid flow using the force measurement capability of optical trapping,” *Adv. Powder Technol.*, vol. 25, no. 4, pp. 1249–1253, 2014.

[14] J. G. Santiago, S. T. Wereley, C. D. Meinhart, D. J. Beebe, and R. J. Adrian, “A particle image velocimetry system for microfluidics,” *Exp. Fluids*, vol. 25, no. 4, pp. 316–319, 1998.

[15] S. T. Wereley and C. D. Meinhart, “Recent Advances in Micro-Particle Image Velocimetry,” *Annu. Rev. Fluid Mech.*, vol. 42, pp. 557–576, 2010.

[16] R. Lindken, M. Rossi, S. Grosse, and J. Westerweel, “Micro-Particle Image Velocimetry (microPIV): recent developments, applications, and guidelines.,” *Lab Chip*, vol. 9, no. 17, pp. 2551–67, 2009.

[17] P. Huang, J. S. Guasto, and K. S. Breuer, “Direct measurement of slip velocities using three-dimensional total internal reflection velocimetry,” *J. Fluid Mech.*, vol. 566, p. 447, 2006.

[18] C. M. Zettner and M. Yoda, “Particle velocity field measurements in a near-wall flow using evanescent wave illumination,” *Exp. Fluids*, vol. 34, pp. 115–121, 2003.

[19] R. J. Adrian and J. Westerweel, *Particle image velocimetry*. Cambridge university, 2011, p. 558.

[20] J. Wu, R. Kodzius, W. Cao, and W. Wen, “Extraction, amplification and detection of DNA in microfluidic chip-based assays,” *Microchim. Acta*, vol. 181, no. 13–14, pp. 1611–1631, 2013.

[21] F. Abhari, H. Jaafar, and N. A. Md Yunus, “A comprehensive study of micropumps technologies,” *Int. J. Electrochem. Sci.*, vol. 7, pp. 9765–9780, 2012.

[22] H. a. Mohammed, G. Bhaskaran, N. H. Shuaib, and R. Saidur, “Heat transfer and fluid flow characteristics in microchannels heat exchanger using nanofluids: A review,” *Renew. Sustain. Energy Rev.*, vol. 15, no. 3, pp. 1502–1512, 2011.

[23] K. D. Jensen, “Flow Measurements Techniques,” *J. Brazilian Soc. Mech. Sci. Eng.*, vol. XXVI, no. 4, pp. 2–3, 2004.

[24] Y. Yeh and H. Z. Cummins, “Localized fluid flow measurements with an HeNe laser spectrometer,” *Appl. Phys. Lett.*, vol. 4, no. 1964, pp. 176–178, 1964.

[25] M. Raffel, C. E. Willert, S. T. Wereley, and J. Kompenhans, *Particle Image Velocimetry: A Practical Guide*. Springer, 2007, p. 468.

[26] R. Adrian, “Particle-Imaging Techniques For Experimental Fluid-Mechanics,” *Annu. Rev. Fluid Mech.*, vol. 23, no. 1, pp. 261–304, 1991.

[27] C. D. Meinhart, S. T. Wereley, and M. H. B. Gray, “Volume illumination for two-dimensional particle image velocimetry,” *Meas. Sci. Technol.*, vol. 11, pp. 809–814, 2000.

[28] H. Search, C. Journals, A. Contact, M. Iopscience, and I. P. Address, "Volume illumination for two-dimensional particle image velocimetry," vol. 809, 2000.

[29] M. M. Mielnik, "Micro – PIV and its application to some BioMEMS related microfluidic flows," Norwegian University of Science and Technology, 2005.

[30] F. M.White, *Fluid Mechanics*, 2nd ed. New York: Mc Graw Hill, 1986.

[31] F. M.White, *Viscous Fluid Flow*. New York: Mc Graw Hill, 1974, p. 123.

[32] X. Zheng and Z. Silber-Li, "Measurement of velocity profiles in a rectangular microchannel with aspect ratio $\alpha = 0.35$," *Exp. Fluids*, vol. 44, no. 6, pp. 951–959, 2008.

[33] a Melling, "Tracer particles and seeding for particle image velocimetry," *Meas. Sci. Technol.*, vol. 8, pp. 1406–1416, 1999.

[34] R. J. M. Bastiaans, "Cross-correlation PIV; theory, implementation and accuracy," Eindhoven University of Technology, Eindhoven, 2000.

[35] M. Bahri, A. Lawi, N. Aris, M. S. Af, and M. Nur, "Relationships between Convolution and Correlation for Fourier Transform and Quaternion Fourier Transform," *Int. J. Math. Anal.*, vol. 7, no. 43, pp. 2101–2109, 2013.

[36] J. Lu, J. P. Fugal, H. Nordsiek, E. W. Saw, R. a. Shaw, and W. Yang, "Lagrangian particle tracking in three dimensions via single-camera in-line digital holography," *New J. Phys.*, vol. 10, 2008.

[37] G. E. Elsinga, B. Wieneke, F. Scarano, and B. W. van Oudheusden, "Assessment of Tomo-PIV for three-dimensional flows," *6th Int. Symp. Part. Image Velocim.*, pp. 1–10, 2005.

[38] M. Olsen, "Brownian motion and correlation in particle image velocimetry," *Opt. Laser Technol.*, vol. 32, no. 2000, pp. 621–627, 2000.

[39] K. S. Breuer, *Microscale Diagnostic Techniques*. Berlin Heidelberg: Springer New York, 2005, p. 272.

[40] A. Einstein, "On the movement of small particles suspended in stationary liquids required by the molecular kinetic theory of heat," *Ann. Phys.*, pp. 549–560, 1905.

[41] J. Westerweel, "Fundamentals of digital particle image velocimetry," *Meas. Sci. Technol.*, vol. 8, pp. 1379–1392, 1999.

[42] B. M. Wilson and B. L. Smith, "Uncertainty on PIV mean and fluctuating velocity due to bias and random errors," *Meas. Sci. Technol.*, vol. 24, pp. 1–15, 2013.

[43] C. K. Alexander and M. N. O. Sadiku, *Fundamentals of Electric Circuits*. 2011, pp. 1–12.

[44] N. L. Johnson, S. Kotz, and N. Balakrishnan, *Continuous univariate distributions*, 2nd ed. Wiley, 1994, p. 784.

[45] K. P. Balanda and H. L. Macgillivray, "Kurtosis: A Critical Review," *Am. Stat.*, vol. 42, no. 2, pp. 111–119, May 1988.

[46] D. S. Nobes, O. Chatterjee, and A. Setayeshgar, "Plenoptic Imaging for 3DμPTV Investigations of Micro-Scale Flows," *17 th Int. Symp. Appl. laser Tech. to fluid Mech.*, vol. 12, 2014.

[47] C. Willert, B. Stasicki, J. Klinner, and S. Moessner, "Pulsed operation of high-power light emitting diodes for imaging flow velocimetry," *Meas. Sci. Technol.*, vol. 21, p. 075402, 2010.

[48] R. Attota and R. Silver, "Optical microscope angular illumination analysis," *Opt. Express*, vol. 20, no. 6, p. 6693.

[49] D. B. Murphy, *Fundamentals of light microscopy and Electronic*. Wiley-Liss, 2001.

[50] K. P. Balanda and H. L. Macgillivray, "Kurtosis: A Critical Review," *Am. Stat.*, vol. 42, no. 2, pp. 111–119, 1988.

[51] M. G. Olsen and R. J. Adrian, "Out-of-focus effects on particle image visibility and correlation in microscopic particle image velocimetry," *Exp. Fluids*, vol. 29, 2000.

[52] S. Wereley, L. Gui, C. Meinhart, and D. Tretheway, “Single Pixel Evaluation of Microchannel Flows,” *ASME Int. Mech. Eng. Congr. Expo.*, pp. 1–6, 2005.

Appendix

Appendix A: Plotting Codes

In this part, the codes written in Matlab for analysis of the processed data in DaVis are available. At the beginning of each code there is a brief description associated with that code.

Code1.

Instantaneous velocity of each individual image is calculated individually and averaged to give a velocity profile. Skewness, kurtosis and standard deviation is also calculated in this code and plotted up. This code is for the data processed with elliptic interrogation window with aspect ratio 2, but the same code is used for the data processed with other interrogation windows.

```
clc % Clear command line
close all % Close figures
clear % Clear variables
%************ Instantaneous velocity profile for elliptic with
aspect ration of 2*************
 figure(1);
figure(2);
figure(3);
figure(4);
figure(5);
fX = 75; fY = 200;

set(1,'Pos',[fX+150 fY 1350 600]);
set(2,'Pos',[fX+150, fY 600 600]);
set(3,'Pos',[fX+150, fY 600 600]);
set(4,'Pos',[fX, fY 600 600]);
set(5,'Pos',[fX, fY 600 600]);
.............................................................
.......SCALE
DATA.........................................................
C_W = 831; % Width of channel in um

delta_t=1/90; % sec/frame - horizontal flow
```

```
calib=1.2; % um/pixel - horizontal flow

Xoff = 0;  % horizontal flow
Yoff = 495;  % horizontal flow


F = loadvec('*.vc7'); % Load .vc7 file in the current directory
AF=averf(F);  %returns the average of the vector/scalar fields F.
AF is a field of the same type as F, whose elements are the
average of the elements of the fields F.
figure(1)
set(gca, 'Position', [0.05 0.02 0.9 1])
showf(AF,'scalearrow',5, 'spacing', [8 3]);  % average of the
vector/ scalar fileds F



%Velocity_Centreline
%8888888888888888888888888888888
 figure(2)

 AF.x  = (AF.x - Xoff)*calib;     % converts pixels to microns
 AF.y  = (AF.y - Yoff)*calib;     % converts pixels to microns
 AF.vx = -(AF.vx*calib/delta_t);
 AFAVG = spaverf(AF,'X');
 MAX = max(AFAVG.vx(1,:));
Lam = MAX*(1-(AF.y/(C_W/2)).^2); % Theory Profile
Lam_scaled = Lam/MAX;
AFAVG.vx_scaled = AFAVG.vx/MAX;

hold on

plot(AF.y/C_W,AF.vx(30,:)/MAX,'ob');
plot(AF.y/C_W,Lam/MAX,'k','LineWidth',2);
hold off
legend('Experiment','Theory')
set(gca,'FontSize',16, 'FontName','Times New Roman',
'FontWeight','bold','Color','w','LineWidth',2);
xlabel('Channel Width
\it(y/\itCW)','Fontweight','bold','FontName','Times New
Roman','FontSize',16);
ylabel('{Axial Velocity
\bf(\mum/s)}','Fontweight','bold','FontName','Times New
Roman','FontSize',16);
axis([-0.5,0.5,0,1.1]);
grid


%8888888888888888888888888888888
figure(3)
hold on
plot(AF.y/C_W,AFAVG.vx_scaled(1,:),'b','LineWidth',2);
plot(AF.y/C_W,Lam_scaled,'k','LineWidth',2);
```

```
set(gca,'FontSize',16, 'FontName','Times New Roman',
'FontWeight','bold','Color','w','LineWidth',2);
xlabel('Channel Width
\it(y/\itCW)','Fontweight','bold','FontName','Times New
Roman','FontSize',16);
ylabel('{Axial Velocity
(\mum/s)}','Fontweight','bold','FontName','Times New
Roman','FontSize',16);
axis([-0.5,0.5,0,1.1]);
grid

%8888888888888888888888888888888888

 for j=1:length(AF.y)
  for i=1:100
      vex(i,j)=-F(1,i).vx(1,j);   %% Normalized velocity
      i=i+1;

  end

  skew(j) = skewness(vex(:,j));
  Kurt(j) = kurtosis(vex(:,j));
  j=j+1;
  end
 figure(4)
 hold on
 plot(AF.y/C_W, skew,'r','LineWidth',2)
 plot(AF.y/C_W, Kurt,'b','LineWidth',2)
 legend('Skewness','Kurtosis')
 set(gca,'FontSize',16, 'FontName','Times New Roman',
'FontWeight','bold','Color','w','LineWidth',2);
xlabel('Channel Width
\it(y/\itCW)','Fontweight','bold','FontName','Times New
Roman','FontSize',16);
ylabel('Skewness/Kurtosis','Fontweight','bold','FontName','Times
New Roman','FontSize',16);
  axis([-0.5,0.5, -1,8]);
  %........ Standard deviation of mean.............


  stdex = std(vex);
  stdex1 = stdex./mean(vex).*100;  % standard deviation in percent
  sem=stdex/sqrt(length(AF.vx)); % standard error of the mean
  sem1 = sem./mean(vex).*100;
 figure(5)
 hold on
 plot(AF.y/C_W, stdex1,'ob','LineWidth',2)
 set(gca,'FontSize',16, 'FontName','Times New Roman',
'FontWeight','bold','Color','w','LineWidth',2);
 xlabel('Channel Width
\it(y/\itCW)','Fontweight','bold','FontName','Times New
Roman','FontSize',16);
ylabel('standard deviation
%','Fontweight','bold','FontName','Times New
Roman','FontSize',16);
```

```
axis([-0.5,0.5, -0.1, 25]);
```

Code 2:

The changes in the velocity profile in different images because of slip stick phenomena are plotted using this code.

```
clc % Clear command line
close all % Close figures
clear % Clear variables
%********* Velocity Jerk motion*******
 figure(1);
figure(2);
figure(3);
figure(4);

fX = 75; fY = 200;

set(1,'Pos',[fX+150 fY 1350 600]);
set(2,'Pos',[fX+150, fY 1350 600]);
set(3,'Pos',[fX+150, fY 1350 600]);
set(4,'Pos',[fX, fY 600 600]);
% set(5,'Pos',[fX, fY 600 600]);
%
.....
.......SCALE
DATA.....
C_W = 831; % Width of channel in um

delta_t=1/90; % sec/frame - horizontal flow
calib=1.2; % um/pixel - horizontal flow

Xoff = 0;  % horizontal flow
Yoff = 495;  % horizontal flow


F = loadvec('B00151.vc7'); % Load .vc7 file in the current
directory
F1 = loadvec('B00175.vc7'); % Load .vc7 file in the current
directory
F2 = loadvec('B00200.vc7'); % Load .vc7 file in the current
directory
figure(1)
set(gca, 'Position', [0.05 0.02 0.9 1])
showf(F,'scalearrow',5, 'spacing', [8 3]);  % average of the
vector/ scalar fileds F
title('')
xlabel('\itX \rm\bf(Pixel)','Fontweight','bold','FontName','Times
New Roman','FontSize',18);
```

```
ylabel('\itY \rm\bf(Pixel)','Fontweight','bold','FontName','Times
New Roman','FontSize',18);
%***********
figure(2)
set(gca, 'Position', [0.05 0.02 0.9 1])
showf(F1,'scalearrow',5, 'spacing', [8 3]);  % average of the
vector/ scalar fileds F
title('')
xlabel('\itX \rm\bf(Pixel)','Fontweight','bold','FontName','Times
New Roman','FontSize',18);
ylabel('\itY \rm\bf(Pixel)','Fontweight','bold','FontName','Times
New Roman','FontSize',18);
%**********
figure(3)
set(gca, 'Position', [0.05 0.02 0.9 1])
showf(F2,'scalearrow',5, 'spacing', [8 3]);  % average of the
vector/ scalar fileds F
title('')
xlabel('\itX \rm\bf(Pixel)','Fontweight','bold','FontName','Times
New Roman','FontSize',18);
ylabel('\itY \rm\bf(Pixel)','Fontweight','bold','FontName','Times
New Roman','FontSize',18);
c=colorbar('FontSize',12,'FontName','Times New Roman');
%Velocity_Centreline
%8888888888888888888888888888888888
 figure(4)
%  AF.x  = AF.x*calib - Xoff;     % converts pixels to microns
%  AF.y  = AF.y*calib - Yoff;     % converts pixels to microns
 F.x  = (F.x - Xoff)*calib;     % converts pixels to microns
 F.y  = (F.y - Yoff)*calib;     % converts pixels to microns
 F.vx = -(F.vx*calib/delta_t);
 FAVG = spaverf(F,'X');
 MAX = max(FAVG.vx(1,:));
Lam = MAX*(1-(F.y/(C_W/2)).^2); % Theory Profile
Lam_scaled = Lam/MAX;
FAVG.vx_scaled = FAVG.vx/MAX;

hold on

plot(F.y/C_W,F.vx(30,:),'ob');
%plot(AF.y/C_W,AFAVG.vx(1,:),'b','LineWidth',2);

%************
 F1.x  = (F1.x - Xoff)*calib;     % converts pixels to microns
 F1.y  = (F1.y - Yoff)*calib;     % converts pixels to microns
 F1.vx = -(F1.vx*calib/delta_t);
 FAVG1 = spaverf(F1,'X');
 MAX1 = max(FAVG1.vx(1,:));
FAVG.vx_scaled1 = FAVG1.vx/MAX;

hold on
plot(F1.y/C_W,F1.vx(30,:),'om');

%*******
F2.x  = (F2.x - Xoff)*calib;     % converts pixels to microns
```

```
 F2.y  = (F2.y - Yoff)*calib;      % converts pixels to microns
 F2.vx = -(F2.vx*calib/delta_t);
 FAVG2 = spaverf(F2,'X');
 MAX2 = max(FAVG2.vx(1,:));
FAVG.vx_scaled2 = FAVG2.vx/MAX;

hold on
plot(F2.y/C_W,F2.vx(30,:),'ok');

hold off
legend('Experiment 150', 'Experiment 175', 'Experiment 200')
set(gca,'FontSize',12, 'FontName','Times New Roman',
'FontWeight','bold','Color','w','LineWidth',2);
xlabel('Channel Width
\it(y/\itCW)','Fontweight','bold','FontName','Times New
Roman','FontSize',16);
ylabel('Axial Velocity
(\mum/s)','Fontweight','bold','FontName','Times New
Roman','FontSize',16);
axis([-0.5,0.5,0,4000]);
grid
```

Code3:

Particle size distribution obtained from HELOS (H1019) is plotted using code3 for before settlement and code 4 for after settlement.

```
clear all;
close all;
clc;
%************* Particle size distribution before
settleing*************
set(0, 'DefaultAxesFontName', 'Times New Roman');
set(0, 'DefaultUIControlFontName', 'Times New Roman');
set(0, 'defaultUitableFontName', 'Times New Roman');
set(0, 'defaultTextFontName', 'Times New Roman');
set(0, 'defaultUipanelFontName', 'Times New Roman');

set(0,'DefaultLineLineWidth',1.6)
% set default font size, line width and marker size
font_size=12;
line_width_size = 1.5;
marker_size = 10;
line_style = {'-',':','-.',':','-.'};
marker_style = {'*','o','<','s','d'};
%Reading the data file
%begin
%%%%%%%%%%%%%%%%%%%%  PSD-Helos %%%%%%%%%%%%%%%%%%
myFolder = 'R:\NobesResearch\RezaSabbagh\Backup-
experimentalData\DataAND_Processing\Initial_Codes\PSD_Solver_grade
_efficiency\old-versions\Oly-s-Particles\Matlabfiles\before';
```

```
if ~isdir(myFolder)
  errorMessage = sprintf('Error: The following folder does not
exist:\n%s', myFolder);
  uiwait(warndlg(errorMessage));
  return;
end
filePattern = fullfile(myFolder, '*.txt');
logFiles = dir(filePattern);

for k = 1:length(logFiles)

  baseFileName = logFiles(k).name;
  fullFileName = fullfile(myFolder, baseFileName);
  fileID = fopen(fullFileName);
  HELOS_info = textscan(fileID,' %s ' ,38,'HeaderLines',0);
  fprintf(1, 'Now reading %s\n', fullFileName);
  %cutsizes_info = textscan(fileID,'%s' ,14,'HeaderLines',1);
  column_headers = textscan(fileID,'2014-06-12
12:51:55.1200%s','HeaderLines',1);
  column_headers = textscan(fileID,' %s ' ,38,'HeaderLines',0);
  %column_headers = reshape(column_headers{1,1},4,10)';
  counter =1;
final_data_cell(:,1) = HELOS_info{1,1};
final_data_cell(:,2) = column_headers{1,1};
for counter = 2:33
particle_size(counter-1,1) = str2num(final_data_cell{counter,1});
particle_size(counter-1,2) = str2num(final_data_cell{counter,2});
end
d50 = str2num(final_data_cell{35,2});
d50_str = final_data_cell{35,2};
%particle_distribution(:,1) = final_data_cell(2:33,2);
%particle_size (:,2) = final_data_cell(2:33,2);
figure(k);
hold on;
% set(gca,'FontSize',16, 'FontName','Times New Roman',
'FontWeight','bold','Color','w','LineWidth',2);
set(gca, 'xscale', 'log','FontSize',16, 'FontName','Times New
Roman', 'FontWeight','bold','Color','w','LineWidth',2);
plot (particle_size (:,1),particle_size (:,2), 'k-o');
text(20,0.9, ['d50=', d50_str],'FontSize',16);
% text(30,0.9, d50_str);
% title('Particle size distribution before settling');
xlabel('Particle Size (\mum)','FontName','Times New
Roman','FontSize',16,'Fontweight','bold');
ylabel(sprintf('Density Distribution'),'FontName','Times New
Roman','FontSize',16,'Fontweight','bold');

print -dps before-settling.eps
print -djpeg before-settling.jpg
hold off
end
axis([0.5 150 0 1.1]);
```

Code 4:

```
clear all;
close all;
clc;
%************** Particle size distribution after settleing
*********************
set(0, 'DefaultAxesFontName', 'Times New Roman');
set(0, 'DefaultUIControlFontName', 'Times New Roman');
set(0, 'defaultUitableFontName', 'Times New Roman');
set(0, 'defaultTextFontName', 'Times New Roman');
set(0, 'defaultUipanelFontName', 'Times New Roman');

set(0,'DefaultLineLineWidth',1.6)
% set default font size, line width and marker size
font_size=12;
line_width_size = 1.5;
marker_size = 10;
line_style = {'-',':','-.',':','-.'};
marker_style = {'*','o','<','s','d'};
%Reading the data file
%begin
%%%%%%%%%%%%%%%%%%%%  PSD-Helos %%%%%%%%%%%%%%%%%%
myFolder = 'R:\NobesResearch\RezaSabbagh\Backup-
experimentalData\DataAND_Processing\Initial_Codes\PSD_Solver_grade
_efficiency\old-versions\Oly-s-Particles\Matlabfiles\after';
if ~isdir(myFolder)
  errorMessage = sprintf('Error: The following folder does not
exist:\n%s', myFolder);
  uiwait(warndlg(errorMessage));
  return;
end
filePattern = fullfile(myFolder, '*.txt');
logFiles = dir(filePattern);

 %for k = 1:length(logFiles)
 for k = 1:1
  baseFileName = logFiles(k).name;
  fullFileName = fullfile(myFolder, baseFileName);
  fileID = fopen(fullFileName);
  HELOS_info = textscan(fileID,' %s ' ,38,'HeaderLines',0);
  fprintf(1, 'Now reading %s\n', fullFileName);
  %cutsizes_info = textscan(fileID,'%s' ,14,'HeaderLines',1);
  column_headers = textscan(fileID,'after %s','HeaderLines',1);
  column_headers = textscan(fileID,' %s ' ,38,'HeaderLines',0);
  %column_headers = reshape(column_headers{1,1},4,10)';
  counter =1;
final_data_cell(:,1) = HELOS_info{1,1};
final_data_cell(:,2) = column_headers{1,1};
for counter = 2:33
particle_size(counter-1,1) = str2num(final_data_cell{counter,1});
particle_size(counter-1,2) = str2num(final_data_cell{counter,2});
end
d50 = str2num(final_data_cell{35,2});
d50_str = final_data_cell{35,2};
%particle_distribution(:,1) = final_data_cell(2:33,2);
```

```
%particle_size (:,2) = final_data_cell(2:33,2);
figure(k);
hold on;
set(gca, 'xscale', 'log','FontSize',16, 'FontName','Times New
Roman', 'FontWeight','bold','Color','w','LineWidth',2);
plot (particle_size (:,1),particle_size (:,2), 'ko-');
text(12,1.6, ['d50=', d50_str],'FontSize',16);
% text(30,1.8, d50_str);
% title('Particle size distribution after settling');
xlabel('Particle Size (\mum)','FontName','Times New
Roman','FontSize',16,'Fontweight','bold');
ylabel(sprintf('Density Distribution'),'FontName','Times New
Roman','FontSize',16,'Fontweight','bold');

print -dps AfterSettling.eps
print -djpeg AfterSettling.jpg
hold off
end
axis([0.5 50 0 2.1]);
```

Code 5:

Different interrogation window sizes are compared in this code.

```
clc % Clear command line
close all % Close figures
clear % Clear variables
%***********Compare different pass interrogation size*******

figure(1); figure(2);
figure(3); figure(4);
figure(5);figure(6);
fX = 55; fY = 200;
set(1,'Pos',[fX fY+200 600 600]);
set(2,'Pos',[fX+600+15, fY+200 600 600]);
set(3,'Pos',[fX+2*(520), fY+200 520 600]);
set(4,'Pos',[fX fY-200 600 600]);
set(5,'Pos',[fX+600+15, fY-200 600 600]);
set(6,'Pos',[fX+2*(520), fY-200 520 600]);
 %
.....................................................................
.......Scale
Data.........................................................
C_W = 831; % Width of channel in um

%
.....................................................................
.......Different Pass_Velocity Profile
E4...........................................................
Fpath = 'R:\NobesResearch\Fahimeh
Behboodi\Experiments\29_Jan_15\Instantaneous';
% Fpath = 'R:\NobesResearch\Fahimeh
Behboodi\Experiments\13_Jan_15\test\Instantaneous';
figure(1)
```

```
load([Fpath '\AF_256_128_E4']);
AFy=AF.y;
AFAVG = spaverf(AF,'X');
 MAX = max(AFAVG.vx(20,:));
plot(AFy/C_W,AFAVG.vx(20,:)/MAX,'b','LineWidth',2);

load([Fpath '\AF_128_64_E4']);
AF1y=AF.y;
AFAVG1 = spaverf(AF,'X');
MAX = max(AFAVG1.vx(20,:));
hold on
plot(AF1y/C_W,AFAVG1.vx(20,:)/MAX,'r','LineWidth',2);

load([Fpath '\AF_64_32_E4']);
AF2y=AF.y;
AFAVG2 = spaverf(AF,'X');
MAX = max(AFAVG2.vx(20,:));
plot(AF2y/C_W,AFAVG2.vx(20,:)/MAX,'g','LineWidth',2);
MAX = max(AFAVG.vx(20,:));
Lam = MAX*(1-(AFy/(C_W/2)).^2); % Theory Profile
plot(AFy/C_W,Lam/MAX,'k','LineWidth',2);
hold off
legend('256 to 128 E4','128 to 64 E4','64 to 32 E4','Theory')
set(gca,'FontSize',16, 'FontName','Times New Roman',
'FontWeight','bold','Color','w','LineWidth',2);
xlabel('{Channel Width (y\rm/CW\rm)}','FontName','Times New
Roman','Fontsize',16,'Fontweight','bold');
ylabel('{Axial Velocity \rm (\mum/s)}','FontName','Times New
Roman','FontSize',16,'Fontweight','bold');
axis([-0.5,0.5,0,1.1]);
grid
                        %.....................Difference between
theory and experiment.............................
figure(4)
MAX1 = max(AFAVG1.vx(1,:));
MAX2 = max(AFAVG2.vx(1,:));

Lam1 = MAX1*(1-(AF1y/(C_W/2)).^2); % Theory Profile
Lam2 = MAX2*(1-(AF2y/(C_W/2)).^2); % Theory Profile
i=1;
for i=1:40

diff_exp_theo=AFAVG.vx(10,:)/MAX-Lam/MAX;
diff_exp_theo1=AFAVG1.vx(10,:)/MAX1-Lam1/MAX1;
diff_exp_theo2=AFAVG2.vx(10,:)/MAX2-Lam2/MAX2;

 i=i+1;
end
    y2 = -0.5:0.05:0.5;
    fit_Y = [];
    fit_Udiff = [];
    fit_Y1 = [];
    fit_Udiff1 = [];
    fit_Y2 = [];
```

```
    fit_Udiff2 = [];

    fit_Y = [fit_Y AFy/C_W];
    fit_Udiff = [fit_Udiff diff_exp_theo];

    fit_Y1 = [fit_Y1 AF1y/C_W];
    fit_Udiff1 = [fit_Udiff1 diff_exp_theo1];

    fit_Y2 = [fit_Y2 AF2y/C_W];
    fit_Udiff2 = [fit_Udiff2 diff_exp_theo2];

    p2 = polyfit(fit_Y,fit_Udiff,5);
    p2_1 = polyfit(fit_Y1,fit_Udiff1,5);
    p2_2 = polyfit(fit_Y2,fit_Udiff2,5);

    Udiff = polyval(p2,y2);
    Udiff1 = polyval(p2_1,y2);
    Udiff2 = polyval(p2_2,y2);
 hold on
 plot(AFy/C_W,diff_exp_theo, 'or')
 plot(AF1y/C_W,diff_exp_theo1, 'sb')
 plot(AF2y/C_W,diff_exp_theo2, '+g')
 plot(y2,Udiff,'r','LineWidth',2); % PLot the fit to the data
 plot(y2,Udiff1,'b','LineWidth',2); % PLot the fit to the data
 plot(y2,Udiff2,'g','LineWidth',2); % PLot the fit to the data
 legend('256 to 128 E4','128 to 64 E4','64 to 32 E4')
 set(gca,'FontSize',16, 'FontName','Times New Roman',
'FontWeight','bold','Color','w','LineWidth',2);
 xlabel('{Channel Width (y\rm/CW\rm)}','FontName','Times New
Roman','Fontsize',16,'Fontweight','bold');
 ylabel('{Difference between theory and
experiment}','FontName','Times New
Roman','Fontsize',16,'Fontweight','bold');

 axis([-0.5,0.5,-0.1,0.3]);
 grid


%
.....................................................................
.......Different Pass_Velocity Profile
E2.....................................................

figure(2)
load([Fpath '\AF_256_128_E2']);
AFy=AF.y;
AFAVG = spaverf(AF,'X');
MAX = max(AFAVG.vx(20,:));

plot(AFy/C_W,AFAVG.vx(20,:)/MAX,'b','LineWidth',2);

load([Fpath '\AF_128_64_E2']);
AF1y=AF.y;
AFAVG1 = spaverf(AF,'X');
```

```
MAX = max(AFAVG1.vx(20,:));
hold on
plot(AF1y/C_W,AFAVG1.vx(20,:)/MAX,'r','LineWidth',2);

load([Fpath '\AF_64_32_E2']);
AF2y=AF.y;
AFAVG2 = spaverf(AF,'X');
MAX = max(AFAVG2.vx(20,:));
plot(AF2y/C_W,AFAVG2.vx(20,:)/MAX,'g','LineWidth',2);
MAX = max(AFAVG.vx(20,:));
Lam = MAX*(1-(AFy/(C_W/2)).^2); % Theory Profile
plot(AFy/C_W,Lam/MAX,'k','LineWidth',2);
hold off
legend('256 to 128 E2','128 to 64 E2','64 to 32 E2','Theory')
set(gca,'FontSize',16, 'FontName','Times New Roman',
'FontWeight','bold','Color','w','LineWidth',2);
xlabel('{Channel Width (y\rm/CW\rm)}','FontName','Times New
Roman','Fontsize',16,'Fontweight','bold');
ylabel('{Axial Velocity \rm (\mum/s)}','FontName','Times New
Roman','FontSize',16,'Fontweight','bold');
axis([-0.5,0.5,0,1.1]);
grid

%.....................Difference between theory and
experiment.................................
figure(5)
MAX1 = max(AFAVG1.vx(1,:));
MAX2 = max(AFAVG2.vx(1,:));

Lam1 = MAX1*(1-(AF1y/(C_W/2)).^2); % Theory Profile
Lam2 = MAX2*(1-(AF2y/(C_W/2)).^2); % Theory Profile
i=1;
for i=1:40

diff_exp_theo=AFAVG.vx(10,:)/MAX-Lam/MAX;
diff_exp_theo1=AFAVG1.vx(10,:)/MAX1-Lam1/MAX1;
diff_exp_theo2=AFAVG2.vx(10,:)/MAX2-Lam2/MAX2;

 i=i+1;
end
    y2 = -0.5:0.05:0.5;
    fit_Y = [];
    fit_Udiff = [];
    fit_Y1 = [];
    fit_Udiff1 = [];
    fit_Y2 = [];
    fit_Udiff2 = [];

    fit_Y = [fit_Y AFy/C_W];
    fit_Udiff = [fit_Udiff diff_exp_theo];

    fit_Y1 = [fit_Y1 AF1y/C_W];
    fit_Udiff1 = [fit_Udiff1 diff_exp_theo1];
```

```
    fit_Y2 = [fit_Y2 AF2y/C_W];
    fit_Udiff2 = [fit_Udiff2 diff_exp_theo2];

    p2 = polyfit(fit_Y,fit_Udiff,5);
    p2_1 = polyfit(fit_Y1,fit_Udiff1,5);
    p2_2 = polyfit(fit_Y2,fit_Udiff2,5);

    Udiff = polyval(p2,y2);
    Udiff1 = polyval(p2_1,y2);
    Udiff2 = polyval(p2_2,y2);
 hold on
 plot(AFy/C_W,diff_exp_theo, 'or')
 plot(AF1y/C_W,diff_exp_theo1, 'sb')
 plot(AF2y/C_W,diff_exp_theo2, '+g')
 plot(y2,Udiff,'r','LineWidth',2); % PLot the fit to the data
 plot(y2,Udiff1,'b','LineWidth',2); % PLot the fit to the data
 plot(y2,Udiff2,'g','LineWidth',2); % PLot the fit to the data
 legend('256 to 128 E2','128 to 64 E2','64 to 32 E2')
 set(gca,'FontSize',16, 'FontName','Times New Roman',
'FontWeight','bold','Color','w','LineWidth',2);
 xlabel('{Channel Width (y\rm/CW\rm)}','FontName','Times New
Roman','Fontsize',16,'Fontweight','bold');
 ylabel('{Difference between theory and
experiment}','FontName','Times New
Roman','Fontsize',16,'Fontweight','bold');

 axis([-0.5,0.5,-0.1,0.3]);
 grid

%
.....................................................................
.......Different Pass_Velocity Profile
S.....................................................

figure(3)
load([Fpath '\AF_256_128_S']);
AFy=AF.y;
AFAVG = spaverf(AF,'X');
MAX = max(AFAVG.vx(20,:));

plot(AFy/C_W,AFAVG.vx(20,:)/MAX,'b','LineWidth',2);
load([Fpath '\AF_128_64_S']);
AF1y=AF.y;
AFAVG1 = spaverf(AF,'X');
MAX = max(AFAVG1.vx(20,:));
hold on
plot(AF1y/C_W,AFAVG1.vx(20,:)/MAX,'r','LineWidth',2);
load([Fpath '\AF_64_32_S']);
AF2y=AF.y;
AFAVG2 = spaverf(AF,'X');
MAX = max(AFAVG2.vx(20,:));
plot(AF2y/C_W,AFAVG2.vx(20,:)/MAX,'g','LineWidth',2);
MAX = max(AFAVG.vx(20,:));
Lam = MAX*(1-(AFy/(C_W/2)).^2); % Theory Profile
plot(AFy/C_W,Lam/MAX,'k','LineWidth',2);
```

```
hold off
legend('256 to 128 S','128 to 64 S','64 to 32 S','Theory')
set(gca,'FontSize',16, 'FontName','Times New Roman',
'FontWeight','bold','Color','w','LineWidth',2);
xlabel('{Channel Width (y\rm/CW\rm)}','FontName','Times New
Roman','Fontsize',16,'Fontweight','bold');
ylabel('{Axial Velocity \rm (\mum/s)}','FontName','Times New
Roman','FontSize',16,'Fontweight','bold');
axis([-0.5,0.5,0,1.1]);
grid

%.....................Difference between theory and
experiment.................................
figure(6)
MAX1 = max(AFAVG1.vx(1,:));
MAX2 = max(AFAVG2.vx(1,:));

Lam1 = MAX1*(1-(AF1y/(C_W/2)).^2); % Theory Profile
Lam2 = MAX2*(1-(AF2y/(C_W/2)).^2); % Theory Profile
i=1;
for i=1:40

diff_exp_theo=AFAVG.vx(10,:)/MAX-Lam/MAX;
diff_exp_theo1=AFAVG1.vx(10,:)/MAX1-Lam1/MAX1;
diff_exp_theo2=AFAVG2.vx(10,:)/MAX2-Lam2/MAX2;

 i=i+1;
end
    y2 = -0.5:0.05:0.5;
    fit_Y = [];
    fit_Udiff = [];
    fit_Y1 = [];
    fit_Udiff1 = [];
    fit_Y2 = [];
    fit_Udiff2 = [];

    fit_Y = [fit_Y AFy/C_W];
    fit_Udiff = [fit_Udiff diff_exp_theo];

    fit_Y1 = [fit_Y1 AF1y/C_W];
    fit_Udiff1 = [fit_Udiff1 diff_exp_theo1];

    fit_Y2 = [fit_Y2 AF2y/C_W];
    fit_Udiff2 = [fit_Udiff2 diff_exp_theo2];

    p2 = polyfit(fit_Y,fit_Udiff,5);
    p2_1 = polyfit(fit_Y1,fit_Udiff1,5);
    p2_2 = polyfit(fit_Y2,fit_Udiff2,5);

    Udiff = polyval(p2,y2);
    Udiff1 = polyval(p2_1,y2);
    Udiff2 = polyval(p2_2,y2);
 hold on
 plot(AFy/C_W,diff_exp_theo, 'or')
```

```
 plot(AF1y/C_W,diff_exp_theo1, 'sb')
 plot(AF2y/C_W,diff_exp_theo2, '+g')
 plot(y2,Udiff,'r','LineWidth',2); % PLot the fit to the data
 plot(y2,Udiff1,'b','LineWidth',2); % PLot the fit to the data
 plot(y2,Udiff2,'g','LineWidth',2); % PLot the fit to the data
 legend('256 to 128 S','128 to 64 S','64 to 32 S')
 set(gca,'FontSize',16, 'FontName','Times New Roman',
'FontWeight','bold','Color','w','LineWidth',2);
 xlabel('{Channel Width (y\rm/CW\rm)}','FontName','Times New
Roman','Fontsize',16,'Fontweight','bold');
 ylabel('{Difference between theory and
experiment}','FontName','Times New
Roman','Fontsize',16,'Fontweight','bold');

 axis([-0.5,0.5,-0.1,0.3]);
 grid
```

Code6:

Different interrogation window shapes are compared in this code.

```
clc % Clear command line
close all % Close figures
clear % Clear variables
%***********Compare different  interrogation shapes*******
figure(1); figure(2);
figure(3); figure(4);
figure(5);figure(6);
fX = 55; fY = 200;
set(1,'Pos',[fX fY+200 600 600]);
set(2,'Pos',[fX+600+15, fY+200 600 600]);
set(3,'Pos',[fX+2*(520), fY+200 520 600]);
set(4,'Pos',[fX fY-200 600 600]);
set(5,'Pos',[fX+600+15, fY-200 600 600]);
set(6,'Pos',[fX+2*(520), fY-200 520 600]);

 %
.............................................................
.......Scale
Data.........................................................
C_W = 831; % Width of channel in um

%
.............................................................
.......256_128_Velocity Profile
E4,E2$S......................................................
.
Fpath = 'R:\NobesResearch\Fahimeh
Behboodi\Experiments\29_Jan_15\Instantaneous';
% Fpath = 'R:\NobesResearch\Fahimeh
Behboodi\Experiments\13_Jan_15\test\Instantaneous';
figure(1)
```

```
load([Fpath '\AF_256_128_E4']);
AFy=AF.y;
AFAVG = spaverf(AF,'X');
 MAX = max(AFAVG.vx(20,:));
plot(AFy/C_W,AFAVG.vx(20,:)/MAX,'b','LineWidth',2);

load([Fpath '\AF_256_128_E2']);
AF1y=AF.y;
AFAVG1 = spaverf(AF,'X');
 MAX = max(AFAVG1.vx(20,:));
hold on
plot(AF1y/C_W,AFAVG1.vx(20,:)/MAX,'r','LineWidth',2);

load([Fpath '\AF_256_128_S']);
AF2y=AF.y;
AFAVG2 = spaverf(AF,'X');
 MAX = max(AFAVG2.vx(20,:));
plot(AF2y/C_W,AFAVG2.vx(20,:)/MAX,'g','LineWidth',2);
MAX = max(AFAVG.vx(10,:));
Lam = MAX*(1-(AFy/(C_W/2)).^2); % Theory Profile
plot(AFy/C_W,Lam/MAX,'k','LineWidth',2);
hold off
legend('256 to 128 E4','256 to 128 E2','256 to 128 S','Theory')
 set(gca,'FontSize',16, 'FontName','Times New Roman',
'FontWeight','bold','Color','w','LineWidth',2);
xlabel('{Channel Width (y\rm/CW\rm)}','FontName','Times New
Roman','Fontsize',16,'Fontweight','bold');
ylabel('{Axial Velocity \rm (\mum/s)}','FontName','Times New
Roman','FontSize',16,'Fontweight','bold');
axis([-0.5,0.5,0,1.1]);
grid
            %.....................Difference between theory and
experiment.............................
figure(4)
MAX1 = max(AFAVG1.vx(1,:));
MAX2 = max(AFAVG2.vx(1,:));

Lam1 = MAX1*(1-(AF1y/(C_W/2)).^2); % Theory Profile
Lam2 = MAX2*(1-(AF2y/(C_W/2)).^2); % Theory Profile
i=1;
for i=1:40

diff_exp_theo=AFAVG.vx(10,:)/MAX-Lam/MAX;
diff_exp_theo1=AFAVG1.vx(10,:)/MAX1-Lam1/MAX1;
diff_exp_theo2=AFAVG2.vx(10,:)/MAX2-Lam2/MAX2;

 i=i+1;
end
    y2 = -0.5:0.05:0.5;
    fit_Y = [];
    fit_Udiff = [];
    fit_Y1 = [];
    fit_Udiff1 = [];
    fit_Y2 = [];
```

```
    fit_Udiff2 = [];

    fit_Y = [fit_Y AFy/C_W];
    fit_Udiff = [fit_Udiff diff_exp_theo];

    fit_Y1 = [fit_Y1 AF1y/C_W];
    fit_Udiff1 = [fit_Udiff1 diff_exp_theo1];

    fit_Y2 = [fit_Y2 AF2y/C_W];
    fit_Udiff2 = [fit_Udiff2 diff_exp_theo2];

    p2 = polyfit(fit_Y,fit_Udiff,5);
    p2_1 = polyfit(fit_Y1,fit_Udiff1,5);
    p2_2 = polyfit(fit_Y2,fit_Udiff2,5);

    Udiff = polyval(p2,y2);
    Udiff1 = polyval(p2_1,y2);
    Udiff2 = polyval(p2_2,y2);
 hold on
 plot(AFy/C_W,diff_exp_theo, 'or')
 plot(AF1y/C_W,diff_exp_theo1, 'sb')
 plot(AF2y/C_W,diff_exp_theo2, '+g')
 plot(y2,Udiff,'r','LineWidth',2); % PLot the fit to the data
 plot(y2,Udiff1,'b','LineWidth',2); % PLot the fit to the data
 plot(y2,Udiff2,'g','LineWidth',2); % PLot the fit to the data
 legend('256 to 128 E4','256 to 128 E2','256 to 128 S')
  set(gca,'FontSize',16, 'FontName','Times New Roman',
'FontWeight','bold','Color','w','LineWidth',2);
 xlabel('{Channel Width
(y\rm/CW\rm)}','Fontsize',16,'FontName','Times New
Roman','Fontweight','bold');
 ylabel('{Difference between theory and
experiment}','FontName','Times New
Roman','Fontsize',16,'Fontweight','bold');

 axis([-0.5,0.5,-0.1,0.3]);
 grid
%
.....................................................................
.......128_64_Velocity Profile
E4,E2$S.....................................................
.

figure(2)
load([Fpath '\AF_128_64_E4']);
AFy=AF.y;
AFAVG = spaverf(AF,'X');
 MAX = max(AFAVG.vx(20,:));

plot(AFy/C_W,AFAVG.vx(20,:)/MAX,'b','LineWidth',2);

load([Fpath '\AF_128_64_E2']);
AF1y=AF.y;
AFAVG1 = spaverf(AF,'X');
```

```
 MAX = max(AFAVG1.vx(20,:));
hold on
plot(AF1y/C_W,AFAVG1.vx(20,:)/MAX,'r','LineWidth',2);

load([Fpath '\AF_128_64_S']);
AF2y=AF.y;
AFAVG2 = spaverf(AF,'X');
 MAX = max(AFAVG2.vx(20,:));
plot(AF2y/C_W,AFAVG2.vx(20,:)/MAX,'g','LineWidth',2);
MAX = max(AFAVG.vx(10,:));
Lam = MAX*(1-(AFy/(C_W/2)).^2); % Theory Profile
plot(AFy/C_W,Lam/MAX,'k','LineWidth',2);
hold off
legend('128 to 64 E4','128 to 64 E2','128 to 64 S','Theory')
 set(gca,'FontSize',16, 'FontName','Times New Roman',
'FontWeight','bold','Color','w','LineWidth',2);
xlabel('{Channel Width (y\rm/CW\rm)}','FontName','Times New
Roman','Fontsize',16,'Fontweight','bold');
ylabel('{Axial Velocity \rm (\mum/s)}','FontName','Times New
Roman','FontSize',16,'Fontweight','bold');
axis([-0.5,0.5,0,1.1]);
grid

%.....................Difference between theory and
experiment.................................
figure(5)
MAX1 = max(AFAVG1.vx(1,:));
MAX2 = max(AFAVG2.vx(1,:));

Lam1 = MAX1*(1-(AF1y/(C_W/2)).^2); % Theory Profile
Lam2 = MAX2*(1-(AF2y/(C_W/2)).^2); % Theory Profile
i=1;
for i=1:40

diff_exp_theo=AFAVG.vx(10,:)/MAX-Lam/MAX;
diff_exp_theo1=AFAVG1.vx(10,:)/MAX1-Lam1/MAX1;
diff_exp_theo2=AFAVG2.vx(10,:)/MAX2-Lam2/MAX2;

 i=i+1;
end
    y2 = -0.5:0.05:0.5;
    fit_Y = [];
    fit_Udiff = [];
    fit_Y1 = [];
    fit_Udiff1 = [];
    fit_Y2 = [];
    fit_Udiff2 = [];

    fit_Y = [fit_Y AFy/C_W];
    fit_Udiff = [fit_Udiff diff_exp_theo];

    fit_Y1 = [fit_Y1 AF1y/C_W];
    fit_Udiff1 = [fit_Udiff1 diff_exp_theo1];
```

```
    fit_Y2 = [fit_Y2 AF2y/C_W];
    fit_Udiff2 = [fit_Udiff2 diff_exp_theo2];

    p2 = polyfit(fit_Y,fit_Udiff,5);
    p2_1 = polyfit(fit_Y1,fit_Udiff1,5);
    p2_2 = polyfit(fit_Y2,fit_Udiff2,5);

    Udiff = polyval(p2,y2);
    Udiff1 = polyval(p2_1,y2);
    Udiff2 = polyval(p2_2,y2);
 hold on
 plot(AFy/C_W,diff_exp_theo, 'or')
 plot(AF1y/C_W,diff_exp_theo1, 'sb')
 plot(AF2y/C_W,diff_exp_theo2, '+g')
 plot(y2,Udiff,'r','LineWidth',2); % PLot the fit to the data
 plot(y2,Udiff1,'b','LineWidth',2); % PLot the fit to the data
 plot(y2,Udiff2,'g','LineWidth',2); % PLot the fit to the data
 legend('128 to 64 E4','128 to 64 E2','128 to 64 S')
  set(gca,'FontSize',16, 'FontName','Times New Roman',
'FontWeight','bold','Color','w','LineWidth',2);
 xlabel('{Channel Width (y\rm/CW\rm)}','FontName','Times New
Roman','Fontsize',16,'Fontweight','bold');
 ylabel('{Difference between theory and
experiment}','FontName','Times New
Roman','Fontsize',16,'Fontweight','bold');

 axis([-0.5,0.5,-0.1,0.3]);
 grid


%
.....................................................................
.......64_32_Velocity Profile
E4,E2$S.....................................................
.

figure(3)
load([Fpath '\AF_64_32_E4']);
AFy=AF.y;
AFAVG = spaverf(AF,'X');
 MAX = max(AFAVG.vx(20,:));

plot(AFy/C_W,AFAVG.vx(20,:)/MAX,'b','LineWidth',2);
load([Fpath '\AF_64_32_E2']);
AF1y=AF.y;
AFAVG1 = spaverf(AF,'X');
 MAX = max(AFAVG1.vx(20,:));
hold on
plot(AF1y/C_W,AFAVG1.vx(20,:)/MAX,'r','LineWidth',2);
load([Fpath '\AF_64_32_S']);
AF2y=AF.y;
AFAVG2 = spaverf(AF,'X');
 MAX = max(AFAVG2.vx(20,:));
plot(AF2y/C_W,AFAVG2.vx(20,:)/MAX,'g','LineWidth',2);
MAX = max(AFAVG.vx(10,:));
```

```
Lam = MAX*(1-(AFy/(C_W/2)).^2); % Theory Profile
plot(AFy/C_W,Lam/MAX,'k','LineWidth',2);
hold off
legend('64 to 32 E4','64 to 32 E2','64 to 32 S','Theory')
 set(gca,'FontSize',16, 'FontName','Times New Roman',
'FontWeight','bold','Color','w','LineWidth',2);
xlabel('{Channel Width (y\rm/CW\rm)}','FontName','Times New
Roman','Fontsize',16,'Fontweight','bold');
ylabel('{Axial Velocity \rm (\mum/s)}','FontName','Times New
Roman','FontSize',16,'Fontweight','bold');
axis([-0.5,0.5,0,1.1]);
grid

%.....................Difference between theory and
experiment.................................
figure(6)
MAX1 = max(AFAVG1.vx(1,:));
MAX2 = max(AFAVG2.vx(1,:));

Lam1 = MAX1*(1-(AF1y/(C_W/2)).^2); % Theory Profile
Lam2 = MAX2*(1-(AF2y/(C_W/2)).^2); % Theory Profile
i=1;
for i=1:40

diff_exp_theo=AFAVG.vx(10,:)/MAX-Lam/MAX;
diff_exp_theo1=AFAVG1.vx(10,:)/MAX1-Lam1/MAX1;
diff_exp_theo2=AFAVG2.vx(10,:)/MAX2-Lam2/MAX2;

 i=i+1;
end
    y2 = -0.5:0.05:0.5;
    fit_Y = [];
    fit_Udiff = [];
    fit_Y1 = [];
    fit_Udiff1 = [];
    fit_Y2 = [];
    fit_Udiff2 = [];

    fit_Y = [fit_Y AFy/C_W];
    fit_Udiff = [fit_Udiff diff_exp_theo];

    fit_Y1 = [fit_Y1 AF1y/C_W];
    fit_Udiff1 = [fit_Udiff1 diff_exp_theo1];

    fit_Y2 = [fit_Y2 AF2y/C_W];
    fit_Udiff2 = [fit_Udiff2 diff_exp_theo2];

    p2 = polyfit(fit_Y,fit_Udiff,5);
    p2_1 = polyfit(fit_Y1,fit_Udiff1,5);
    p2_2 = polyfit(fit_Y2,fit_Udiff2,5);

    Udiff = polyval(p2,y2);
    Udiff1 = polyval(p2_1,y2);
    Udiff2 = polyval(p2_2,y2);
```

```
 hold on
 plot(AFy/C_W,diff_exp_theo, 'or')
 plot(AF1y/C_W,diff_exp_theo1, 'sb')
 plot(AF2y/C_W,diff_exp_theo2, '+g')
 plot(y2,Udiff,'r','LineWidth',2); % PLot the fit to the data
 plot(y2,Udiff1,'b','LineWidth',2); % PLot the fit to the data
 plot(y2,Udiff2,'g','LineWidth',2); % PLot the fit to the data
 legend('64 to 32 E4','64 to 32 E2','64 to 32 S')
  set(gca,'FontSize',16, 'FontName','Times New Roman',
'FontWeight','bold','Color','w','LineWidth',2);
 xlabel('{Channel Width (y\rm/CW\rm)}','FontName','Times New
Roman','Fontsize',16,'Fontweight','bold');
 ylabel('{Difference between theory and
experiment}','FontName','Times New
Roman','Fontsize',16,'Fontweight','bold');

 axis([-0.5,0.5,-0.1,0.3]);
 grid
```

Appendix B: PIV Analysis

The process of doing PIV on the images on DaVis 8.0.7 are shown as follows:

- Choosing parameter
- Subtract sliding minimum in preprocessing
- PIV time series, choosing multi pass with decreasing interrogation window sizes and choosing three different window shapes of square, elliptic with aspect ratio of 2 and elliptic with aspect ratio of 4

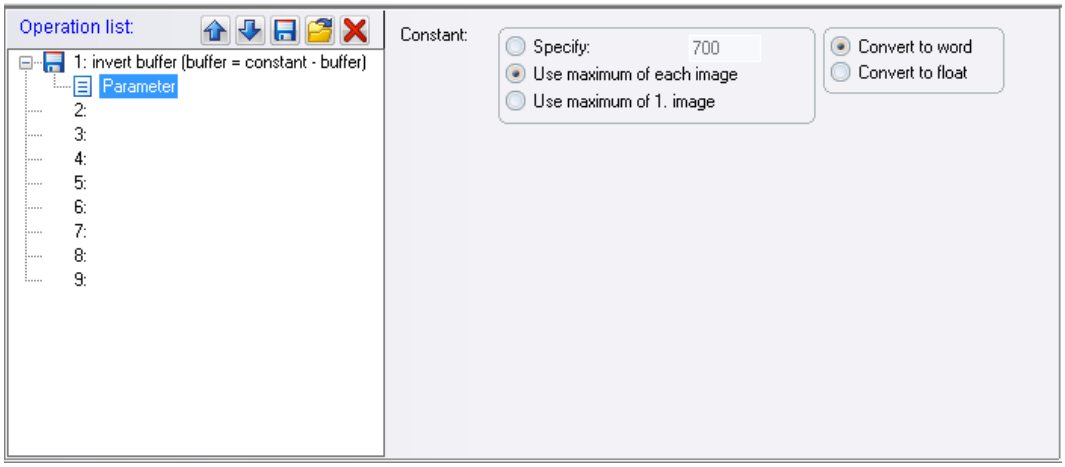

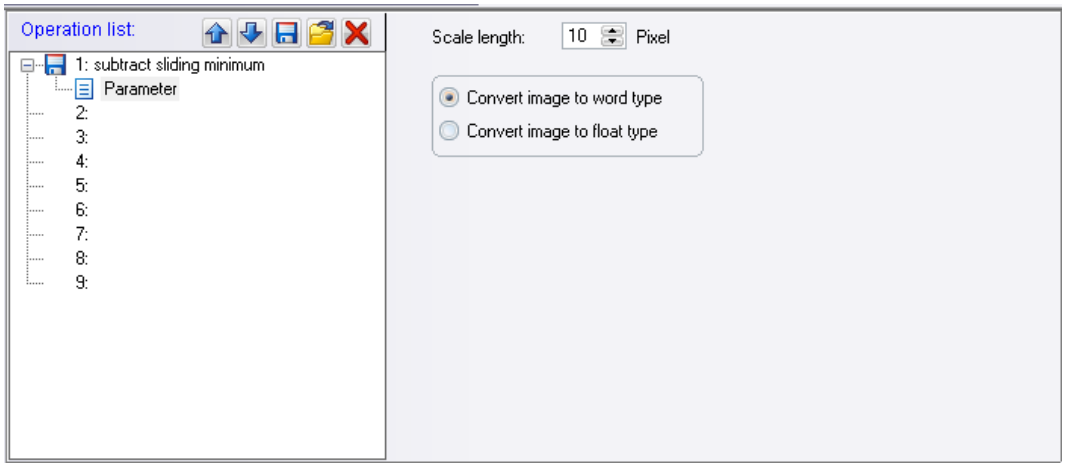

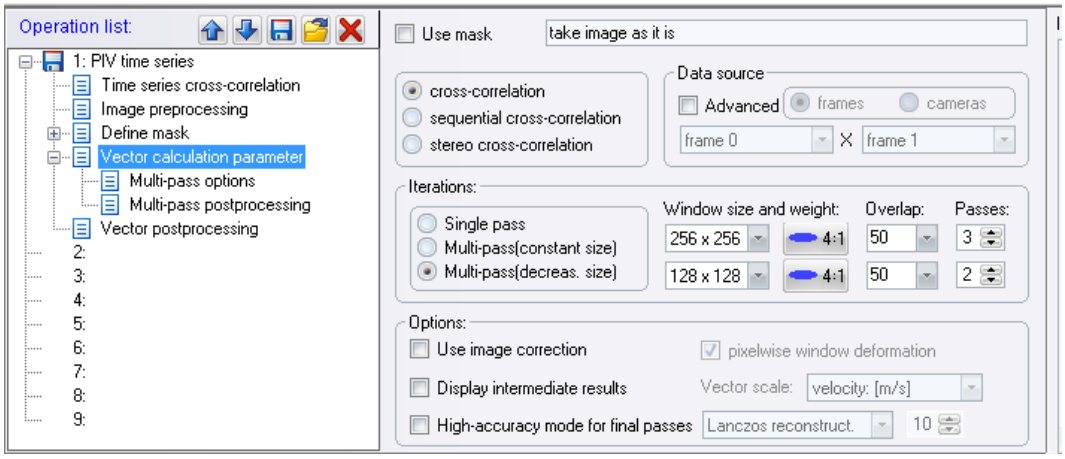
Operation list:
1: PIV time series
Time series cross-correlation
Image preprocessing
Define mask
Vector calculation parameter
Multi-pass options
Multi-pass postprocessing
Vector postprocessing
2:
3:
4:
5:
6:
7:
8:
9:
Use mask
take image as it is
cross-correlation
sequential cross-correlation
stereo cross-correlation
Data source
Advanced
frames
cameras
frame 0
X
frame 1
Iterations:
Single pass
Multi-pass(constant size)
Multi-pass(decreas. size)
Window size and weight:
Overlap:
Passes:
256 x 256
4:1
50
3
128 x 128
4:1
50
2
Options:
Use image correction
pixelwise window deformation
Display intermediate results
Vector scale:
velocity: [m/s]
High-accuracy mode for final passes
Lanczos reconstruct.
10

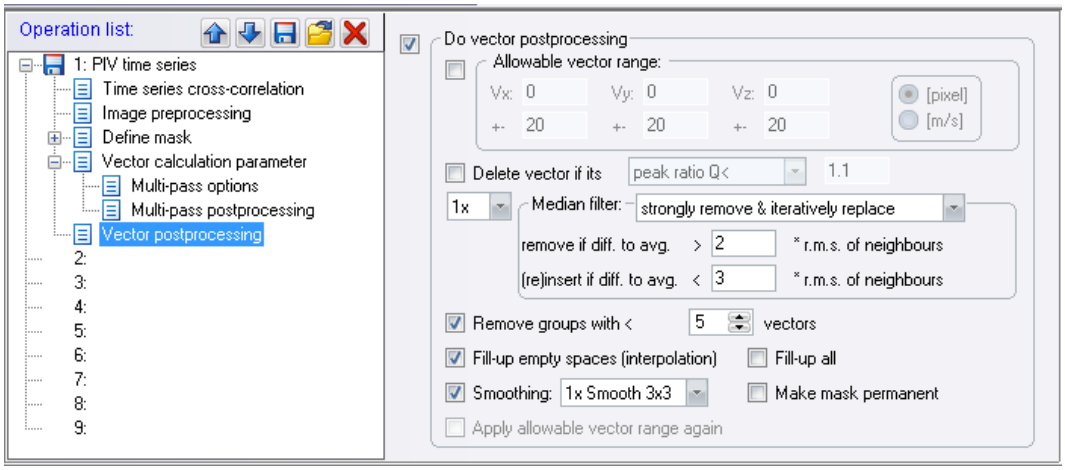
Operation list:
1: PIV time series
Time series cross-correlation
Image preprocessing
Define mask
Vector calculation parameter
Multi-pass options
Multi-pass postprocessing
Vector postprocessing
2:
3:
4:
5:
6:
7:
8:
9:
Do vector postprocessing
Allowable vector range:
Vx: 0
Vy: 0
Vz: 0
+- 20
+- 20
+- 20
[pixel]
[m/s]
Delete vector if its
peak ratio Q<
1.1
1x
Median filter:
strongly remove & iteratively replace
remove if diff. to avg. > 2 * r.m.s. of neighbours
(re)insert if diff. to avg. < 3 * r.m.s. of neighbours
Remove groups with < 5 vectors
Fill-up empty spaces (interpolation)
Fill-up all
Smoothing:
1x Smooth 3x3
Make mask permanent
Apply allowable vector range again